Title
Establishing Structure-Function Relationships for Soft Thermoelectric Materials Through Rational Design

Permalink
https://escholarship.org/uc/item/96m82786

Author
Gordon, Madeleine P.

Publication Date
2021

Peer reviewed|Thesis/dissertation

Establishing Structure-Function Relationships for Soft Thermoelectric Materials Through Rational Design

By

Madeleine P. Gordon

A dissertation submitted in partial satisfaction of the

requirements for the degree of

Doctor of Philosophy

in

Applied Science and Technology

in the

Graduate Division

of the

University of California, Berkeley

Committee In Charge
Dr. Jeffrey Urban, Co-Chair
Professor Junqiao Wu, Co-Chair
Professor Christopher Dames
Professor David Attwood

Summer 2021

Abstract

Establishing Structure-Function Relationships for Soft Thermoelectric Materials Through Rational Design

By

Madeleine P. Gordon

Doctor in Applied Science and Technology Graduate Group

University of California, Berkeley

Dr. Jeffrey Urban, Co-Chair
Professor Junqiao Wu, Co-Chair

Thermoelectric generators offer an exciting avenue for enhancing the efficiency of existing heat engines through the scavenging of waste heat. These direct heat to electricity converting devices even have the potential to power small electronic devices through body heat alone. Traditionally, thermoelectric materials are dominated by inorganic rare earth elements which, while achieving high degrees of performance, have limited the widespread deployment of thermoelectric generators due to prohibitive manufacturing costs, energy intensive processes and rigid device form factors. However, propelled by recent advances in soft electronic materials and the advent of personal electronic devices and the internet of things, there has been a surge of interest in developing carbon-based thermoelectric systems. Within this family of soft thermoelectrics, hybrid materials composed of organic and inorganic constituents have demonstrated interesting physical phenomenon and promising performance enhancements. While these materials are intriguing due to their potential for realizing novel transport physics, the non-linear interactions occurring at the organic-inorganic interface are not well understood. This makes the design of new cutting-edge hybrid materials more challenging.

In order to establish more concrete design rules to help guide the development of next generation hybrid thermoelectric materials, we chose to begin by focusing on a well-studied hybrid model system composed of tellurium (Te) nanowire cores and a conducting polymer poly(3,4-ethylenedioxythiophene) polystyrene sulfonate (PEDOT:PSS) shell. While this Te-PEDOT:PSS hybrid system has been extensively characterized, little has been done to systematically investigate the impacts of nanowire length and diameter as a knob for tuning thermoelectric performance. To pursue this, we utilized a synthetic procedure leveraging different molecular weights of polyvinyl pyrrolidone (PVP) to act as the structure directing and surface passivating ligand for the Te atoms during the nucleation process. Upon synthesizing the nanowires, a gentle ligand exchange process was used to transform the shell from insulating PVP to conductive PEDOT:PSS. We show that it is possible to tune Te nanowire dimensions by using different molecular weights of PVP and a 183% increase in thermoelectric performance can be achieved compared to prior literature reports of similarly sized Te-PEDOT:PSS nanowires. Interestingly, diameter appears to be the nanowire dimension most responsible for enhancing performance.

To better understand this apparent diameter dependence, we chose to further simplify the model system to a single Te-PEDOT:PSS nanowire in order to be able to more effectively isolate

transport phenomenon. We show that as the nanowire diameter is reduced, the electrical conductivity increases and the thermal conductivity decreases, while the Seebeck coefficient remains nearly constant. The origin of the decoupling of charge and heat transport lies in the fact that electrical transport occurs through the organic shell, while thermal transport is driven by the inorganic core.

With this first ever experimental validation of electrical transport occurring predominantly within the organic shell, one clear avenue for enhancing thermoelectric transport is through modulation and control over shell morphology. Knowing this, we investigated alternative approaches for controlling organic polymer structure through heteroatom substitution. Poly(3-(3’,7’-dimethyloctyl) chalcogenophenes) (P3RX) doped with 2,3,5,6-tetrafluoro-7,7,8,8-tetracyanoquinodimethane (F4TCNQ) was chosen to study and the doping methodology, the heteroatom (X = Thiophene (T), Selenophene (Se), Tellurophene (Te)) and the extent of doping are systematically varied. By spectroscopically, structurally and thermoelectrically characterizing these P3RX polymers we find that heteroatom identity radically impacts degree of structural ordering. Furthermore, we find that structural ordering not only impacts electronic charge transport but also the success of dopant:polymer interactions.

The findings detailed in this dissertation help to establish clear design rules upon which the next generation of cutting-edge hybrid materials can be based. In addition to the implications for enhancing thermoelectric transport in hybrid materials, the final study also aids in establishing a better understanding of how to leverage the most optimal organic polymer doping conditions, a topic highly relevant to the organic electronics community.

Table of Contents

ABSTRACT **1**
LIST OF FIGURES .... **II**
LIST OF TABLES .... **VIII**
ACKNOWLEDGEMENTS .... **IX**
CHAPTER 1. INTRODUCTION **1**
1.1 THERMOELECTRIC HISTORY 1
1.2 BASIC PRINCIPLES 2
1.3 CHALLENGES 5
1.4 EMERGING AREAS 7
1.5 OUTLINE AND SUMMARY OF CORE DISSERTATION CHAPTERS 10
CHAPTER 2. TRANSPORT FUNDAMENTALS **12**
2.1 INORGANIC CHARGE TRANSPORT 12
2.2 ORGANIC CHARGE TRANSPORT 14
2.3 HYBRID CHARGE TRANSPORT 17
2.4 THERMAL TRANSPORT 18
2.5 CONCLUSIONS 19
CHAPTER 3. MODULATION OF NANOWIRE DIAMETER AND THERMOELECTRIC PERFORMANCE VIA SYNTHETICALLY TUNING LIGAND MOLECULAR WEIGHT **21**
3.1 ABSTRACT 21
3.2 INTRODUCTION 21
3.3 RESULTS AND DISCUSSION 22
3.4 CONCLUSIONS 27
3.5 MATERIALS AND METHODS 27
3.6 ACKNOWLEDGEMENTS 30
3.7 SUPPORTING INFORMATION 30
CHAPTER 4. IDENTIFYING THE DECOUPLING OF CHARGE AND HEAT TRANSPORT BY ENACTING A HYBRID SINGLE NANOWIRE INVESTIGATION **35**
4.1 ABSTRACT 35
4.2 INTRODUCTION 35
4.3 RESULTS AND DISCUSSION 37
4.4 CONCLUSIONS 48
4.5 MATERIALS AND METHODS 49
4.6 ACKNOWLEDGMENTS 51
4.7 SUPPORTING INFORMATION 51
CHAPTER 5. CONTROL OVER MORPHOLOGY AND DOPING MECHANISM IN POLY(ALKYL-CHALCOGENEOPHENES) VIA HETEROATOM SUBSTITUTION **66**
5.1 ABSTRACT 66
5.2 INTRODUCTION 66
5.3 RESULTS AND DISCUSSION 68
5.4 CONCLUSIONS 76
5.5 MATERIALS AND METHODS 76
5.6 ACKNOWLEDGEMENTS 78
5.7 SUPPORTING INFORMATION 78
CHAPTER 6. CONCLUSIONS AND FUTURE OUTLOOKS **92**
CHAPTER 7. REFERENCES **94**

List of Figures

Figure 1.1- A TE module schematic a. showing the migration of charge carriers (- indicates electrons, + indicates holes) from the hot side to the cold side under (a.) power generation configuration and (b.) under a Peltier cooling configuration.

Figure 1.2- Visual representation of the relationship between the three major thermoelectric properties, Seebeck coefficient, thermal conductivity, and electrical conductivity as a function of carrier concentration. Panel a. shows the common tradeoffs between the properties for traditional materials, making overall device performance, *ZT*, quite challenging to enhance. Also shown plotted is Power Factor, $S^2\sigma$, which is often used as a general stand in for *ZT*. Panel b. shows the relative contributions to the total thermal conductivity, k, from the lattice thermal conductivity, $k_{lattice}$, and the electronic thermal conductivity, $k_{Electron}$, as a function of carrier concentration.

Figure 1.3- A general schematic depicting the landscape of organic and hybrid materials in terms of the sliding scale of Seebeck coefficient and electrical conductivity.

Figure 1.4- Overview of the TE properties of a wide sampling of performances reported for organic and hybrid materials.[23,37,59–68] The Seebeck coefficient (top) and power factor (bottom) are plotted as a function of electrical conductivity. Bi_2Te_3 compound performances are plotted as well in order to provide references to the benchmark industry standard material.

Figure 2.1- A graphical representation of the energy dependent electrical conductivity for a traditional material exhibiting band-like transport. Panel a. depicts the Fermi probability distribution function with the Fermi level (also referred to as the chemical potential) marked by the red dashed line. Panel b. demonstrates the resulting distribution from the partial derivative of the fermi distribution function with respect to energy, centered about the fermi level. In panel c., by multiplying the function shown in b. by the density of states *g(E)*, an offset distribution (shown in bright blue) appears which is representative of the carriers energetically available to participate in charge transport.

Figure 3.1- Depiction of the synthetic process employed, paired with SEM and HRTEM micrographs depicting the structure of the Te-PVP coated NWs. Panel (a) shows a general cartoon schematic of the multi-step synthetic process for forming the hybrid nanostructures. A representative scanning electron micrograph shows the microscale morphology of the Te-PVP NWs in panel (b). Panel (c) depicts a representative transmission electron micrograph of the Te-PVP wire which shows the thin polymer layer on the surface of the inorganic core and distinctly shows the lattice fringes indicative of atomic spacings in the unit cell.

Figure 3.2- Scanning electron micrographs and Powder X-ray Diffraction (PXRD) for Te NWs synthesized with 3 different molecular weights of PVP show a clear trend of increasing *AR* distribution as a function of PVP molecular weight increase. Panel (a) corresponds to PVP-29 wires, (b) PVP-40 NWs and (c) PVP-55 NWs. Panel (d) provides clear confirmation that all the Te NW batches are of the same trigonal crystal structure belonging to space group P3121. Above

panel (d) a visual representation of the Te NW facets can be found where the body facet (100) is marked in pink and the end facet (101) is highlighted in blue.

Figure 3.3- Thermoelectric performances of the as-synthesized Te-PEDOT:PSS NWs. Electrical conductivity, Seebeck coefficient and power factor are shown in graphs (a) and (b) as a function of AR. There appears to be a clear correlation between *AR* and performance where the highest performing set of wires having an *AR* of 73, demonstrate a power factor of ~130 uW/mK^2. In order to better understand the driving forces behind this trend, conductivity and Seebeck coefficient as a function of average NW length and diameter are shown in panels (c) and (d) respectively. While there is a distinct lack of trend between conductivity and NW length, a dependency can be observed as a function of NW diameter. Vertical errors bars are the standard deviations between triplicate measurements.

Figure 3.4- Representative TGA plot showing the decomposition of the organic component beginning at 200°C during a heat ramp to 600°C. Once the weight percent curve levels off it is indicative of the entirety of the organic phase having been removed to leave only the inorganic component behind.

Figure 3.5- *AR* histograms for Te NWs synthesized with 3 different molecular weights of PVP. Panel (a) corresponds to PVP-29 wires, (b) PVP-40 NWs and (c) PVP-55 NWs. Insets shown within panels (a), (b), and (c) are cumulative distribution functions representative of the increase in size distribution spread as larger molecular weight of PVP are used to synthesize wires.

Figure 3.6- Nanowire length size distribution histograms depicting the general closeness in lengths apparent for all three systems at play.

Figure 3.7- Diameter histograms for Te NWs synthesized with 3 different molecular weights of PVP. To further demonstrate differences in NW diameter, panels (a), (b), and (c) are shown for PVP-29, PVP-40 and PVP-55, respectively.

Figure 3.8- Power factor versus average nanowire length and diameter. This plot demonstrates the distinct sensitivity to diameter that these hybrid Te-PEDOT:PSS nanowire systems demonstrate compared to the impact of tuning nanowire length.

Figure 4.1- Material structure and thermoelectric properties measurement scheme. (a) A HRTEM micrograph distinguishing between the PEDOT:PSS shell and the inorganic Te core. The inset is an SAED pattern confirming the single crystal nature of the Te nanowire and its crystallographic structure and orientation. (b) Scanning electron micrograph depicting the suspended pad measurement platform utilized to probe the thermoelectric properties of the hybrid nanowire, where the artificial coloration is used to aid in distinguishing between components. (c) Visualization of the crystallographic space group that the Te core forms with the different facets shown and the (001) direction along the nanowire axis of growth. (d) The top portion of the cartoon schematics depicting thermal transport occurring through the inorganic core while electronic carrier transport occurring through the organic shell, and the bottom portion of the panel illustrating the proposed hypothesis of better organic templating on narrower nanowire diameters being the cause for the observed enhanced charge mobility.

Figure 4.2- Room temperature electrical transport properties. Measured room temperature electrical conductivity and Seebeck coefficient are plotted as a function of wire diameter for different Te-PEDOT:PSS core/shell nanowires. The measured results of Te-PVP core/shell nanowires, represented by the hollow symbols, are also plotted for comparison. Note that PVP is an electrical insulator, and similar to the Te-PEDOT:PSS wires, the PVP layer thickness is kept ~1.14 ± 0.36 nm in Te-PVP nanowires while only the Te core diameter is varied. Here, the measurement uncertainties of σ is mainly from the uncertainties in nanowire length and diameter measurements, and uncertainties of S is mainly from the uncertainties in linear least square fitting.

Figure 4.3- Kang-Snyder model on temperature dependent electrical transport properties. (a-b) Measured temperature dependent Seebeck coefficient and electrical conductivity of Te-PEDOT:PSS hybrid nanowires with different diameters. (c) Reduced chemical potential $\eta = (E_F - E_t)/k_B T$ of different diameter Te-PEDOT:PSS nanowires plotted as a function of temperature. (d) $ln(\sigma_{E0})$ is plotted as a function of $T^{-0.5}$, and hopping energy W_γ is extracted by taking the slope of $ln(\sigma_{E0})$ vs $T^{-0.5}$ curve.

Figure 4.4- Gate modulated electrical conductivity measurements. (a) Measured source drain current normalized with respect to the ratio of nanowire shell cross-sectional area over length ($I_{DS}^*=I_{DS}/(\pi Dt/L)$) of three Te-PEDOT:PSS core/shell nanowires as a function of gate voltage, V_G, where the source drain voltage, V_{SD}, is kept at 0.2 V. Inset: schematic drawing of the device. (b) Hole mobility, μ, plotted as a function of nanowire diameter, D. Inset: SEM image of the device used for the gated electrical conductivity measurements. The measurement uncertainties of μ is mainly from the uncertainties in nanowire length and diameter measurements.

Figure 4.5- Thermoelectric properties of hybrid nanowires. (a) Temperature dependent thermal conductivity of Te-PEDOT:PSS and Te-PVP nanowires with different diameters, where the measured room temperature thermal conductivity for bulk Te is also plotted for comparison [1]. The dashed lines are modeled thermal conductivity of each nanowires considering the effects of phonon-boundary scattering. (b) Size-dependent thermoelectric figure of merit, ZT, of Te-PEDOT:PSS hybrid nanowires at room temperature. (c) Temperature-dependent ZT of Te-PEDOT:PSS hybrid nanowires with various diameters. (d) Size-dependent thermal conductivity and power factor of Te-PEDOT:PSS hybrid nanowires at room temperature, which show inverse relationship with respect to the nanowire diameter. Here, the measurement uncertainties of κ is mainly from the uncertainties in nanowire length and diameter measurements, and the uncertainties of ZT is calculated based on the respective uncertainties in S, σ, and κ.

Figure 4.6- Organic shell thickness characterization. HRTEM micrographs and SAED insets for nanowires of diameter (a) 101 nm and (b) 177 nm showing crystalline structure. HRTEM micrographs showing representative images of the shell thickness of (c) Te-PEDOT:PSS and (d) Te-PVP hybrid nanowires.

Figure 4.7- Measured average shell thickness and calculated standard deviation for Te-PEDOT:PSS hybrid nanowires with different diameters.

Figure 4.8- Contact thermal resistance characterization. The inset is a SEM image showing a Te-PEDOT nanowire bridging the two suspended side-by-side membranes with all four contacts bonded with EBID Pt deposits. The scale bar of the SEM image is 2 μm.

Figure 4.9- Schematic drawing showing a nanowire sample placed to bridge the gap of the two suspended membranes.

Figure 4.10- Double radiation shield scheme. (a) Schematic drawing showing the inside of the cryostat. (b) A picture showing the approach of mounting the additional radiation shield on the sample holder. Photo Credit: Lin Yang, Lawrence Berkeley National Laboratory.

Figure 4.11- Measured total thermal conductance, G_{bg+nw}, background thermal conductance, G_{bg}, and the sample thermal conductance after the background subtraction, G_{nw}, for the 57 nm diameter Te-PEDOT core/shell nanowire.

Figure 4.12- Linear fitting to obtain electrical resistance and Seebeck coefficient. (a) Measured *I-V* curve for the 118 nm diameter Te-PEDOT:PSS nanowire at 300 K, where the solid line is the fitted curve using the linear least square fitting approach. (b) Measured temperature difference and induced Seebeck voltage for the same nanowire at 300 K. The Seebeck coefficient is obtained by fitting the slope of the data points using the linear least square fitting method.

Figure 4.13- Parallel circuit model calculation. (a) Calculated electrical conductivity using the parallel circuit model in comparison with the measured results. Inset: schematic drawing showing the cross-section of the Te-PEDOT:PSS hybrid nanowire. (b) Calculated Seebeck coefficient using the parallel model in comparison with the measured results.

Figure 4.14- Electrical circuit diagram for the hybrid core-shell nanowire under a temperature gradient ($T_h - T_s$), where $V_{SB,shell}$ and $V_{SB,core}$ are shell and core Seebeck voltage, respectively, R_{shell} and R_{core} are shell and core electrical resistance respectively. V_{SB} represents the measured open circuit Seebeck voltage.

Figure 4.15- Gate modulated electrical conductivity measurements. (a) Drain source current (I_{DS}) versus drain source voltage (V_{DS}) under different gate voltage V_g, the linear I-V curve showing Ohmic behaviors of the contacts. (b) Measured source drain current of three Te-PEDOT:PSS core/shell nanowires as a function of gate voltage, where the drain source voltage is kept at 0.2 V.

Figure 4.16- Schematic drawing showing the device setup used for gated modulated Seebeck coefficient measurements.

Figure 4.17- Gate modulated Seebeck coefficient measurements. (a) Circuit diagram showing the measurement scheme for the thermometer calibration. (b) Measured voltage with lock-in 1 for the near side thermometer plotted as a function of heating voltage. (c) Circuit diagram showing the measurement scheme for the Seebeck coefficient measurement. (d) Measured Seebeck voltage plotted as a function of heating voltage under different global back gate voltage.

Figure 4.18- Seebeck coefficient of Te-PEDOT:PSS nanowire measured under different gate voltage.

Figure 4.19- Thermal transport in hybrid nanowires. (a) Comparison of the room temperature modeled thermal conductivity with the measured results for Te-PEDOT:PSS hybrid nanowires of different diameters. (b) Calculated heat flux ratio flowing through the shell to that of the total core/shell nanowire as function of wire diameter.

Figure 5.1- Normalized UV-Vis-NIR spectra of the pristine polymers, and the F4TCNQ solution doped (50 mM) and vapor doped films, (a) P3RT, (b) P3RSe, (c) P3RTe, and (d) P3HT. The dashed lines in each panel show the peak locations of CTC (teal lines *ca.* 364, 685 nm), residual F4TCNQ dopant (green lines *ca.* 390 nm) and ICT (orange lines *ca.* 410, 760, 875 nm).

Figure 5.2- XPS analysis for select P3RX films. Heteroatom scans for each polymer (a) S-2p spectra in P3RT, (b) Se-3d spectra in P3RSe, (c) Te-3d spectra in P3RTe, and (d) S-2p spectra in P3HT, all demonstrate a blue shift upon doping. (e) Deconvoluted N-1s spectra of 50 mM doped polymers reveal the relative intensities of N^0 species (teal fitted peak centered at ~399.5 eV) versus the N^{-1} peak (orange fitted peak centered at ~ 398 eV). The strong presence of N^{-1} in both P3RTe and P3HT further corroborates that ICT is the dominant doping mechanism for these two polymers, as opposed to P3RT and P3RSe which show reduced or no intensity.

Figure 5.3- (a) GIWAXS of pristine polymers of P3RT, P3RSe, P3RTe and P3HT, (b) nearly out-of-plane line cut, and (c) in-plane line cuts. The strong (h00) peaks visible in (b) along with the pronounced (010) peaks in (c) provide clear support of preference for edge-on orientation for all the polymers except P3RSe which shows both edge-on and face-on alignment. Out-of-plane line cuts are shown for (d) P3RT, (e) P3RSe, (f) P3RTe, and (g) P3HT both before and after vapor doping with F4TCNQ. Both P3RT and P3RSe show (h00) peaks shift to higher Q after doping, indicative of a contraction of the lamellar spacing. P3RTe and P3HT show the lamellar stacking peak shift to lower Q, indicating an expansion in lamellar spacing and suggestive of F4TCNQ dopant intercalating into the alkyl side chains leading to ITC doping.

Figure 5.4- Thermoelectric properties as a function of heteroatom and doping. (a) Electrical conductivity, (b) Seebeck coefficient, (c) Jonker curve comparing this study (P3RTe-F4TCNQ) with our previously reported P3RX-$FeCl_3$ dataset. Error bars, when present, represent the sample-to-sample standard deviation.

Figure 5.5- UV-Vis-NIR spectra of pristine and F4TCNQ doped films. (a) P3RT, (b) P3RSe, (c) P3RTe, (d) P3HT.

Figure 5.6- ATR-FTIR spectra of F4TCNQ doped films. vapor doped ((a) and (b)) and 50 mM solution doped ((c) and (d)) poly(alkyl chalcogenophenes) thin films. (a) and (c) Annotated MIR spectra. (b) and (d) Zoomed-in MIR spectra, highlighting the cyano absorbances and charge transfer mechanisms.

Figure 5.7- 50 mM (a) P3RT, (b) P3RSe, (c) P3RTe and (d) P3HT heteroatom deconvolutions. Orange peaks indicate blue shifted populations that interact with the F4TCNQ dopant whereas the yellow peaks are indicative of the neat populations.

Figure 5.8- F4TCNQ:Heteroatom doping ratio. X-labels represent the doping conditions, where number (*e.g.* 1, 12, 50) represent the solution concentration in mM, and "V" represents vapor. Error bars represent the standard deviation as calculated from the F-1s and N-1s spectra.

Figure 5.9- Depiction of in-plane and nearly out of plane sector integrations.

Figure 5.10- Nearly out-of-plane GIWAXS (100) peak line cuts for (a) P3RT, (b) P3RSe, (c) P3RTe, and (d) P3HT before and after vapor doping. Both (a) and (b) demonstrate that the doublets observed before doping are also present after doping as well.

Figure 5.11- Analyzing neutral F4TCNQ in GIWAXS line cuts. Zoomed in GIWAXS nearly out-of-plane line cuts of F4TCNQ doped P3RT, P3RSe, P3RTe and P3HT demonstrate the consistent nature with which sharp peaks appear that are indicative of neutral F4TCNQ molecules in the polymer thin film at the time of the measurement.

Figure 5.12- Calculating coherence lengths. Full width half max (Δq) determination in order to calculate coherence length. Panel a) shows Δq of the different (h00) reflections plotted as a function of h^2 and a line of best fit finding the intersection point with the y-axis. The intercept is then used as the Δq in the Scherrer formula to determine coherence length. This method is appropriate to use based upon inspection of panel b) peak breadth ($q-q_o$), which shows a distinct broadening of higher order reflections. Higher order broadening indicates that peak width is impacted not only by grain size but also by other effects such as thermal fluctuations, thus utilizing the y intercept rather than (100) value for Δq is more accurate and helps to negate over estimation of coherence length that might occur.

Figure 5.13- Thermal activation energies for electrical conductivity. Error bars represent sample to sample standard deviations. All doped films demonstrated statistically significant activation energies, with a 95% confidence interval. Grey line represents k_BT at 300 K.

Figure 5.14- Electrical conductivity (a) and Seebeck coefficient (b) of full doping ladder. Error bars, when present, represent sample to sample standard deviations.

List of Tables

Table 3.1 Diameter, length and aspect ratio for Te NWs synthesized using different PVP MWs, as determined by SEM for *n* > 50 NWs of each kind.

Table 3.2 Gel permeation chromatography (GPC) performed on neat starting PVP polymers as acquired from Sigma Aldrich. We report the number averaged and weight averaged molecular weight (M_n and M_w, respectively) and the polydispersity ($D=M_w/M_n$) for the three PVP samples. The values reported in the table were obtained using an instrument calibration performed with poly(ethylene oxide) standards. To obtain accurate Mn and Mw values, the instrument should be calibrated with PVP standards, but these were not readily available. Therefore, the absolute value of M_n and M_w values are not expected to be consistent with the nominal values provided by Sigma Aldrich, but comparisons between the three samples is valid.

Table 3.3 Comparison of power factors and aspect ratios (calculated from the reported dimensions in each paper) for the composite nanowires presented in this paper and analogous undoped systems from the literature.

Table 4.1 Electrical transport parameters for Te-PEDOT:PSS core/shell nanowires with different diameters.

Table 5.1- Coherence lengths corresponding to lamellar stacking (h00) and pi-pi stacking (010).

Acknowledgements

The work discussed in this dissertation is a culmination of many years of collaboration, conversation, guidance, patience, learning and kindness. I owe a great deal of gratitude to the many people who made this dissertation possible.

Firstly, I am incredibly grateful to my advisors Dr. Jeff Urban and Prof. Junqiao Wu. Their support, wisdom and encouragement has been invaluable to me. Jeff generously first took me on as a SULI intern, something I am so incredibly thankful for. I never could have anticipated how life changing that opportunity would be and while I was initially only meant to stay for 3 months, I ended up staying in the Urban group for 6 years. Jeff's infectious enthusiasm for science and out of the box thinking always kept me on my toes and encouraged me to approach problems creatively. Junqiao and the entire Wu group have been incredibly generous and helpful, I've truly enjoyed being a part of their group meetings and expanding my scientific understanding through learning about the work they do. In addition to scientific research, I've also had the good fortune of working with Junqiao to make AS&T a more equitable and thriving graduate group for future students. His passion and commitment to AS&T and its students is truly inspiring and has been a joy to work with.

In addition to my mentors, I am also grateful to all of my collaborators. I have been so incredibly fortunate to get to work with some of the most wonderful graduate students, post-docs and professors both locally here at Berkeley and beyond. Some professors I'd like to mention that I am deeply grateful to are Prof. Dave Attwood and Prof. Chris Dames. Dave has done so much for AS&T and has provided me with such wonderful mentorship throughout my time at Berkeley. Chris' class on microscale heat transfer transformed the way I viewed my research and the open and welcoming way that he taught the course content not only effectively conveyed the information but also inspired me to become a better communicator. Both Dave and Chris have been amazing committee members and I am so grateful for their kind and genuine support.

Within the Urban group, Eddy Zaia was my first graduate student mentor when I joined and his friendship, patience, guidance and support was a major inspiration and motivation for me to pursue graduate school. Along with Eddy, the entire Urban group made my experience so welcoming and truly made the group feel like home. I have to express my appreciation to thermoelectric folks past and present, Ayash Sahu, Boris Russ, Jason Forster, Peter Yang, Carlos Forsythe, Chaochao Dun, Nelson Coates, Jaeyoo Choi, Heng Wang, Woochul Lee, and Pengyu Yuan for all the expertise, discussion and support. And of course, the rest of the group members I overlapped with, Ngoc Bui, Erin Creel, Chih-Hao Hsu, Sohee Jeong, Fen Qui, Zhuolei Zhang, and many more who all made coming to work each day such a positive, invigorating experience. Thank you to Mook Kang, Lukas Hackl, and Alex Bruefach for all their support and comradery, having them as fellow grad students through this journey has been a true pleasure. I've also been extremely lucky to work with some fantastic undergrad researchers, Valerie Niemann, Kyle Haas and others. Kyle, thanks for being such a stellar undergraduate researcher and always having so much enthusiasm.

Working at the Molecular Foundry has been an absolute dream come true, giving me access to world class lab facilities and enabling me to work with some of the brightest and most generous scientific minds. I owe a heartfelt thanks to all the Molecular Foundry Staff, particularly Tracy Mattox, Tev Kuykendall, Anne Pham, Tina McCoy, Suksham Barun, David Hohm, and Virginia Altoe. They keep the Foundry up and running smoothly, even when having to navigate a global pandemic, yet somehow still find the time and energy to answer all my questions with a smile.

I have been exceedingly fortunate to work with some fantastically talented collaborators who have now turned into good friends. Thanks to Akanksha Menon for her eternal willingness to read through manuscript drafts, brainstorm ideas, provide guidance, and most importantly be such a dear friend. Her talent and patience are unrivaled, and her future students are so incredibly lucky to have her as a guide for their own journeys. It has been such a pleasure to also work with Lin Yang, Shawn Gregory, Greg Su, Alex Buyanin and so many others. Their enthusiasm, passion and commitment to scientific excellence has been such a huge source of brilliance for me, I could not have asked for a better group of collaborators.

I'm incredibly grateful to my dear friend Derek Popple, he has provided so much support (both technical and emotional), and comradery through all of grad school, as well as laughter and light even when things were feeling dark. Additionally, I owe a huge thanks to all AS&T students, especially Emma Regan, Rachel Woods-Robinson, Carlos Biaou, Liona Fan-Chiang, and Akel Hashim, for helping me to overcome the inevitable challenges we all face in grad school and making this journey so much more fun.

It would be thoughtless of me to not also take a moment to acknowledge past mentors, Prof. David Boucher and Dr. Joey Robertson, as their support and guidance is what got me to Berkeley in the first place. I was a bit of a scientific late bloomer. I didn't partake in research until the summer before my senior year of undergrad. Thankfully, Prof. David Boucher was willing to not only take a risk on a completely untrained student but also go the extra mile for me to get things lined up last minute. He instilled in me a love for laboratory research, the scientific method and physical chemistry and gave me the confidence to take risks and speak up about my scientific ideas which has aided me throughout my scientific career.

And most importantly, I of course want to thank my family. Their love, support, and encouragement have gotten me to where I am today and have shaped who I am as a person. My partner has been such a rock for me during this entire process and continues to inspire me every single day with his passion for learning, dedicated work ethic, enthusiasm for adventure and constant kindness. My parents have taught me so much. My mother has always been my biggest advocate and motivator and instilled in me a love for analytical thinking and data driven processes from day one. Her intelligence, strength and generosity are just a few of her many wonderful attributes that I try to embody every day. My father has taught me the importance of effective communication, a love for art, music, and cooking as well as the significance of always finding beauty and wonder in even the simplest things. My late grandfather, Stanley, has always been a major source of inspiration for me, while his doctorate degree is medical in nature (he was a radiologist) his passion for learning always motivated me to pursue more education. And while I might not have realized it growing up, hearing about his radiological work is part of what motivated me to pursue learning so much about x-ray scattering techniques. I also want to thank my cousin Sarah, reconnecting with her during my PhD has been such a joy for me.

I truly am so incredibly lucky.

Chapter 1. Introduction

There has been a global proliferation of low power devices ranging from personal electronics and biosensors to the internet-of-things.[2] With the advent of the COVID-19 pandemic, the importance of these personal electronic devices, especially those with biosensing capability (e.g. O2 pulse-ox sensor, heart rate monitor, blood sugar, etc.) has become further apparent. However, with smart electronics appearing in smaller and smaller device geometries, long-lasting power sources with flexible form factors are a growing area of focus.[2,3] Soft thermoelectrics (TEs) are poised to fill this gap while also offering the potential of drawing energy from the human body.[4–6] TE materials can be integrated into thermoelectric generators (TEGs), devices capable of transforming thermal gradients into useful electrical power, or Peltier devices capable of generating localized heating or cooling by applying an electrical current. In addition to acting as small flexible power sources for electronics, TEGs are also appealing for a wide variety of applications, such as complimentary devices to be paired with existing heat engines in an effort to boost power generation efficiency as the planet faces a growing energy crisis.

Within the field of soft TEs there are still unanswered questions surrounding material design and the fundamental physics driving charge and heat transfer that need to be answered before soft TEs can reach their full potential. This dissertation focuses extensively on the development and understanding of soft TE materials in order to aid in the establishment of design principles upon which future cutting edge materials can be based. However, before diving into soft TE materials specifically, Chapter 1 begins with a bigger picture look at the history of TE's and an explanation of basic principles. This ensures the reader has a good grasp of the topic before tackling a discussion of the challenges that TE materials face, ultimately motivating a conversation on emerging areas developed to tackle these challenges. Finally, a brief overview of the chapters of this dissertation is provided. Ultimately, in order to fully appreciate the need for soft materials, the promising attributes they offer and the challenges they inevitably face, it is important to first begin with a bigger picture look at the field of TEs as a whole and Chapter 1 aims to provide that bigger picture snapshot.

1.1 Thermoelectric History

The phenomenon of the TE effect was reported as early as the 18th century. Italian physicist and chemist, Alessandro Guiseppe Antonio Anastasio Volta is widely credited with discovering the TE effect in 1794 with his study on the electromotive force originating from the temperature difference between a junction of two dissimilar conductors.[7] While Volta is ascribed the discovery, Johann Seebeck is arguably a more well-known figure within TE history due to the electromotive force generated from a temperature gradient being named after him.[8] As time progressed, the understanding surrounding the TE effect grew and developed, with contributions from William Thomson,[9] William Strutt Rayleigh,[10] Edmund Altenkirch,[11] Jean Charles Athanase Peltier,[12] Ludwig Boltzmann, Lars Onsager,[13,14] and many others. In the 20th century, great interest was placed upon developing TEGs and Peltier coolers in order to act as power sources or precise temperature controllers for a variety of different applications that fit different historical needs, such as for optoelectronics and deep space missions.

Heavily doped semiconductors were quickly identified as the most promising group of materials for TE use and the standout materials were the chalcogen-based alloys antimony telluride, bismuth telluride, and lead telluride. While these materials offered benchmark performances, TEs were plagued with low efficiencies of only 5%. With the advent of the lithium-ion battery, many major hopes for TEGs were quashed. Only applications that required long-lived, solid-state power still relied upon TEGs. One area that TEs have found great success is deep space missions where photovoltaic power is not possible. Here, TE's still suffer from low efficiency, but due to the very large temperature gradient that can be generated between ambient deep space and a radioactive heat source, sufficient power can be achieved. TEGs have been directly employed in a number of different deep space missions and have even been left on the moon in order to power devices remaining there for scientific monitoring.[15]

By the mid-to-late 20th century, the excitement surrounding TEs had died off until the 1990's when two MIT physicists, Hicks and Dresselhaus, published a series of papers positing the theoretical potential of nanostructuring for enhancing TE material performance.[16–19] These theories breathed new life into the field of TE research and the hunt for novel materials and cutting edge performances began once again. Now, in the 21st century, as the planet faces a growing energy crisis and finite fuel sources, the majority of attention placed on TE research is no longer positioned upon TEGs as independent power sources, but instead focuses upon the potential for TEs to act as a complimentary device to existing engines in order to boost efficiency.

1.2 Basic Principles

The TE effect is the phenomenon of a charge gradient building up within a semiconducting material as a result of an applied thermal gradient. Charge carriers on the hot side of the material have more kinetic energy, causing them to migrate to the cold side. This migration results in a charge gradient developing across the material which in turn causes the movement of electrons which can be harvested as a current. To transform this phenomenon into a device capable of generating power, two semiconducting legs, one n-type (electron rich) and one p-type (electron deficient), are electrically connected in series and thermally connected in parallel. When a thermal gradient is applied to this device configuration, it is possible to connect an electronic device in need of power as demonstrated in **Figure 1.1a**. Putting many of these p-, n- leg pairs together in conjunction with a heat sink can greatly increase the operating voltage of the module while reducing its electrical current, thus enabling greater power generation.

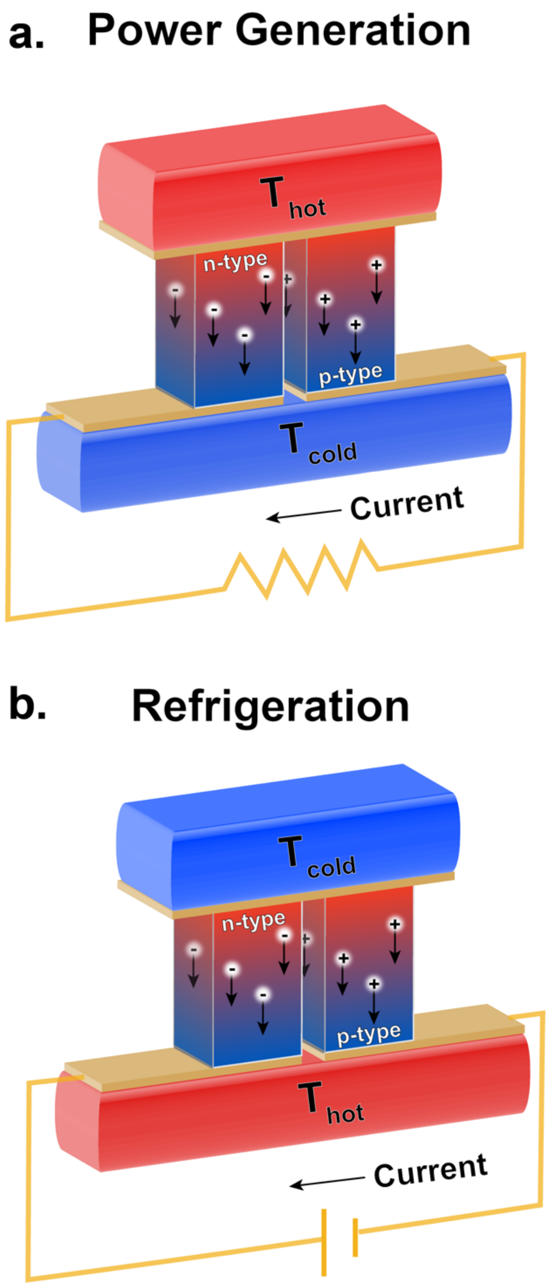

Figure 1.1- A TE module schematic a. showing the migration of charge carriers (- indicates electrons, + indicates holes) from the hot side to the cold side under (a.) power generation configuration and (b.) under a Peltier cooling configuration.

TE performance is ultimately described by a dimensionless figure of merit, ZT,

$$ZT = \frac{S^2 \sigma T}{k}$$

where S is the material's Seebeck coefficient (μV/K), σ is the electrical conductivity (S/cm), k is the thermal conductivity (W/mK), and finally T is the average temperature of the hot and cold sides of the device (K). Often times the product of the numerator, $S^2\sigma$ is utilized and referred to as the Power Factor.

In addition to power generation, a TE device can also be utilized in such a way that it generates a temperature gradient by applying an electrical current and operating in reverse. The movement of the applied current through the TE materials (with no applied temperature gradient) causes endothermic and exothermic processes to occur at the semiconductor-metal junctions via the Peltier effect, as demonstrated in **Figure 1.1b**. The Peltier coefficient can be defined as follows,

$$\Pi = S * T$$

Regardless of whether being used for power generation or solid-state cooling, the ideal TE material has a high σ and very low k, a type of material often described as a "phonon-glass, electron-crystal".[20] Low k materials are preferred in order to maintain the greatest possible thermal differential across the device. By enlarging this thermal gradient, the amount of heat that can be converted into electricity is maximized. High σ is critical in order to minimize the parasitic heat flow losses that that arise as a result of thermal conduction and inevitable Joule heating. Joule heating (I^2R) is generated by the thermoelectric current, I, flowing through the individual semiconducting legs with a resistance, R.

The third critical variable to consider in terms of a TE material's performance is the Seebeck coefficient. The Seebeck coefficient, also known as the Thermopower, is a measure of the material's ability to maintain a voltage potential, ΔV, given an applied temperature difference. Giving the Seebeck coefficient the generalized form,

$$S = -\frac{dV}{dT}.$$

The dominant charge carrier (either electrons or holes) involved in electrical transport within a specific leg dictates the sign of S. Therefore, if electrons are the majority, S will be negative and vice versa for holes being the dominant charge carrier.

The efficiency of a TEG and Peltier cooler is expressed with respect to the Carnot efficiency, which is the maximum efficiency a heat engine can achieve when operating between two temperatures,

$$\eta = \frac{\Delta T}{T_h} \times \frac{\sqrt{1 + Z\bar{T}} - 1}{\sqrt{1 + Z\bar{T}} + \frac{T_c}{T_h}}$$

$$COP = \frac{T_c}{\Delta T} \times \frac{\sqrt{1 + Z\bar{T}} - \frac{T_h}{T_c}}{\sqrt{1 + Z\bar{T}} + 1}$$

where η is the carnot efficiency of a TEG, ΔT is the temperature difference applied to the device, T_h and T_c are the temperatures of the hot and cold side, respectively, $\bar{T}$ is the average temp at which the device is operating, and COP is the coefficient of performance for a Peltier module.[21,22]

In terms of device efficiency, TEs are notoriously low, typically plagued with efficiencies below 10%. Assuming a TEG of ZT~1, at T_c= 20 °C, and at T_h=37 °C, the device would be ~0.6% efficient. To put this in perspective, the human body can be considered a heat engine able to produce ~100 W of thermal energy under basal metabolic conditions.[23,24] With the human body as a heat source, a ΔT=17 °C, and assuming optimal operating conditions, it would be possible to harvest a power density of ~30 μWcm^{-2}. This is well within the necessary power needs of many small electronic devices, as power needs for microelectronics has decreased significantly as of late, with some wireless biological sensors requiring as low as 1 μW to operate.[25] However, while using TEGs as power sources for microelectronics appears incredibly promising, their small size demands the need for conformal or flexible device geometries not necessarily available with traditional, rigid, inorganic TEs. This reveals a major need for the development of high performing soft TE materials.

1.3 Challenges

TE materials inevitably suffer from low device efficiencies. To combat these low efficiencies, researchers are constantly seeking higher performing materials to integrate into the devices. For traditional inorganic TE materials, the challenge with this endeavor is the inherent coupling between the critical material parameters of electrical conductivity, Seebeck coefficient and thermal conductivity. These parameters are intrinsically linked and, in some cases, inversely correlated. In order to boost σ, the traditional routes follow the Drude model, $\sigma = \mu n q$, (μ is the carrier mobility, n is the carrier concentration, q represents elemental charge) and focus upon enhancing either μ or n. While this is an effective strategy for σ enhancement, depending on the type of material, S will decrease in response and k will increase. The relationship between these three parameters plotted over a wide range of carrier concentrations is shown below in **Figure 1.2a**.

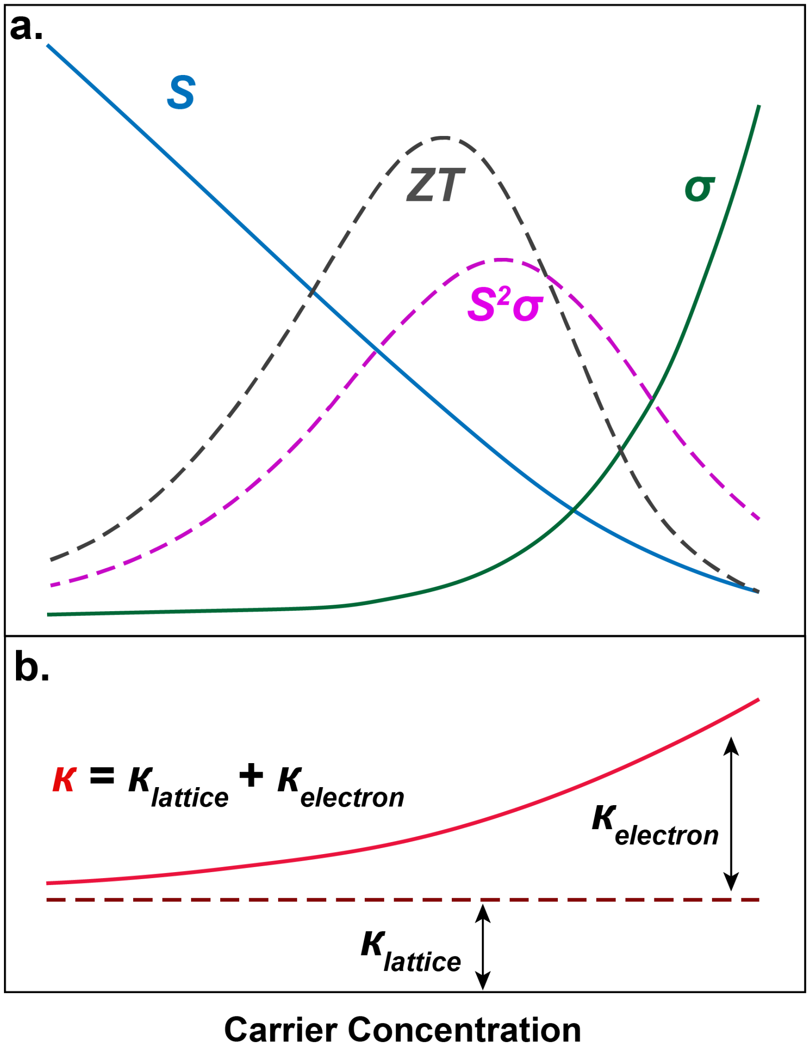

Figure 1.2- Visual representation of the relationship between the three major thermoelectric properties, Seebeck coefficient, thermal conductivity, and electrical conductivity as a function of carrier concentration. Panel a. shows the common tradeoffs between the properties for traditional materials, making overall device performance, *ZT*, quite challenging to enhance. Also shown plotted is Power Factor, $S^2\sigma$, which is often used as a general stand in for *ZT*. Panel b. shows the relative contributions to the total thermal conductivity, k, from the lattice thermal conductivity, $k_{lattice}$, and the electronic thermal conductivity, $k_{Electron}$, as a function of carrier concentration.

Therefore, rather than enhancing ZT outright, usually performance enhancements come as a result of parameter optimization. There are a number of techniques that have gained attention due to their promise of being able to enhance either electrical conductivity or Seebeck coefficient while minimizing thermal conductivity. Nanostructuring is one such technique where the differences in electron and phonon mean free paths are exploited and a sharpening of the density of states is leveraged.[17] Phonons typically travel longer distances than electrons before scattering, thus by quantum confining bulk materials it is possible to preferentially scatter phonons and reduce the thermal conductivity without detriment to the electrical conductivity, providing an effective route to decoupling these two parameters. When transitioning from a traditional bulk inorganic material that demonstrates band-like transport to a quantum confined one, the electronic density of states changes shape to become sharper. A sharper density of states will give rise to a higher Seebeck coefficient, as will be further described in Chapter 2. This concept has given rise to an entire field of study and has proven to be quite effective for traditional inorganic materials such as Bi_2Te_3 and PbTe,[26,27] and has enabled the demonstration of *ZT*s upwards of 1.5.[20,28,29]

While techniques such as nanostructuring have provided great results for inorganic materials to overcome historic performance limitations, they do not address all of the challenges that traditional TE materials face. These inorganic rare earth elements (*e.g.* Bi_2Te_3 and PbTe) are inherently expensive and energy intensive to process and produce devices with rigid form factors.[30–34] Therefore, even with *ZT* enhancements, TE deployability is still very limited and there is a clear need to move away from these materials entirely. With the advent of soft electronic materials, greater attention has been paid to developing these types of novel materials for TE applications in order to access solution processability, lower material cost and conformal device geometries.

1.4 Emerging Areas

The field of soft TE materials encompasses both the area of purely organic small molecules and polymers as well as hybrid organic-inorganic composite type materials. By incorporating some percentage of carbon, not only will the TE material likely achieve reduced material costs, ease of manufacturing and heightened flexibility, but often times novel transport mechanisms arise as well. Transport demonstrated in organic and hybrid materials offers the possibility of decoupling S, σ and k. However, before delving more deeply into the transport dynamics of organic and hybrid materials (discussed in Chapter 2), it is important to first understand what the material landscape for soft TEs looks like.

Organic semiconductors can demonstrate a wide range of transport phenomenon, from insulating to semi-metallic (as demonstrated in **Figure 1.3**) and have demonstrated great amenability to novel device architectures such as textiles and conformal arrays.[23,35–37] In addition to their superior processability, organic based TEs also offer novel charge transport mechanisms that deviate from traditional inorganic band-like transport.[23] A number of organic semiconductors have shown promise as TE materials, including but not limited to, polyaniline (PANI), poly(3,4-ethylenedioxythiophene) (PEDOT), and poly(3-hexylthiophene) (P3HT) derivatives.[23,38,39] While these polymers show promise on their own, to achieve appreciable levels of electrical transport they must be doped. Unlike with inorganic materials, organic semiconductors must be chemically doped with small molecules in order to increase the carrier concentration and the level of doping is radically higher than for inorganic semiconductors. One system that has found a wide amount of success through doping is PEDOT. When paired with polystyrene sulfonate (PSS) or Fe(III) tris-*p*-toluenesulfonate (Tos), PEDOT can become not only solution processable but also demonstrate high degrees of performance with electrical conductivities achieved upwards of ~4600 S/cm.[40]

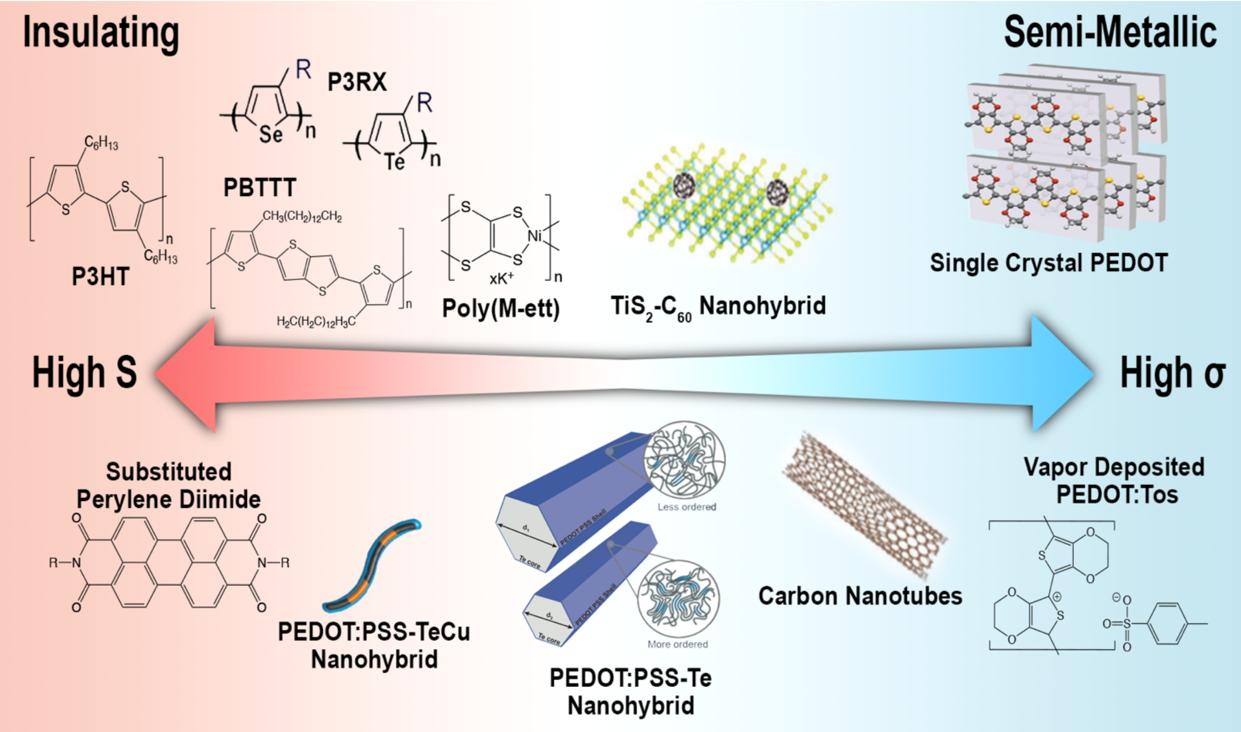

Figure 1.3- A general schematic depicting the landscape of organic and hybrid materials in terms of the sliding scale of Seebeck coefficient and electrical conductivity.

While many organic semiconductors have comparable concentrations of electrons and holes, making them ambipolar, often times the carrier sign (n-type or p-type) is determined by the ability to dope that material in a stable manner. P-type organic semiconductors are far more prevalent than n-type carriers. This is due to the electron affinity of most organic materials being relatively small. With a small electron affinity, negatively charged molecules tend to become unstable and as a result, rather than doping the organic semiconductor and making those charges available to participate in charge transport, will instead react with water or oxygen in the environment. [23,41,42] This results in limiting the optimal n-type organics to perylene diimide (PDI), naphthalene diimide (NDI) and fullerene derivatives which all demonstrate larger electron affinities.[43–46] While performance still lags behind that of their p-type counter parts, there has been some progress made in developing stable n-type organic based materials. One such material is a poly(metal 1,1,2,2-ethenetetrathiolate) (poly(M-ett)) derivative, a conjugated polymer with metal ions in the backbone to achieve a power factor of 66 $\mu W m^{-1} K^{-2}$.[47,48]

Organic-inorganic hybrid TEs are yet another emerging area of materials that hold promise for novel transport mechanisms, added processability and heightened tunability. These materials leverage the synthetic tunability of their inorganic constituents while also enabling flexible form factors and low thermal conductivity inherited from their organic component.[49] The classic sign of a hybrid material is significantly enhanced performance that is a result of non-linear interactions occurring at the nanoscale interfacial layer forming between the two constituents.[50,51] The result is a new material class that offers tunable material interfaces with performances otherwise unattainable within additive-exclusive composite materials.[50] *In-situ* growth has traditionally been the most effective avenue for producing hybrid materials that demonstrate synergistic performance enhancements. This method utilizes the organic component as the nucleation directing agent for the inorganic species to result in well-formed nanostructures with a well adhered organic layer coating the surface.[50,52–55]

Within the category of p-type hybrid materials, tellurium nanowires coated with PEDOT:PSS (PEDOT:PSS-Te) are especially well studied. In 2010, See *et al.* initially reported on the synthesis of PEDOT:PSS-Te nanowires to find that the hybrid material demonstrated a surprisingly high electrical conductivity and could achieve an impressive ZT ~0.1.[52] Since that time there have been many studies performed on this system exploring the effect on performance of tuning the nanowire dimensions,[50,55] the impact of forming copper sub-phase alloys,[54] and studies probing the fundamental physics at play.[51,53] Recently, we published a study on the TE performance of single PEDOT:PSS-Te nanowires which has helped to reveal critical insights into the fundamentals of charge and thermal transport within the system and demonstrated a single wire ZT~0.54 at 400 K, one of the highest reported ZTs for a hybrid material to date.

In terms of n-type hybrid materials, current progress has been quite limited. Interestingly, due to Tellurium's ambipolar nature, Te nanowires are a promising starting point for developing n-type hybrid materials. Sahu *et al.* demonstrated the ability to resurface Te nanowires, opening up the possibility to adhere new organic species to the inorganic surface.[50] Zaia *et al.* utilized a similar methodology with the n-type small molecule PDI to achieve a power factor of 17.5 $\mu Wm^{-1}K^{-2}$.[56] In 2020, another study by Sahu *et al.* demonstrated coating the Te nanowire surface with molecular sulfur (S) to achieve unprecedented n-type power factors of ~500 $\mu Wm^{-1}K^{-2}$.[57] By coating the Te nanowires in S, they posit that a hybridized sub-band is created which shrinks and shifts the bandgap such that the material demonstrates n-type transport. Beyond Te nanowire-based hybrids, another promising material was reported by Tian *et al.* when combining C_{60} fullerenes with TiS_2.[58] This material was able to achieve power factors of ~400 $\mu Wm^{-1}K^{-2}$ which when integrated into a device was able to generate 350 nW of power under a 20 K temperature difference. These enhancements in performance hold great promise for the field of n-type hybrid development. To illustrate the inequity between n-type and p-type materials, **Figure 1.4** plots both the Seebeck coefficient versus electrical conductivity and power factor versus conductivity for the latest literature of organic and hybrid TE materials with respect to their best performing inorganic counterparts. For the S vs σ plot, the linear line shown in black highlights the curious $S \propto \sigma^{-\frac{1}{4}}$ power law which is discussed later in Chapter 2.

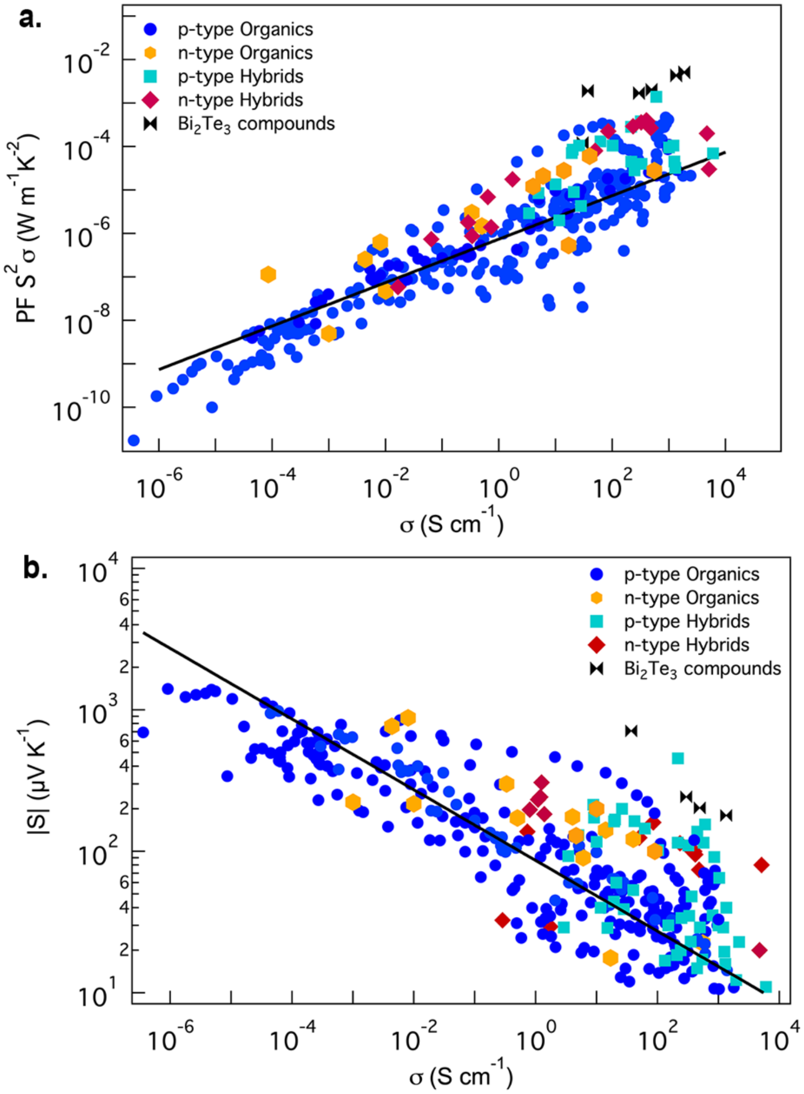

Figure 1.4- Overview of the TE properties of a wide sampling of performances reported for organic and hybrid materials.[23,37,59–68] The Seebeck coefficient (top) and power factor (bottom) are plotted as a function of electrical conductivity. Bi_2Te_3 compound performances are plotted as well in order to provide references to the benchmark industry standard material.

1.5 Outline and Summary of Core Dissertation Chapters

The overarching goal of this dissertation is to establish design rules upon which next generation hybrid materials can be based. This is done by investigating the fundamental charge transport physics at play in soft TE systems and exploring the three following questions.

1. How can we synthetically establish better control over hybrid material dimensions and how do those dimensions impact TE performance?
2. Where is charge and heat transport specifically occurring within a model hybrid system?

3. How can we better understand and tune organic morphology and the corresponding electronic properties?

In Chapter 2, I introduce the fundamental phenomenon driving thermoelectric transport along with a focus upon the physical properties of different classes of materials that dictate their behavior. Given the overarching focus upon soft material transport physics, I have summarized the current models utilized to explain the physics at play. The information detailed in this chapter serves as a knowledge basis which the following chapters build upon.

Chapter 3 details our systematic investigation of the impact of hybrid nanowire diameter and length on overall thermoelectric performance, as modulated through surface ligand molecular weight. Contrary to previous literature reports, we found that shrinking nanowire diameter appears to offer far larger performance enhancements than large increases in nanowire length. This finding suggests that diameter control is a highly effective route for enhancing thermoelectric performance in hybrid materials.

In Chapter 4, in order to better understand the fundamental driving forces behind the insights garnered from Chapter 3, we defined a well-controlled single nanowire hybrid model system. These single nanowire measurements are the first of their kind to be applied to this type of hybrid material and helped to provide the first ever experimental confirmation of charge transport occurring through the organic conducting shell and thermal transport moving through the inorganic nanowire core. Additionally, this study demonstrated unmatched thermoelectric performance, achieving a ZT~0.5. This further emphasizes the importance of establishing a better understanding and control over the morphology of the organic polymer shell.

In Chapter 5, in order to expand upon our understanding and control over the organic polymer shell morphology, we first endeavor to explore the impacts of heteroatom substitution as a knob for control the electronic and structural landscape of polythiophene derivatives. From this study we have established a better understanding of the physical underpinnings driving certain types of polymer-dopant interactions.

Chapter 2. Transport Fundamentals

While soft TE materials hold great promise for overcoming the challenges faced by traditional inorganic TEs, significant improvements are still necessary in order to truly rival the performance of their inorganic counter parts. The secrets to unlocking higher performances in soft TE materials lay in better understanding the fundamental transport physics at play. As a result, Chapter 2 provides a detailed transport discussion. Because transport in organic and hybrid materials is complex, approaching the physics first from a more well understood inorganic perspective will be helpful in order to establish the fundamental concepts at play. Once that foundation is laid, organic and hybrid electronic transport is discussed along with the theoretical models commonly applied to them. And lastly, a brief discussion of thermal transport is provided as well in order to afford the reader with a wholistic understanding of both charge and heat transfer.

2.1 Inorganic Charge Transport

Traditional TE transport has long been based upon bulk inorganic materials that exhibit long range order. Electrical conductivity can be represented in a simplistic form, as previously mentioned, according to the Drude model, $\sigma = \mu n q$. However, periodicity enables the delocalization of charge carriers throughout the material and leads to band-like transport which enables more rigorous forms of electrical conductivity to be constructed. According to the classical theory of conduction for band-like transport, electrical conductivity can be mathematically represented in the following manner,

$$\sigma_{bulk} = -\frac{e^2}{3}\int v^2 t_s \frac{\partial f_o}{\partial E} g(E) dE$$

where e is the charge constant, v is the charge carrier velocity, t_s is the time between scattering events, f_0 is the equilibrium Fermi-Dirac distribution function, and $g(E)$ is the energy dependent electronic density of states. This function can be further simplified to

$$\sigma_{bulk} = -\frac{e^2}{3}\int \sigma\,(E) dE$$

and is referred to as the energy dependent differential electrical conductivity, $\sigma(E)$. A simplified version of the combination of these functions is shown graphically in **Figure 2.1** below.

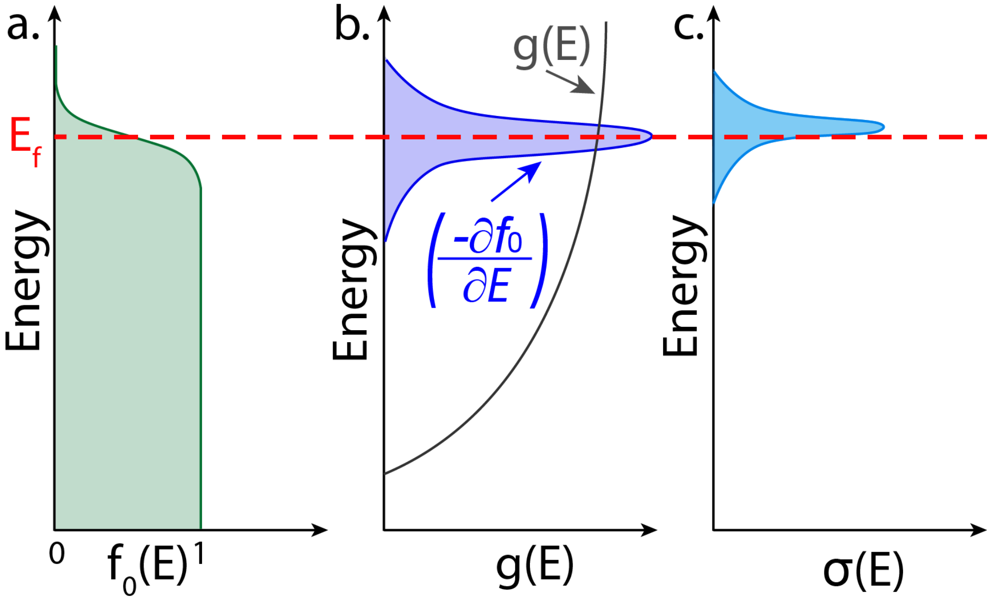

Figure 2.1- A graphical representation of the energy dependent electrical conductivity for a traditional material exhibiting band-like transport. Panel a. depicts the Fermi probability distribution function with the Fermi level (also referred to as the chemical potential) marked by the red dashed line. Panel b. demonstrates the resulting distribution from the partial derivative of the fermi distribution function with respect to energy, centered about the fermi level. In panel c., by multiplying the function shown in b. by the density of states *g(E)*, an offset distribution (shown in bright blue) appears which is representative of the carriers energetically available to participate in charge transport.

The Fermi-Dirac distribution function represents the distribution of charge carriers in a certain material, and the Fermi level (E_f, also referred to as the chemical potential), shown in **Figure 2.1a** by the red line, is the point at which there is a 50% probability of a certain state being filled. This position is noteworthy because only carriers with energy close to E_f participate in charge transport and the Fermi level can be tuned via doping. For the sake of simplicity, v and t_s will be assumed to be energy independent, leaving $\frac{\partial f_o}{\partial E}$ and *g(E)* as the main energy dependent terms. The negative partial derivative, -$\frac{\partial f_o}{\partial E}$ results in the Gaussian distribution about E_f shown in **Figure 2.1b**. In order to visualize the charge carriers available to participate in charge transport, this function must be multiplied by *g(E)* in order to accurately represent the states available for the charge carriers to occupy. Giving rise to the offset distribution shown in green in **Figure 2.1c** and whose integral is proportional to the total energy dependent electrical conductivity.

The Seebeck coefficient is somewhat more complex because it requires considering a material not only under an electrical potential (as is done for electrical conductivity) but also a thermal potential. The differential electrical conductivity is also present in the Seebeck coefficient as,

$$S_{bulk} = -\frac{1}{eT}\frac{\int v^2 t_s\left(E - E_f\right)g(E)\frac{\partial f_o}{\partial E}dE}{\int v^2 t_s g(E)\frac{\partial f_o}{\partial E}dE} = -\frac{1}{eT}\frac{\int \sigma(E)\left(E - E_f\right)dE}{\sigma}$$

This expression reveals the inverse relationship between *S* and σ and demonstrates that the Seebeck coefficient is a measure of the asymmetry in the distribution of hot carriers (higher energy, above E_f) and cold carriers (lower energy, below E_f). This emphasis on asymmetry demonstrates the importance of Fermi level positioning in order to maximize the greatest degree of asymmetry which often occurs closer to the band edge of a material in order to enhance *S*. While this is an avenue to enhance *S*, it also further emphases the inverse relationship with σ since electrical conductivity will decrease as fewer carriers are available to participate in transport. This relationship is the underlying driving force behind why metals typically have a low *S* but high σ, whereas insulators have a high *S* and low σ.

2.2 Organic Charge Transport

Organic semiconductors demonstrate varying degrees of disorder, therefore the ease with which a charge carrier can move through the material is highly dependent upon electronic coupling and structural morphology, making their transport vary drastically from well-ordered inorganic systems. This deviation necessitates the need for an extensive understanding of the transport complexities present and ultimately the development of unique organic specific transport models. Due to the lack of long-range periodicity in organic electronic materials, charge carriers are typically forced to hop from one discrete localized state to another. This hopping-like transport can occur along the conjugated backbone of the molecule or polymer, however, eventually a carrier's conductive progression will be forced to move to a new discrete organic body. The overlap between molecular orbitals of separate molecules or polymer chains is dictated by much weaker interactions, such as van der Waals bonding, than those of the covalently bonded backbone. Of these weaker interactions, π-π stacking, when molecules or polymer chains order themselves with strong overlap of their π orbitals, typically offers the best degree of electronic "communication".[23] While π-π stacking is conducive to charge transport, it inevitably creates a larger energetic barrier that carriers must overcome even for systems with relatively high levels of crystallinity.[69] As a result of this highly localized electronic landscape, the electronic structure for organic systems can no longer be represented as band continuums. Instead, the electronic structure is often described as discrete states with a highest occupied molecular orbital (HOMO) and lowest unoccupied molecular orbital (LUMO) which can be likened to a traditional semiconductor's valence and conduction states, respectively.[23] Given these weak intermolecular interactions, rather than representing the density of states as a parabolic band, as is tradition for many inorganic semiconductors, organic density of states are often described more broadly with a Gaussian distribution.

Due the spatial and energetic disorder resulting in highly localized electronic states and relatively wide bandgaps, organic semiconductors tend to be fairly electrically insulating. This creates the need for carriers to be added to the system in order to bring about appreciable degrees of charge transport.[23] However, this process is not as straightforward as it is for covalently bonded solids. The addition of carriers to the π orbitals can cause geometric distortions in the organic backbone, referred to as polarons. A polaron is a type of quasiparticple made up of a charged species paired with a lattice vibration. Depending on the organic system in question, electrons or holes may no longer be the majority charge carrier, but instead polarons or bipolarons (the aggregation of two polarons) might dominate.[69,70] This change in dominant charge carrier radically impacts charge transport dynamics and can cause reductions in mobility that lead to carrier self-trapping.[69]

Given the complexities of these organic systems, mathematical models to explain their fundamental charge transport has been a challenge and those that do exist tend to only apply to materials when a narrow set of conditions are met. Examples of such models include nearest neighbor hopping (NNH), variable range hoping (VRH) and Mott's mobility edge model (MMEM).[71–73] The NNH model is able to describe a transport regime where the carrier hopping rate is limited by spatial tunneling distances, causing the carrier to only be able to hop to states immediately nearest them. This model is most applicable to polymers which are lightly doped and demonstrate an exponential Arrhenius dependence relation between temperature and electrical conductivity. Alternatively, VHR describes transport where carriers choose to hop to sites that are farther away than nearest neighbor sites. This type of hopping is driven by a large mismatch in energetic energies which usually arises in heavily doped organic systems. Mott's mobility edge model is useful for metallic-like transport for carriers excited beyond a particular mobility edge but inevitably tends to provide overestimates for electrical conductivity. Each of these models have their own respective shortcomings and furthermore, fail to effectively capture transport trends for semiconducting polymers over multiple orders of magnitude of conductivity and can be increasingly challenging to effectively tease out the fundamental phenomenon at play.[74]

One model put forth by Kang and Snyder in 2017 aims to treat semiconducting organic transport in a more general form in an attempt to capture the full range of conductivity trends for a broader variety of polymers.[74] To achieve this degree of generality, a transport function $\sigma_E(E)$ is defined from which electrical conductivity, σ, can be expressed as,

$$\sigma = \int \sigma_E(-\frac{\partial f_o}{\partial E})dE$$

$$\text{where} \qquad \sigma_E(E,T) = \sigma_{Eo}(T) \times \left(\frac{E-E_t}{k_B T}\right)^s \text{ when } (E < E_t)$$

$$\text{or} \quad \sigma_E(E,T) = 0 \text{ when } (E > E_t)$$

this transport function encompasses $\sigma_{Eo}(T)$, the temperature dependent but energy independent transport coefficient, E_t, the transport edge which defines the transport energy of charge carriers below which no electrons or holes contribute to transport even at finite temperatures, s the transport parameter, k_B the Boltzman constant and T the temperature. By defining a transport edge, it is possible to differentiate between thermally activated hopping carriers above and below this point, thus aptly capturing transport in insulating organic semiconductors where the chemical potential is below E_t. When the chemical potential is above E_t, the form of $\sigma_E(E)$ alters due to its dependency on the density of states, carrier velocity and scattering time which all demonstrate varying power law relationships to the energy of the carrier above E_t. As a result, the s parameter becomes the key component introduced to help modulate the function in order to account for the energy dependence of the carrier above the transport edge. Thus, enabling the Kang-Snyder model to be applicable to such a wide range of conduction transport.

According to this model the Seebeck coefficient can also be expressed in terms of the transport function;

$$S = \frac{1}{\sigma}(\frac{k_B}{e})\int(\frac{E - E_F}{k_B T})\sigma_E(-\frac{\partial f}{\partial E})dE$$

From this form it is apparent that the Seebeck coefficient is highly dependent on the carrier concentration and the energetic landscape of the material. Due to the fact that $\sigma_E(E,T)$ is dependent on the charge transport mechanism, the temperature dependence of S can also vary. Interestingly, this model makes it is possible to recover the power law $S \propto \sigma^{-\frac{1}{4}}$, a reoccurring universal empirical relationship that arises for a myriad of different TE materials that had previously alluded modelling efforts.

While the Kang-Snyder model is undoubtedly the first of its kind to effectively address modelling a larger range of polymer transport, it does inevitably have shortcomings. A number of studies have revealed inconsistencies between experimentally collected values and predictions made by the model.[75–78] The source of these shortcomings are likely buried in the model's treatment of carrier concentration and the transport parameter s. The Kang-Snyder model claims that the transport coefficient σ_{Eo} is constant for a given material system, thus overlooking the potential impact that carrier concentration might have upon that term. Additionally, while the vast majority of polymers fit to an s=3 power law, in reality this would require $E_F - E_t$ ≥1 eV. While this may be accurate for very low carrier concentrations, it seems unphysical at even moderate doping levels given the relatively narrow bandwidths for most semiconducting polymers. Alternatively, s=1 yields more plausible $E_F - E_t$values, but inevitably, if used to fit the vast majority of semiconducting polymers, would no longer produce a good fit with experimental data.

To combat these challenges, Gregory et al. recently produced a new model that builds upon the architecture that Kang and Snyder initially established.[79] This model is known as the semi-localized transport (SLoT) model and seeks to provide a better fit to experimental data while also providing more fundamental physical insight into the mechanisms at play. The SLoT model augments the transport function to include a carrier concentration ratio, *c*.

$$\sigma_E(E,T,c) = \begin{Bmatrix} 0, (E < E_t) \\ \sigma_0 \exp\left(-\frac{W_H(c)}{k_B T}\right) \times \left(\frac{E - E_t}{k_B T}\right), (E \geq E_t \end{Bmatrix}$$

where $W_H(c)$ is the potential energy barrier a hopping carrier must overcome to participate in transport. Previously, the Kang-Snyder model treated the W_H term as constant and independent of carrier concentration. The SLoT model authors argue that this is insufficient because in real physical systems the potential energy barrier is expected to decrease with increasing carrier concentration.[76,80–84] As a result of adding this $W_H(c)$ function to the energy independent term of σ_E, it is possible to now better fit experimental data with the s term being set equal to 1 which yields physically reasonable chemical potentials. Interestingly, this model was also applied to doped carbon nanotube data and was found to be in good agreement.[79] This suggests that this model may be even more broadly applicable to a wider variety of materials than initially anticipated and offers the possibility of a truly universal model. However, given the young age of the SLoT model, only time will tell if it can truly stand up to these claims.

2.3 Hybrid Charge Transport

Hybrid systems inevitably have effects from both the organic and inorganic components which result in a fairly complex and challenging system. This necessitates a full understanding of the impacts of morphology and carrier energetics upon transport in both parent systems before any assumptions can be made about the hybrid system. The hard-soft hybrid interface can be characterized by the discrete molecular orbitals of the organic component mixing with the inorganic's band of continuum states. Ultimately, charge transfer at this unique interface gives rise to non-linear interactions that are a defining feature for transport and result in the classic calling card of hybrid materials, synergistic performance enhancements.[85] The exact physical underpinnings responsible for these performance enhancements, however, are not well understood and are still a hot topic of debate.[52,54,63,86]

There are three general schools of thinking when it comes to understanding the observed synergistic performance enhancements for hybrid systems, energy filtering,[52,54,87] interfacial charge transfer[51,63,87–90] and templating[51,63,90]. Energy filtering is an effect that has generated a lot of attention in the last decade,[52,54,87] the concept leverages a slight energetic offset between the organic and inorganic components in order to create a potential energy barrier which only allows hot carriers to pass through the interface. By screening out the lower energy carriers it is possible to enhance the Seebeck coefficient (by boosting the asymmetry between hot and cold carriers) with only a minor decrease in electrical conductivity. Due to the quadratic dependence on the Seebeck coefficient, this enhancement can theoretically lead to major increases in overall *ZT*. However, energy filtering is quite challenging to conclusively identify as a significant contributor. In fact, a number of studies have been published suggesting that the role of energy filtering has been over estimated in the hybrid literature.[51,91]

Interfacial charge transfer implies that at the inorganic-organic interface some extent of band bending occurs, causing charge accumulation at the interface, leading to the inorganic species being doped by the organic component or vice versa.[51,88] Doping in this manner, if the inorganic species was assumed to be the component being doped and the main avenue for charge transport, would reduce the impact of scattering events from impurities, causing higher carrier mobility as well as localized regions of higher carrier concentration at the interface.[88] This phenomenon would lead to heightened electrical conductivity. Alternatively, if the organic phase were to be assumed to be the predominant channel for charge transport, then it would experience a de-doping effect (removal of charge carriers) that would give rise to a higher Seebeck coefficient.[51,90] In order to achieve this sort of doping it is essential that there is proper matching of organic to inorganic energetics to ensure that charge transfer between these two species is spontaneous.[88]

Organic templating is another effect that has been implicated as playing a role in hybrid material TE transport. Due to the natural surface energy of the inorganic nanostructure's exposed facet, the organic phase will preferentially order itself upon the surface of the inorganic material.[51,63,90] The idea of organic molecules or polymers assembling themselves to be more or less well ordered based upon the surface energy of the inorganic substrate or architecture is well established in the organic electronic literature.[92–94] However, these cases traditionally rely upon bulk inorganic materials, not nanostructures. If charge transport is presumed to occur through the organic layer, then a boost in electrical conductivity would be expected due to the heightened mobility as a result of the higher degree of crystallinity. However, the phenomenon of templating is exceedingly challenging to experimentally validate in most hybrid materials due to the ultra-thin nature of the organic shell sitting upon a highly crystalline inorganic core.[90]

In terms of mathematically describing charge transport in hybrid materials, few models exist. One such popular model applied to multicomponent systems is the effective medium theory, which predicts that the Seebeck coefficient of the new material must lie between that of the individual parent components.[95] While this model is highly applicable to composite materials, it is unable to effectively predict performances for hybrid materials because it cannot capture the non-linear interactions that occur at the hard soft interface of hybrids. Interestingly, the Kang-Snyder model, discussed at length in the previous Organic Transport section, has also been effectively applied to some hybrid materials such as PEDOT:PSS-Te and PEDOT:PSS-CuTe nanowires.[51,90] The applicability and fit of this model, of course, suggests that the majority of charge transport must be occurring through the organic PEDOT:PSS shell rather than the inorganic core. However, great amounts of debate still exist surrounding the best way to explain TE transport in organic-inorganic hybrid materials.

2.4 Thermal Transport

Thermal transport is another critical component that must be considered for a TE material. Thermal conductivity is a representation of how well a certain material is able to conduct heat. Given that thermal conductivity, k, is in the denominator of ZT, it is important that k be minimized. But to do this effectively, one must first establish an understanding of what drives thermal transport and how it propagates through different types of materials. As previously mentioned in Chapter 1, k is comprised of an electron ($k_{electron}$) and phonon (k_{phonon}) contribution. Thermal transport is highly dependent upon the ordering and bonding strength between atoms because heat can be thought move through a material as quantized lattice vibrations, referred to as phonons.

For insulators, k is predominantly made up of k_{phonon} and can be represented mathematically as,[96,97]

$$\kappa = \frac{1}{3} C \nu \Lambda$$

where C is the specific heat capacity of the material, ν is the group velocity and Λ is the phonon mean free path. The specific heat capacity can be derived mathematically from the material's density of states and thus is highly dependent on the dimension of the material in question. The specific heat capacity is defined as the amount of heat required to raise the temperature of 1 kg of a material by 1 K. For a bulk, 3D material C will demonstrate a cubed power law dependence and as dimensionality shrinks so does the magnitude of the power law. Λ is how far a phonon can travel before it undergoes a scattering event, typically there are three different scattering events that can cause changes in Λ. Those scattering events are boundary scattering, impurity scattering and Umklapp scattering. While the first two are fairly straight forward, the third may be less familiar. Umklapp scattering is phonon-phonon scattering that only occurs when the phonons have a high enough energy to scatter off of one another inelastically. These three scattering mechanisms can be combined to form Λ via Mathieson's rule as,

$$\Lambda^{-1} = \Lambda_{boundary}^{-1} + \Lambda_{impurity}^{-1} + \Lambda_{umklapp}^{-1}$$

For a highly electrically conductive material the electronic contribution to k is far more significant and is intimately coupled with electrical conductivity through the Wiedemann-Franz Law,

$$\kappa_e = LT\sigma$$

where L is the Lorenz number. The Lorenz number is very much system dependent as,

$$L = \frac{\pi^2}{3}\left(\frac{k_B}{e}\right)^2$$

but is usually equal to 2.44×10^{-8} WΩK^{-2}.[96] The Wiedemann-Franz law was originally derived assuming an ideal electron gas model, therefore it holds well for metals but does not always fit well when applied to organic based systems.[98–100]

Organic semiconductors, due to their inherently disordered nature and low electrical conductivity, tend to have relatively low k values (~0.1-0.5 Wm^{-1}K^{-1}, as opposed to a metal such as copper with a k~400 W/mK) and are typically dominated by phonon based thermal transport.[99,101–103] Hybrid materials however are very poorly understood in terms of thermal behavior, in fact often times k is assumed to be quite low for these kinds of soft materials and only the Power Factor is readily investigated. This is a result of challenges surrounding thermal conductivity measurement techniques for probing thin film samples.[37,103] The most common thermal conductivity measurements for thin films include time domain thermoreflectance (TDTR) and the 3ω-method.[104] Both of these methods most effectively measure the out-of-plane thermal conductivity, however electrical conductivity measurements are probed in the through-plane direction. Thus, given the anisotropic nature of soft TE materials, measuring these two properties not in the same direction is concerning. A report on PEDOT:PSS has shown that the in-plane thermal conductivity is up to three times greater than the out-of-plane value.[99] For hybrid materials very few thermal conductivity reports can be found in the literature, raising the question of how accurate claimed ZT values truly are. Performing more studies where thermal and electrical conductivity can be probed in the same direction is an area of the utmost importance.

In addition to advancements in thermal metrology, exploring thermal transport in hybrid materials is critical in order to maximize overall TE performance and efficiency. Without a detailed understanding of where and how heat propagates through the material, it is challenging to predict which phonon scattering techniques (*i.e.* nanostructuring, etc.) might be most relevant for decreasing overall thermal conductivity. This dissertation endeavors to aid in bridging these knowledge gaps by performing carefully designed, systematic thermal measurements in the same direction as charge transport measurements. Simultaneously bringing about a better understanding of where and how phonon propagation is occurring and providing a more accurate *ZT* value for a model hybrid material. Further discussion of thermal transport in hybrid materials is provided in Chapter 4 where a systematic study of a single hybrid nanowire is detailed.

2.5 Conclusions

This discussion surrounding charge and heat transport helps to set the stage for the work detailed in this dissertation. There are many outstanding questions surrounding fundamental transport in soft TE materials, especially hybrids. While hybrid materials hold the potential for realizing novel transport physics, the non-linear interactions occurring at the organic-inorganic interface are not well understood and there is significant debate in the literature around explanations for the exact physical underpinnings. This lack of clarity makes the design of new cutting-edge hybrid materials quite challenging and ultimately inhibits these materials from reaching their full potential. The goal of this dissertation is to provide experimentally verified clarity surrounding soft material transport by rationally establishing a better understanding of structure-function relationships. To do this, we begin by establishing an understanding of structure-performance relationships in hybrid materials. This is done by first developing a synthetic technique for tuning the dimensions of such materials and then tracking the resulting TE performance changes that might arise, as is detailed in Chapter 3.

Chapter 3. Modulation of nanowire diameter and thermoelectric performance via synthetically tuning ligand molecular weight

Adapted from "Understanding Diameter and Length Effects in a Solution-Processable Tellurium-PEDOT:PSS Hybrid Thermoelectric Nanowire Mesh," M.P. Gordon, K. Haas, E. Zaia, A.K. Menon, L. Yang, A. Bruefach, M. Galluzzo, M.C. Scott, R.S. Prasher, A. Sahu, J.J. Urban, *Advanced Electronic Materials,* 2021, 7, 3. (DOI:10.1002/aelm.202000904) with permission of the authors. *Reproduced with permission of Wiley.*

3.1 Abstract

Organic-inorganic hybrids offer great promise as solution-processable thermoelectric materials. However, they have struggled to surpass the performance of their rigid inorganic counterparts due, in part, to a lack of synthetic control and limited understanding of how inorganic nanostructure dimensions impact overall charge transport. While it has been hypothesized that length, diameter, and aspect ratio (AR) all impact electronic transport in hybrid nanowires, the field lacks clarity on the relative role of each. In this study, the experimental parameter of ligand molecular weight is investigated as a synthetic knob for modulating nanowire dimensions, as well as the deconvolution of nanowire length versus diameter impacts on electron transport. By increasing ligand molecular weight, larger nanowire AR dispersions occur and an optimal power factor of ~130 $\mu\text{Wm}^{-1}\text{K}^{-2}$ is achieved for a modest AR of 73. Power factors of this magnitude were thought to only be achievable in ultra-high AR systems, our system represents a 183% increase in performance over literature reports with similar AR. Additionally, nanowire diameter is demonstrated to be a far more sensitive parameter for enhancing performance than modulating length. This study provides improved fundamental insight into rational synthetic design avenues that will enable future enhancements in the performance of hybrid materials.

3.2 Introduction

Hybrid thermoelectrics (TEs) are attractive as they combine the low thermal conductivity and solution processability of organic materials with the structural and electronic tunability of inorganic nanostructures.[23,37,49] These materials enable the realization of flexible and printable novel devices that can harness unconventional heat sources, such as body heat, to generate electricity or provide solid-state cooling with the promise of cost-effective solution-based manufacturing.[37,105,23,35,36,106,54,56] The true sign of a hybrid material is significantly enhanced performance as a result of non-linear interactions that occur at the nanoscale interfacial layer formed between the two constituents.[50,51,54,56] This results in a new material class that offers tunable material interfaces with performance otherwise unattainable within simple composites.[50,107]

The performance of a TE material is characterized by a dimensionless figure of merit, $ZT = \frac{(S^2\sigma)}{\kappa}T$, comprised of its Seebeck coefficient S, electrical conductivity σ, thermal conductivity κ, and the absolute temperature T. The quantity $S^2\sigma$ is known as the power factor and denotes the electronic performance of the TE material. The most widely studied hybrid material is tellurium (Te) nanowires (NWs) coated with poly(3,4-ethylenedioxythiophene) polystyrene sulfonate (PEDOT:PSS). This Te-PEDOT:PSS system effectively leverages the high electrical conductivity of PEDOT:PSS and a high Seebeck coefficient attributed to Te, to achieve power factors of ~145 μWm^{-1}K^{-2} for NWs with ultra-high aspect ratios (*AR* = length, *L*/diameter, *D*) ~1000 without any extrinsic doping.[50]

Typically, high *ARs* are achieved by dramatically increasing NW length which leads to a decrease in interfacial scattering events. [50,108,109] However, diameter also often changes in these studies, so it is unclear whether length or diameter is the true driving force behind the observed performance enhancements. Recent studies have shown that charge transport is dominated by the organic phase within the Te-PEDOT:PSS hybrid NW, and the improvement in TE performance is attributed to the interaction of the polymer with the inorganic NW surface.[51] This interaction results in the self-assembly (alignment or templating) of the polymer along the crystalline facets of the inorganic NW, which is governed by differences in surface energy at the hard-soft interface.[51] It is well-established that surface energy has a size dependence,[110,111] however to date, little work has been done to explore the role of NW diameter and length in enhancing the performance of hybrid thermoelectric materials.

A study by Yee *et al.* attempted to deconvolute the contributions of NW length and diameter on the TE properties of these hybrid bulk films, but were unable to effectively separate the effects due to a lack of synthetic control with the standard one-pot Te-PEDOT:PSS nanowire synthesis.[112] Te-PEDOT:PSS NWs have traditionally been synthesized exclusively with PEDOT:PSS as the nucleation directing surface ligand.[52–54,112] Given that PEDOT:PSS is a commercial polymer blend, the tunability and control of such a synthesis is limited.[112] An alternative approach for synthesizing Te NWs uses polyvinylpyrrolidone (PVP) as the surface ligand[113–116], and this has been shown to provide added degrees of synthetic control in other analogous NW systems.[117–119] For example, Zeng *et al.* demonstrated that well-defined high *AR* silver nanowires could be synthesized by modulating PVP molecular weight (MW).[120] While PVP is not an optimal polymer coating for Te NWs owing to its electrically insulating nature, it imparts synthetic tunability as a myriad of PVP MWs are commercially available.[121,122] Sahu *et al.* proposed a synthetic process for ligand exchange that is tailored specifically to converting nanowires of Te-PVP to Te-PEDOT:PSS, which are of interest for thermoelectric applications.[50,57]

Herein for the first time, we vary the ligand MW to study its effect on Te NW size, as well as the thermoelectric performance of the resulting Te-PEDOT:PSS NWs post ligand exchange. We find that increased PVP MW results in larger NW *AR* dispersions where NW length remains relatively constant but diameter decreases, and an optimal power factor of 130 μW/mK^2 is achieved at a modest *AR* of 73. Such high performance is in contrast with previous reports of the same hybrid material synthesized via different means, wherein an ultra-high *AR* of ~1000 was required for a comparable power factor.

3.3 Results and Discussion

The synthesis used in this work is depicted in **Figure 3.1a**, which yields NWs of uniform surface morphologies as shown in **Figure 3.1b**. **Figure 2.1c** shows a high-resolution transmission electron microscopy (HRTEM) micrograph of the core-shell structure of the PVP polymer coating the Te crystalline core prior to the ligand exchange.

Three different PVP MWs were used in the nanowire synthesis (29 kDa, 40 kDa and 55 kDa) to produce batches of Te NWs with PVP as the surface ligand that are referred to as PVP-29, PVP-40 and PVP-55. ln the next step, the system undergoes a series of ligand exchanges (Figure

3.1a), to yield a hybrid material predominantly composed of a Te NW core encapsulated by the conducting polymer PEDOT:PSS shell (**Figure 3.1c**). This ligand exchange process does not always result in samples with exactly the same ratios of inorganic to organic constituents, thus organic to inorganic weight percent was corrected by adding excess PEDOT:PSS and quantified *via* thermogravimetric analysis (TGA, **Figure 3.4**). The different batches of NWs synthesized were found to have differing diameters and roughly constant lengths owing to the use of different PVP MWs. As shown in **Table 3.1,** PVP of different MWs results in a large range of NW diameters but a small range of lengths, ultimately yielding different *ARs*. The results tabulated in Table 1 are displayed in histogram form in **Figure 3.5**, **3.6**, and **3.7**. PVP-40 clearly demonstrates the smallest average diameter size and tightest size distribution.

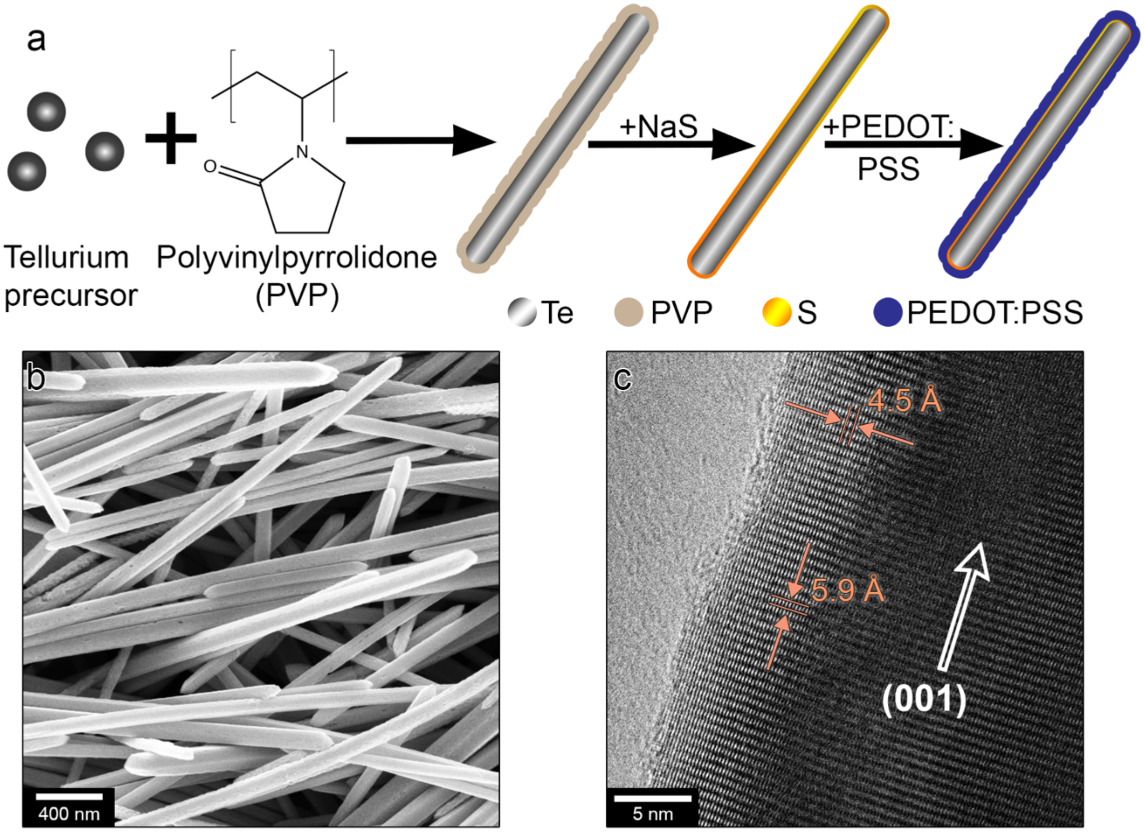

Figure 3.1- Depiction of the synthetic process employed, paired with SEM and HRTEM micrographs depicting the structure of the Te-PVP coated NWs. Panel (a) shows a general cartoon schematic of the multi-step synthetic process for forming the hybrid nanostructures. A representative scanning electron micrograph shows the microscale morphology of the Te-PVP NWs in panel (b). Panel (c) depicts a representative transmission electron micrograph of the Te-PVP wire which shows the thin polymer layer on the surface of the inorganic core and distinctly shows the lattice fringes indicative of atomic spacings in the unit cell.

Table 3.1 Diameter, length and aspect ratio for Te NWs synthesized using different PVP MWs, as determined by SEM for *n* > 50 NWs of each kind.

Sample	Diameter (nm)	Length (μm)	Aspect Ratio
PVP-29	109 (±84)	4.6 (±2.3)	42
PVP-40	56.9 (±16)	4.2 (±1.6)	73
PVP-55	83.0 (±50)	5.6 (±3.2)	68

Inspection of SEM panels a, b, and c in **Figure 3.2** illustrate the visual differences that arise between each system. Powder X-ray diffraction (PXRD) run on each of the film sets confirms that the NW cores are entirely composed of Te and that the inorganic trigonal crystal structure is consistent between batches, **Figure 3.2d**.

Insight into the cause for increase in *ARs* as a function of PVP MW can be explained using a study performed by Xu *et al.* that provides a careful analysis of the nucleation dynamics of PVP with respect to the Te surface.[119] They estimate binding energy preferences of PVP to certain crystal planes of Te according to a theoretical framework established by Fichthorn *et al.* and find a linear correlation between increasing number of PVP monomer units and an increasing preference for binding onto the (100) and (101) planes rather than the (001) plane.[123] Thus, suggesting that for larger PVP MWs there is less of a likelihood for a PVP unit to bind to the (001) plane (the plane perpendicular to and intersecting with the axial direction of growth) that ultimately leads to larger *AR* NWs. While Xu *et al.* did not experimentally observe a dramatic difference in NW dimensions when using different PVP MWs, their synthetic process is carried out in water as opposed to ethylene glycol (which was used in this study), therefore it is possible that differences in solvent viscosity alter the nucleation kinetics between their findings and the current work.

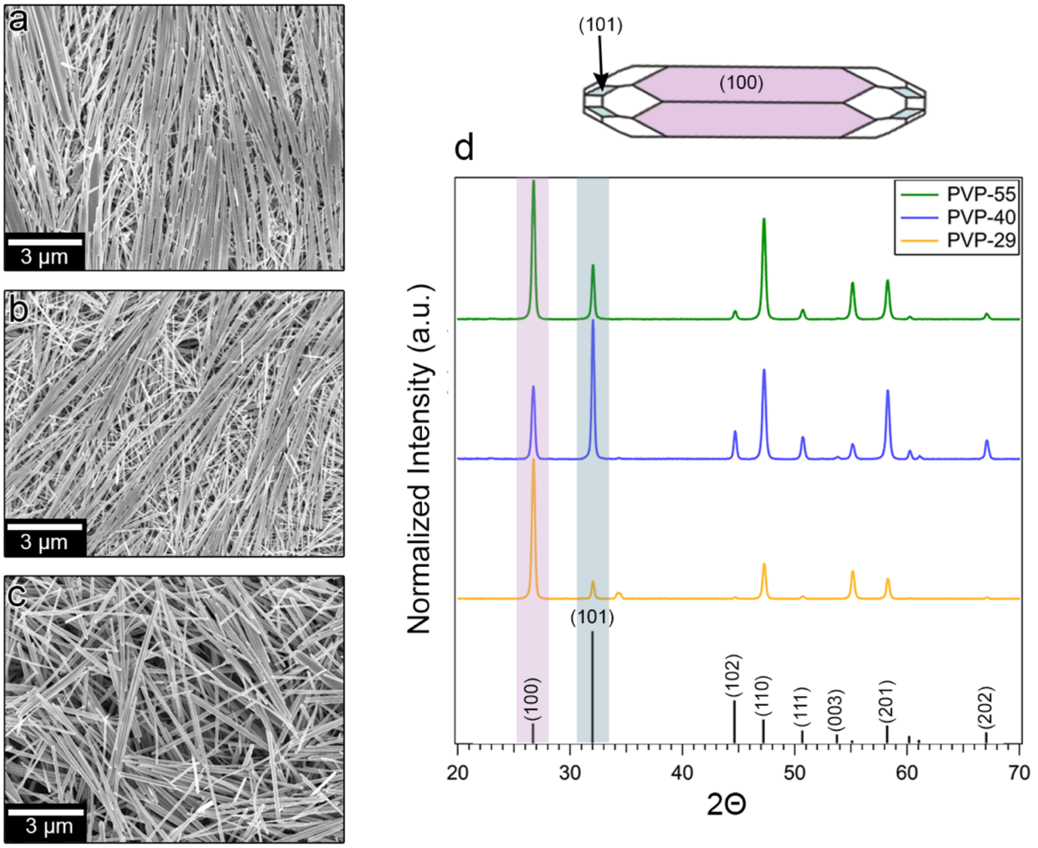

Figure 3.2- Scanning electron micrographs and Powder X-ray Diffraction (PXRD) for Te NWs synthesized with 3 different molecular weights of PVP show a clear trend of increasing *AR* distribution as a function of PVP molecular weight increase. Panel (a) corresponds to PVP-29 wires, (b) PVP-40 NWs and (c) PVP-55 NWs. Panel (d) provides clear confirmation that all the Te NW batches are of the same trigonal crystal structure belonging to space group P3121. Above panel (d) a visual representation of the Te NW facets can be found where the body facet (100) is marked in pink and the end facet (101) is highlighted in blue.

In an attempt to further elucidate the underlying factors at play, gel permeation chromatograph (GPC) was run on the PVP starting polymers in order to confirm the MW and polydispersity index (D) of the polymers. The GPC results are detailed in **Table 3.2** and demonstrate that the actual differences between the claimed molecular weights are closer than the nominal values. In particular, the GPC results indicate that the 55 kDa PVP is only slightly higher in MW than the 40 kDa. Thus, the similarities in *AR* between these two systems is not surprising.

Sahu *et al*. employed the PVP-based multi-step synthetic method and modulated reagent concentrations to synthesize two sets of NWs with different ARs, 20 and 1000, and diameter held constant at ~25 nm, resulting in TE power factors of 25 and 145 µWm^{-1}K^{-2} respectively.[50] Instead, by using different PVP MW in the synthesis, we observe that similar power factors can be attained at lower ARs. **Figure 3.3a** and **b** show the TE properties of PVP-29, PVP-40, and PVP-55 as a function of the average *AR* for each hybrid; the Seebeck coefficient does not show a strong dependence on *AR* but electrical conductivity does increase as *AR* increases. The highest *AR* is obtained in PVP-40, which shows the highest electrical conductivity, and this performance enhancement translates to a power factor of ~127 µWm^{-1}K^{-2} for a hybrid with no extrinsic doping. The benefit of achieving such high power factors in an undoped material is the possibility for future performance enhancement through utilization of well-established doping/de-doping protocols in literature.[50,54,86,112] These materials far exceed the performance of Te-PEDOT:PSS hybrids reported in literature with comparable or smaller *ARs*, and rivals the power factor reported by Sahu *et al*. for the same material at an ultra-high *AR* of ~1000.[50] A comparison of power factors and ARs (calculated from the reported NW dimensions in each paper) for the hybrid NWs presented in this work and those reported in literature are shown in **Table 3.3**.[50,52,53,86,112]

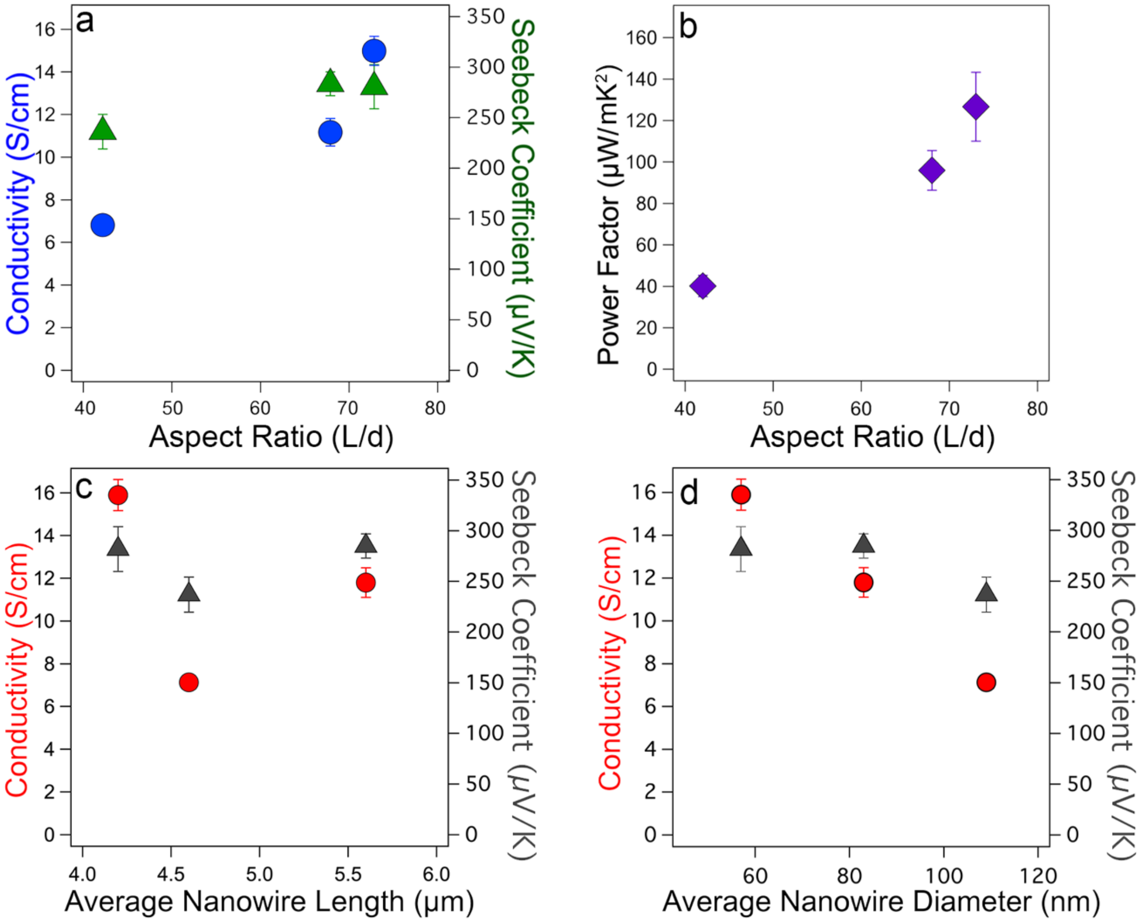

Figure 3.3- Thermoelectric performances of the as-synthesized Te-PEDOT:PSS NWs. Electrical conductivity, Seebeck coefficient and power factor are shown in graphs (a) and (b) as a function of AR. There appears to be a clear correlation between *AR* and performance where the highest performing set of wires having an *AR* of 73, demonstrate a power factor of ~130 uW/mK^2. In order to better understand the driving forces behind this trend, conductivity and Seebeck coefficient as a function of average NW length and diameter are shown in panels (c) and (d) respectively. While there is a distinct lack of trend between conductivity and NW length, a dependency can be observed as a function of NW diameter. Vertical errors bars are the standard deviations between triplicate measurements.

With this PVP MW modulating technique, the NWs produced are similar in length, which implies that NW diameter is the main driver impacting charge transport. **Figure 3.3c** and **d** show electrical conductivity (the parameter most dramatically impacted by AR) as a function of NW length and diameter, respectively. While **Figure 3.3c** does not show a distinct trend, **Figure 3.3d** shows a direct correlation between decreasing diameter and increased conductivity. **Figure 3.8** shows power factor as a function of both NW diameter and length. We observe a power factor enhancement from 40 to 127 $\mu Wm^{-1}K^{-2}$ as a result of average diameter decrease from 110 to 57 nm for PVP-29 and PVP-40, respectively. Reducing the NW diameter by 3x brings about roughly the same performance enhancement as that observed by Sahu *et al.* for a 100x increase in NW length. Thus, it appears that TE performance is significantly more sensitive to NW diameter differences than changes in NW length.

This diameter dependent conductivity result is also consistent with our recent study on single nanowires of Te-PEDOT:PSS with the same synthesis method as this work using the 40 kDa PVP.[124] It is observed that electrical conductivity monotonically increases as NW diameter decreases, while the Seebeck coefficient remains relatively constant. This enhancement is attributed to increased mobility arising from templating of PEDOT:PSS on the surface of the inorganic nanowire, as there is a decrease in surface energy for smaller wire diameters that enables the polymer chains to align or self-assemble on the Te NW surface.[124] These findings paired with the results discussed in this study suggest that nanoscale templating effects dependent on NW diameter impact overall transport far more than macroscale interfacial scattering that is dominated by NW length.

3.4 Conclusions

In conclusion, this report explored the morphological impacts of utilizing different MWs of surface ligand PVP and provided some insight on the fundamental driving forces behind the TE performances observed in the resulting hybrid systems. We demonstrate a power factor of ~130 $\mu Wm^{-1}K^{-2}$ for our entirely undoped and untreated low *AR* Te-PEDOT:PSS NWs, which rivals the high performances of the same materials with ultra-high *ARs*. This comparable performance for dramatically different *ARs* demonstrates the need to further decouple effects of NW length and diameter. This work challenges traditional design rules (*i.e.* high *ARs*) thought to be necessary for high TE performance in this hybrid system and instead posits that average NW diameter dominates charge transport within the system. This diameter dependent trend is very intriguing and deserves further investigation. However, given the inherently disordered and complex nature of the bulk mesh thin films used in this study, it is challenging to be able to definitively identify the driving forces behind the observed trends. Therefore, now that synthetic control over hybrid NW dimensions has been established, it is paramount that a carefully controlled hybrid model system is investigated. The work done in the next chapter, Chapter 4, directly addresses this and builds upon the understandings established in this chapter.

3.5 Materials and Methods

3.5.1 Nanowire Synthesis

PEDOT:PSS (Clevios PH1000) was purchased from Heraeus and underwent no further processing other than vortexing and filtration. Tellurium dioxide (99.9995%), polyvinylpyrrolidone (PVP, average molecular weights 29 kDa, 40 kDa, and 55 kDa), sodium hydroxide (NaOH, ACS reagent,

≥97.0%, pellets), ethylene glycol (EG, ReagentPlus®, ≥99%), hydrazine hydrate (HH, 78-82%, iodometric), and sodium sulfide (NaS) were purchased from Sigma Aldrich.

Te-PVP NWS - Synthesis of PVP coated Te NWs and surface ligand exchange to sulfur then PEDOT:PSS followed protocol established in existing literature barring some slight modification.[50] In this reaction EG (30 mL) is utilized as both the solvent and as the partial reducing agent. EG is placed in a round bottom flask under an inert N_2 environment, stirred with a Teflon stir bar and its temperature is monitored by thermocouple. NaOH (0.9 g) is then slowly added to the EG solution and allowed to stir until fully dissolved. Upon dissolution of NaOH in the mixture, PVP (0.3 g) is added and dissolves. The same is done for the addition of TeO_2 (0.72 g). Once all of these reagents have been added then a heating mantle is placed beneath the round bottom flask and the solution is slowly heated to 160ºC and vented while maintaining stirring and inert environment conditions. The solution initially appeared translucent but as heating continues, it transitioned to a clear yellow before becoming dark and opaque. The appearance of a dark grey/brown opaque color is indicative of the start of nucleation. When the solution temperature approaches 160ºC then HH (1.5 mL) should be rapidly injected into the mixture in order to truly induce nucleation. Once HH has been injected the reaction is left to heat and stir for one hour. The reaction is then quenched by removing the heat source and submerging the round bottom flask into a cool water bath. Once the product temperature has lowered to ~35ºC then the contents of the flask are transferred to 50 mL disposable Falcon tubes to prepare for the cleaning process. To clean the NW solution, the tubes are centrifuged for 35 minutes at 9,000 rpm then the supernatant is poured off, fresh deionized water is added, and the entire tube is vortexed. This process is repeated 5-6 times or until the supernatant appears clear then the final cleaned Te-PVP wires bound in the bottom pellet are resuspended in water.

Te-PEDOT:PSS NWs - In order to convert the Te-PVP NWs to the more useful form of Te-PEDOT:PSS NWs, a multistep ligand exchange process was employed. The cleaned Te-PVP NWs were placed in a closed jar with excess water and NaS (~1 g). The mixture was left to stir overnight. The next morning the NW solution is cleaned three times following the same centrifugation protocol detailed above. The cleaned NWs are then suspended in excess water and PEDOT:PSS (~10 mL) is added to the solution. The mixture is again stirred and left overnight. After stirring over night, The PEDOT:PSS-NW solution is cleaned again three times via centrifugation to yield clean Te-PEDOT:PSS NWs.

Thin Film Preparation - Thin film samples were prepared by employing a drop cast technique onto glass substrates (9.5 mm x 9.5 mm, 1 mm thick – Thin Film Devices). The substrates were prepared for deposition by undergoing UV-ozone treatment for at least 10 minutes prior to casting. Once clean, the substrates were placed upon a hot plate and heated at 90 °C, and then 75 μL of the hybrid nanowire composite solution was deposited then left to dry for 10-20 minutes until solvent was entirely gone. 100 nm gold contacts were thermally evaporated onto each of the four corners of the thin films using a shadow mask to aid in electrical contact during thermoelectric measurements.

3.5.2 Electrical and Thermoelectric Measurements

Keithley 2400 Source meters in 4-probe van-der-Pauw configuration were used to measure the sheet resistance of each film. The thickness of each film was measured by measuring the step height of a scratched film using a Veeco Dektak 150 profilometer. Electrical conductivity values were then calculated using the sheet resistance and the thickness measurements. The Seebeck coefficient was determined using a homemade probe setup consisting of two Peltier devices (ferrotect) placed ~4 mm apart. A single current was passed through each of the Peltier devices in opposite directions, resulting in one device heating up and the other cooling in roughly the same amount with respect to room temperature. A thin film sample is then suspended across the gap between the two Peltier devices (thermal paste was utilized to ensure good thermal contact was being made – Wakefield Thermal S3 Solutions) in order to enable a thermal gradient to arise. The open circuit voltage was then measured across the sample in the same direction as the temperature gradient using an Agilent 34401 multimeter. The magnitude of the temperature gradient across the sample was monitored by the placement of two T-type thermocouples mounted in micromanipulators. The magnitude of the temperature gradient is directly related to the magnitude of current driven through the Peltier devices, thus five different temperature gradients were established (200 sec equilibration time allowance between each temperature gradient). 10 voltage measurements were taken and averaged at each chosen gradient point. All samples exhibited linear variation of open circuit voltage with temperature gradient; this trend was then used to extract Seebeck coefficient values. Data for both electrical conductivity and Seebeck coefficient were acquired using homemade Labview programs. For each measurement, at least three different samples were measured and averaged, with error bars representing standard error. Ohmic contacts were confirmed before measurements.

3.5.3 Characterization

Scanning electron microscopy (SEM), transmission electron microscopy (TEM), X-Ray diffraction (XRD), and thermogravimetric analysis (TGA) were used to characterize the size, shape, structure and composition of the composite system.

Scanning Electron Microscopy - SEM images were captured on a Zeiss Gemini Ultra-55 Analytical Field Emission Scanning Electron Microscope using beam energy of 5 kV.

Transmission Electron Microscopy – A FEI monochromated F20 UT Tecnai was operated at an accelerating voltage of 200 kV. Real space images were taken with a spot size of 3 and an exposure of 0.7 seconds. TEM samples were prepared by placing a TEM grid (400-mesh Cu on holey carbon – Ted Pella 01824) on a filter paper taped flat to a hot plate at 90°C. A single drop of dilute hybrid material solution was deposited onto the grid and then water was slowly forced off for 5 min.

X-Ray Diffraction - A Bruker AXS D8 Discover GADDS XRD micro-diffractometer was used to capture wide-angle spectra using a 0.154 nm wavelength Cu-Kα source.

Thermogravimetric Analysis - To quantify the organic-inorganic weight percent ratio of each sample, a TA Instruments Q5000IR TGA was used. 7-10 mg of each sample was ramped to 600°C at a scan rate of 10°C/min and then an isothermal hold of 60 minutes in order to guarantee complete organic phase decomposition. The total mass percent change after this process was assumed to be the organic component of the hybrid composite system where as the remaining weight percent was assumed to be the inorganic component.

Gel Permeation Chromatography - Gel permeation chromatography (GPC) was conducted on an Agilent 1260 Infinity Series fitted with Waters Styragel HR3 and HR4 columns with 0.05 M LiBr in N-methyl-2-pyrrolidone (NMP) as the mobile phase. The GPC was calibrated using poly(ethylene oxide) standards. The polymer samples were mixed with NMP and stirred at 60 °C until clear solutions were formed and passed through a 2 μm filter before analysis.

3.6 Acknowledgements

This work was performed at the Molecular Foundry, Lawrence Berkeley National Laboratory, and was supported by the Department of Energy, Office of Science, Office of Basic Energy Sciences, Scientific User Facilities Division of the U.S. Department of Energy under Contract No. DE-AC02-05CH11231. M.P.G. gratefully acknowledges the National Science Foundation for fellowship support under the National Science Foundation Graduate Research Fellowship Program. A.K.M acknowledges funding support from the ITRI-Rosenfeld Fellowship from the Energy Technologies Area at Lawrence Berkeley National Laboratory.

3.7 Supporting Information

3.7.1 Thermogravimetric Analysis

The ligand exchange process utilized in this study does not always result in samples with exactly the same ratios of inorganic to organic constituents. As a result, each system is further optimized by adding varying amounts of PEDOT:PSS to the hybrid nanowire solution in order to obtain comparable organic-inorganic weight percent ratios. This was quantified with thermogravimetric analysis (TGA), which confirms that all samples had an organic weight percent of 50-70% (representative curve plotted in **Figure 3.4**).

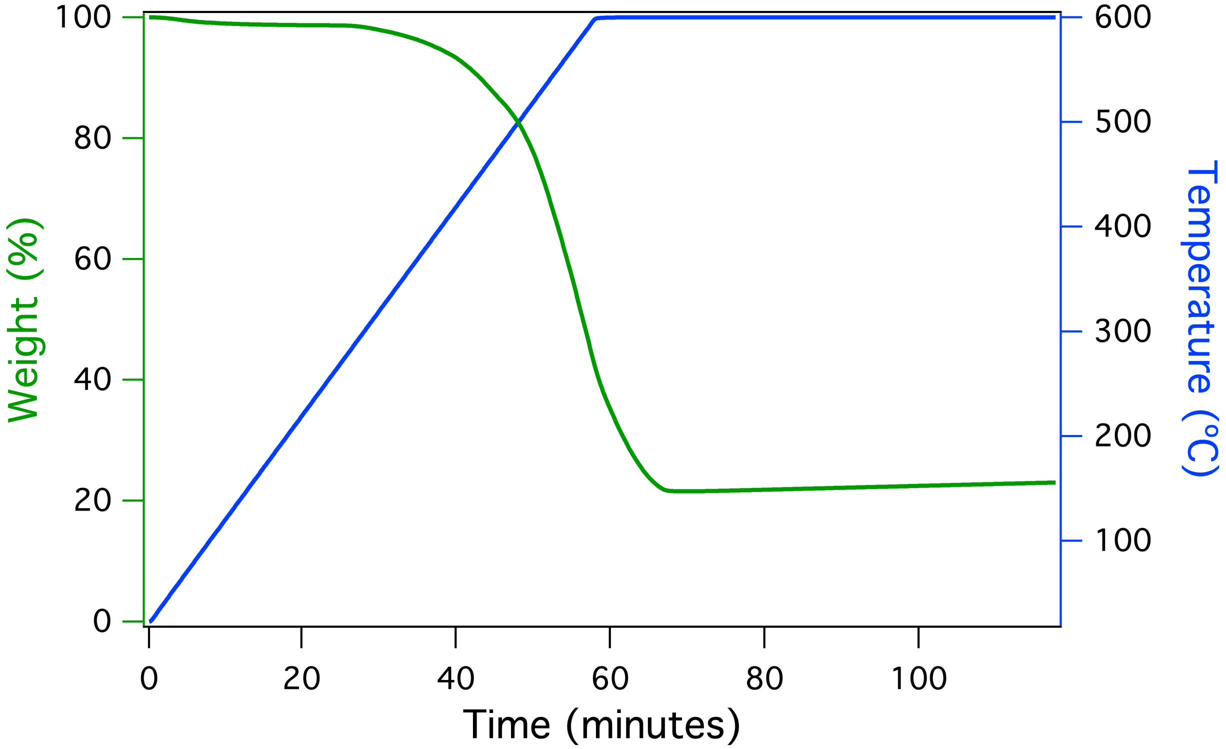

Figure 3.4 Representative TGA plot showing the decomposition of the organic component beginning at 200°C during a heat ramp to 600°C. Once the weight percent curve levels off it is indicative of the entirety of the organic phase having been removed to leave only the inorganic component behind.

3.7.2 Nanowire Dimensional Analysis

While PVP-40 appears to produce the highest *AR* wires (AR- 73), a clear correlation can be found between *AR* size distribution and PVP MW. As PVP MW increases, the produced wires trend towards larger *ARs*. While PVP-55 has a slightly lower average *AR* than PVP-40, inspection of **Figure 3.5 a, b,** and **c** panel insets display cumulative distribution functions which effectively demonstrate what percentage of the entire population lies below a given *AR* value. It's clear that for PVP-55 the statistically relevant populace does appear at *AR* values similar to PVP-40 but overall the population is far broader and leans towards larger *ARs*. To further corroborate this point, inspection of the standard deviation for diameter and length in **Table 3.1** further indicate that PVP-55 produces wires of a wider size distribution. All diameter and length statistics were determined via hand counting n>50 wires from SEM images using ImageJ software to determine dimensions.

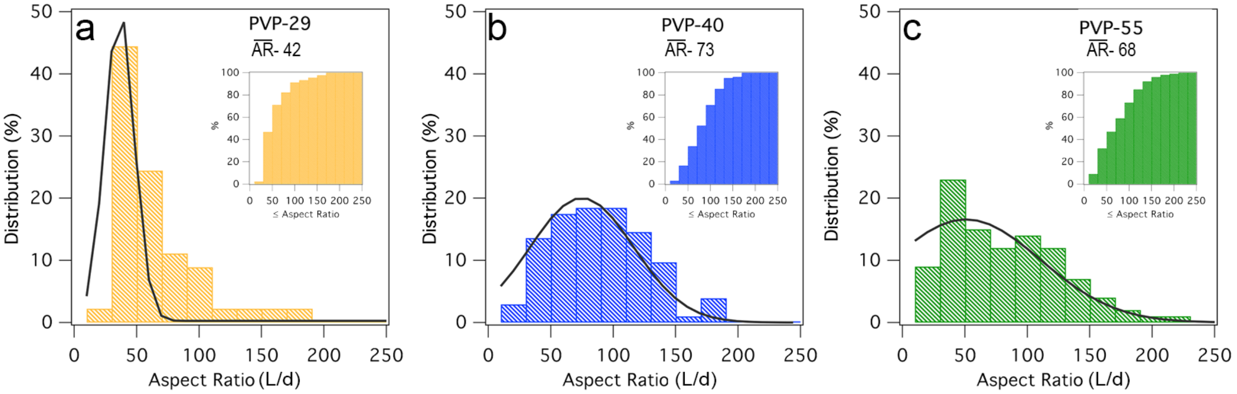

Figure 3.5 *AR* histograms for Te NWs synthesized with 3 different molecular weights of PVP. Panel (a) corresponds to PVP-29 wires, (b) PVP-40 NWs and (c) PVP-55 NWs. Insets shown within panels (a), (b), and (c) are cumulative distribution functions representative of the increase in size distribution spread as larger molecular weight of PVP are used to synthesize wires.

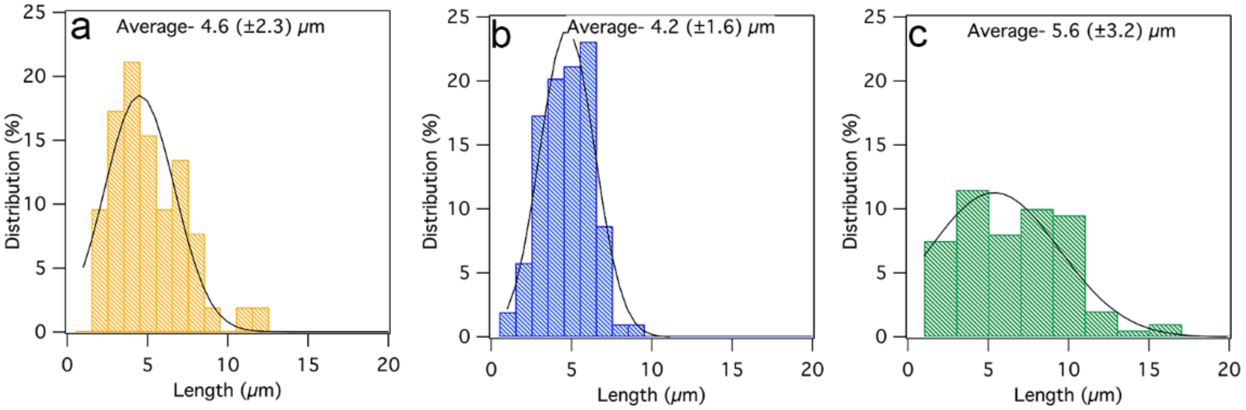

Figure 3.6 Nanowire length size distribution histograms depicting the general closeness in lengths apparent for all three systems at play.

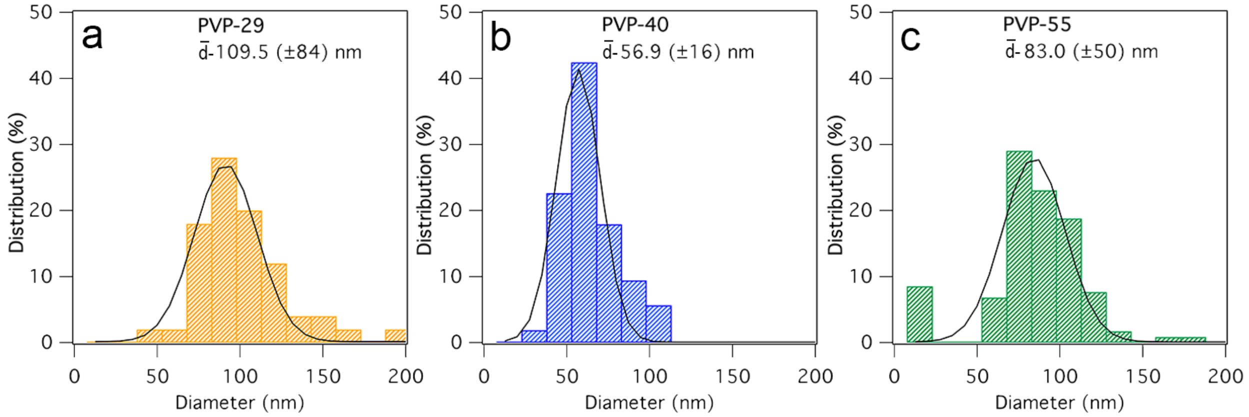

Figure 3.7 Diameter histograms for Te NWs synthesized with 3 different molecular weights of PVP. To further demonstrate differences in NW diameter, panels (a), (b), and (c) are shown for PVP-29, PVP-40 and PVP-55, respectively.

3.7.3 X-ray Diffraction Analysis

Particular care was taken to ensure that all Te NW structures were composed of the same phase. High peak intensities can be observed for the (100), (110), and (200) peaks corresponding to the {hk0} planes. Lower peak intensities can be observed for the (001), (102), and (200) peaks corresponding to the {hkl}, l≠0 planes. Similar differences in intensities have been reported by Li *et al.* where they correlated the phenomenon to preferential growth in the [001] axial direction.[125] This conclusion is consistent with our experimental results given the long length of these NWs. Additionally, peak intensity differences are a result inhomogeneous NW orientation between measured films.

3.7.4 Carrier Dynamics

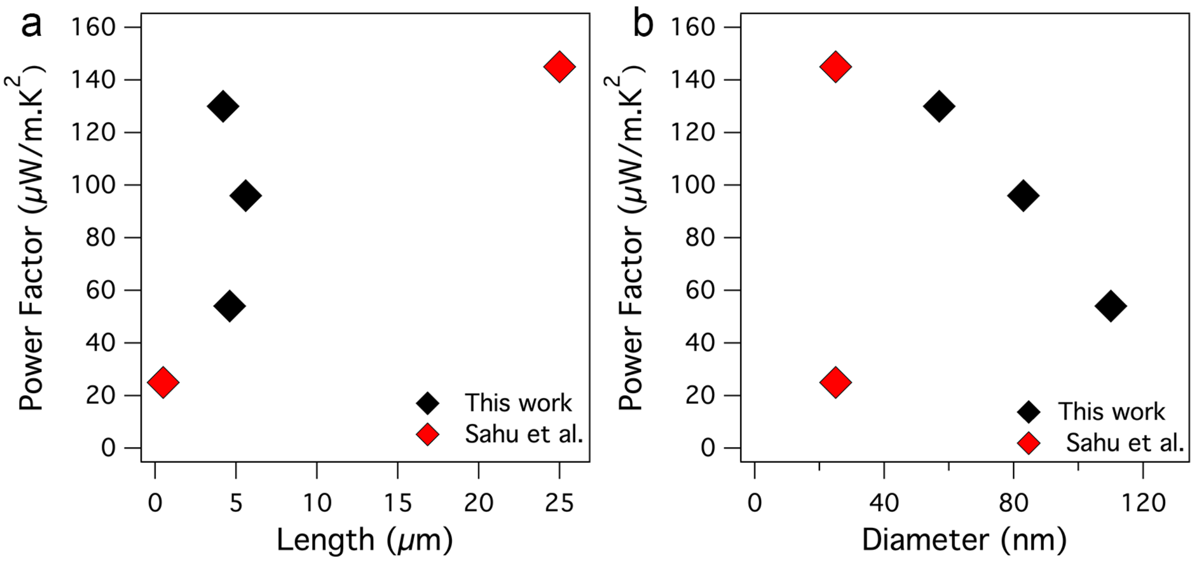

Figure 3.8 Power factor versus average nanowire length and diameter. This plot demonstrates the distinct sensitivity to diameter that these hybrid Te-PEDOT:PSS nanowire systems demonstrate compared to the impact of tuning nanowire length.

Table 3.2 Gel permeation chromatography (GPC) performed on neat starting PVP polymers as acquired from Sigma Aldrich. We report the number averaged and weight averaged molecular weight (M_n and M_w, respectively) and the polydispersity ($D=M_w/M_n$) for the three PVP samples. The values reported in the table were obtained using an instrument calibration performed with poly(ethylene oxide) standards. To obtain accurate Mn and Mw values, the instrument should be calibrated with PVP standards, but these were not readily available. Therefore, the absolute value of M_n and M_w values are not expected to be consistent with the nominal values provided by Sigma Aldrich, but comparisons between the three samples is valid.

GPC Statistics	**29 kDa**	**40 kDa**	**55 kDa**
Mn	6390.7	8862	8993.2
Mw	25365	31308	35405
D	3.9691	3.5329	3.9368

Table 3.3 Comparison of power factors and aspect ratios (calculated from the reported dimensions in each paper) for the composite nanowires presented in this paper and analogous undoped systems from the literature.

Authors	**Aspect Ratio**	**Power Factor** (μW/m.K^2)	**DOI**
Yee *et al.*	<10	15	10.1039/C3CP44558E
Sahu *et al.*	20	25	10.1039/C6TA09781B
Coates *et al.*	21	35	10.1002/adma.201203915
See *et al.*	16-24	71	10.1021/nl102880k
Bae *et al.*	26-40	68	10.1038/srep18805
This work	**42**	**54**	
This work	**68**	**96**	
This work	**73**	**127**	
Sahu *et al.*	1000	145	10.1039/C6TA09781B

Chapter 4. Identifying the decoupling of charge and heat transport by enacting a hybrid single nanowire investigation

Adapted from "Decoupling electron and phonon transport in single nanowire hybrid materials for high performance thermoelectrics," L. Yang,† M.P. Gordon,† A.K. Menon, A. Bruefach, K. Haas, M.C. Scott, R.S. Prasher, J.J. Urban, *Science Advances,* 2021, 7, 20. (DOI:10.1126/sciadv.abe6000) with permission of the authors. *Reprinted with permission of AAAS.* † Denotes equal contribution.

4.1 Abstract

Organic-inorganic hybrids have recently emerged as a class of high performing thermoelectric materials that are lightweight and mechanically flexible. However, the fundamental electrical and thermal transport in these materials has remained elusive due to the heterogeneity of bulk, polycrystalline, thin films reported thus far. Herein we systematically investigate a model hybrid comprising a single core/shell nanowire of Te-PEDOT:PSS. We show that as the nanowire diameter is reduced, the electrical conductivity increases and the thermal conductivity decreases, while the Seebeck coefficient remains nearly constant - this collectively results in a figure of merit, *ZT*, of 0.54 at 400 K. The origin of the decoupling of charge and heat transport lies in the fact that electrical transport occurs through the organic shell, while thermal transport is driven by the inorganic core. This study establishes design principles for high performing thermoelectrics that leverage the unique interactions occurring at the interfaces of hybrid nanowires.

4.2 Introduction

Organic semiconductors and organic-inorganic hybrid materials have garnered significant interest for thermoelectric applications owing to their unique advantages over inorganic materials. For example, organic semiconductors can realize flexible and lightweight energy generation or heating-cooling devices with conformal geometries, and their solution processability enables the use of inexpensive and scalable manufacturing processes [23,36,37,105]. This has led to a surge of interest in various applications, such as implantable medical devices [126], wearables for personal electronics [35], and Internet of Things (IOT) [56,127]. For a given temperature *T*, the efficiency of a thermoelectric material is characterized using a dimensionless figure of merit, $ZT = S^2\sigma T/\kappa$, which encompasses three material properties: Seebeck coefficient *S*, electrical conductivity σ, and thermal conductivity κ. Unfortunately, the well-known interdependence between σ, κ, and *S* in a single phase material often complicates efforts to develop effective strategies to achieve a high *ZT* [23,128].

Previous efforts to enhance *ZT* can be broadly divided into two groups: (*i*) enhancing power factor through electronic doping [128], quantum confinement effects [129], etc., and (*ii*) decoupling interdependence among electrical conductivity, Seebeck coefficient, and thermal conductivity through nanostructuring [130], hierarchical architectures [131], etc. However, maximizing *ZT* using either approach results in a compromise between σ, κ, and *S* in a single phase material. For instance, among conducting polymers, poly(3,4-ethylenedioxythiophene):poly(styrenesulfonic acid) (PEDOT:PSS) is appealing due to its high electrical conductivity upon secondary doping, but a low Seebeck coefficient largely limits its thermoelectric power factor [23,37]. To circumvent this challenge, efforts have been made to integrate the high σ of PEDOT:PSS with Tellurium (Te) nanostructures to form hybrid core-shell systems (Te-PEDOT:PSS) that demonstrate high power factors ($PF = S^2\sigma$), while maintaining solution processability [52,53,112]. This hybrid material system, combining organic and inorganic phases, yields thermoelectric PF exceeding that of either constituent material owing to nonlinear interactions that occur at the hard-soft interface [52,53,112], which results in a ZT value of ~ 0.1 at 300 K [52], and a higher ZT of 0.39 is achieved after chemical treatment with sulfuric acid [132]. One example of such an interaction is the better ordering of PEDOT domains upon introduction of Te nanowires, which has been theoretically shown to improve the electrical conduction in the organic phase [51,133]. Given the inherently low thermal conductivity of the polymer shell and the ultra-thin shell thickness (1-2 nm), it is reasonable to assume that the inorganic core would dominate thermal transport. Taken together, these effects in a hybrid material could offer an unprecedented opportunity to decouple thermal and electrical transport to engineer a high ZT. However, there has been no experimental demonstration of this approach, and the size (*i.e.,* diameter) dependence of electronic and thermal transport for the hybrid nanowires also remains unexplored.

Over the past decade, Te-PEDOT:PSS hybrids have been fabricated as bulk films using various fabrication methods, and the high thermoelectric performance has been attributed to the following possible mechanisms: *(i)* energy filtering at the organic-inorganic interface due to work function offset between the two constituents; *(ii)* interfacial charge transfer induced doping/de-doping, and *(iii)* locally enhanced transport at the Te and PEDOT:PSS interface due to structural reordering effects, *i.e.,* templating [52–54,112,132,134,135]. However, owing to the multiphase nature of these materials, the validity and contribution of these different mechanisms remains an issue of debate. This is further complicated by the fact that all thermoelectric transport studies on the Te-PEDOT:PSS hybrid system thus far have centered on bulk films (nanowire meshes fabricated into thin films, each containing billions of nanowires) [52–54,112,132,134,135]. In these films, the measured thermoelectric properties are averaged over wires of varying dimensions and orientations, and interfacial scattering between nanowires makes it challenging to elucidate the inherent charge transport mechanism.

Additionally, thermal transport in these hybrid systems has not been studied even though these multiphase materials could exhibit interesting phonon scattering mechanisms. For instance, molecular dynamics (MD) simulations of Si/amorphous SiO_2 (a-SiO_2), another core/shell nanowire containing a hard-soft interface, have shown that the presence of a-SiO_2 on the Si nanowire surface strongly scatters phonons propagating into the amorphous shell, forming quasi-stationary modes with mean free paths (MFPs) on the order of interatomic distances [136]. In a similar manner, the semi-crystalline PEDOT:PSS shell of the hybrid system is also acoustically soft and slow [137], in which case phonons are likely to form non-propagating modes within it, thereby forcing thermal transport within the inorganic Te core, and a size (*i.e.,* diameter) dependent thermal conductivity is expected due to stronger phonon boundary scattering. Furthermore, thermal conductivity measurements for hybrid thin films reported thus far have been measured in the through-plane direction, while charge transport and electronic properties are measured in the in-plane direction [37]. This has led to inconsistencies in literature, especially given the inherently anisotropic nature of a bulk mesh film. As such, to glean insight into the underlying charge carrier and phonon transport mechanisms, a model material system comprising free-standing single hybrid nanowires is required with electronic and thermal properties measured along the same axial direction. Performing a systematic and well-controlled study on such a model system will enable the establishment of structure-property relationships for hybrid materials, which is of paramount importance to enhance thermoelectric performance.

In this work, for the first time, we report the thermoelectric properties of individual free-standing Te-PEDOT:PSS core/shell nanowires. By varying the diameter of the inorganic core while maintaining a fixed organic shell thickness, we directly demonstrate that the PEDOT:PSS shell dominates charge carrier (hole) transport. Interestingly, an inverse relationship between the electrical and thermal conductivity with respect to nanowire diameter confirms the ability to decouple these properties, with the inorganic core being the dominant channel for phonon transport. Our results demonstrate the unique advantage of using hybrid materials for thermoelectric applications and provides critical insight into the mechanisms at play, as described in the following sections.

4.3 Results and Discussion

4.3.1 Thermoelectric properties of single hybrid nanowires

The nanowires utilized in this study consist of a soft polymer shell (PEDOT:PSS) and a hard inorganic core (Te) that appears to be single crystal belonging to space group $P3_121$ as shown in **Figure 4.1a** and **4.1c**. The thermoelectric properties of individual Te-PEDOT:PSS nanowires were measured using a custom-fabricated suspended microheater device shown in **Figure 4.1b** [138–140], which enables simultaneous measurement of σ, S, and κ on the same nanowire sample (see Methods) [141,142]. Importantly, this sample geometry ensures that both thermal and electrical properties are measured along the same axial direction, which is crucial given the anisotropic nature of these hybrids and addresses a major drawback with previous thin film measurements.

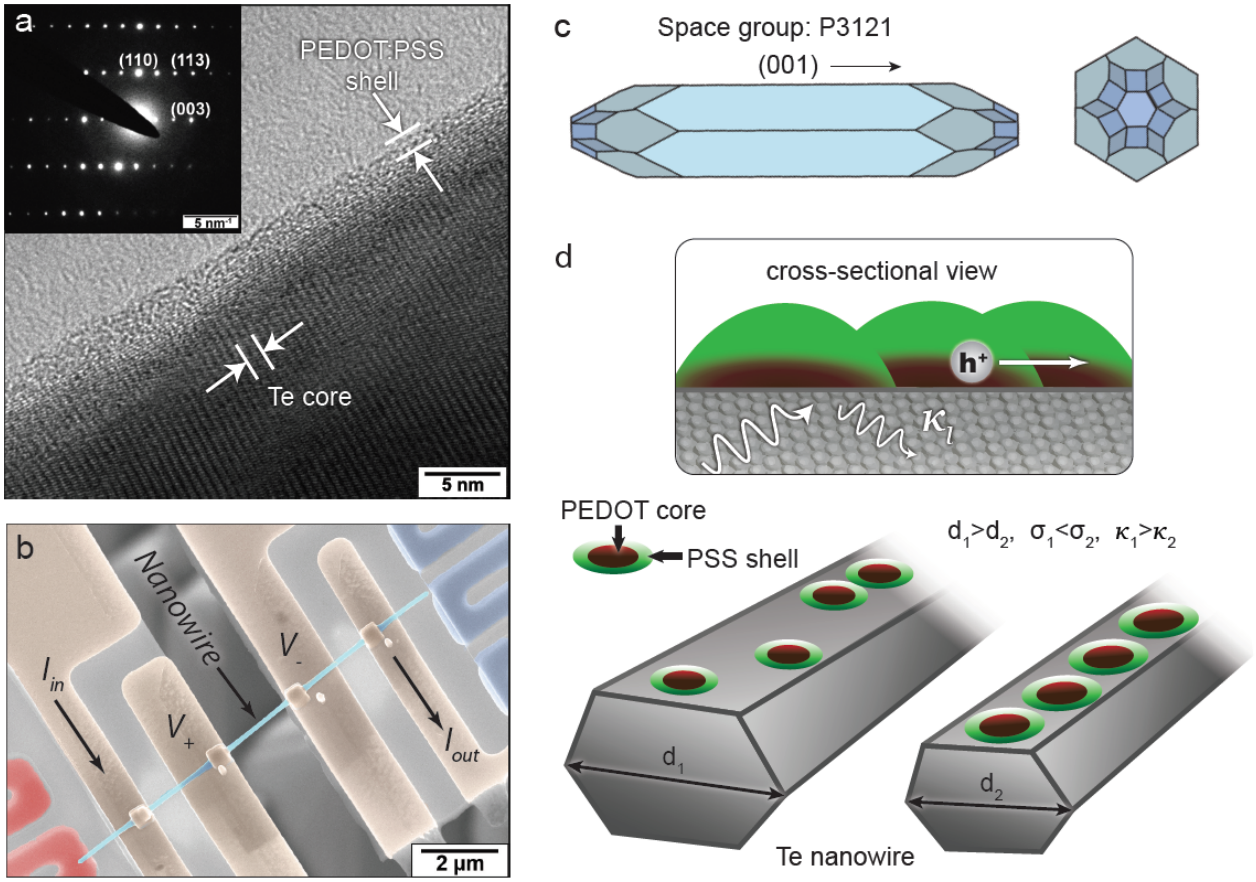

Figure 4.1- Material structure and thermoelectric properties measurement scheme. (a) A HRTEM micrograph distinguishing between the PEDOT:PSS shell and the inorganic Te core. The inset is an SAED pattern confirming the single crystal nature of the Te nanowire and its crystallographic structure and orientation. (b) Scanning electron micrograph depicting the suspended pad measurement platform utilized to probe the thermoelectric properties of the hybrid nanowire, where the artificial coloration is used to aid in distinguishing between components. (c) Visualization of the crystallographic space group that the Te core forms with the different facets shown and the (001) direction along the nanowire axis of growth. (d) The top portion of the cartoon schematics depicting thermal transport occurring through the inorganic core while electronic carrier transport occurring through the organic shell, and the bottom portion of the panel illustrating the proposed hypothesis of better organic templating on narrower nanowire diameters being the cause for the observed enhanced charge mobility.

The room temperature electronic properties of Te-PEDOT:PSS core/shell nanowires with six different diameters are shown in **Figure 4.2**. The smallest sample measured has a diameter ~ 40 nm due to challenges associated with dry transferring thinner nanowires. Interestingly, σ monotonically increases from 10.8 to 43.1 S/cm as the nanowire diameter (D) is reduced from 186 to 42 nm, while S remains nearly constant at ~302 μV/K across all samples, collectively resulting in a power factor increase from 90 to 415 μW/m-K^2. Here, the electrical conductivity is calculated based on $\sigma = L/(RA)$, where L is the nanowire suspended length, R is the measured electrical resistance, and A is the total cross-sectional area of the hybrid nanowire. Thus, by reducing the wire diameter in this hybrid system, we are able to achieve a monotonic increase in σ while S remains largely unchanged. This trend contrasts with single phase materials, in which a fundamental inverse relationship between S and σ upon doping limits enhancements to the power factor. Note that for all core/shell nanowires studied in this work, the PEDOT:PSS polymer shell thickness is 1.45 ± 0.34 nm, while the Te core diameter is varied (**Figure 4.6**), and the suspended length of all wires is maintained between 2.8 - 3.7 µm.

To understand the underlying mechanisms for the diameter dependence of σ which results in a power factor enhancement, it is critical to consider what material phase (*i.e.,* inorganic or organic) dominates electrical transport in the hybrid. If the inorganic core dominates transport, reducing the diameter would not impact σ for wires with diameters larger than the electron mean free path; when the diameter is smaller than the electron mean free path, σ would be lower due to electron-boundary scattering effects, unless the material is a topological insulator [143]. However, theoretical predictions show that Te becomes a topological insulator only with the application of shear strain [144], which is absent in our experiments. A second possible mechanism is energy filtering at the hard-soft interface due to the work function offset between Te and PEDOT:PSS, which would cause the scattering of low energy carriers and results in enhancements in S with only a modest decrease in σ [145]. Given that all the nanowires studied here are composed of the same hard and soft material (*i.e.* same work function offset across the different samples), they would all be subject to the same effect energy filtering effect, if at all. Thus, the phenomenon of energy filtering is irrelevant to our study. Yet another possibility for the diameter dependence is that as the nanowire diameter decreases, the volume fraction of PEDOT:PSS in the hybrid increases, which in turn leads to a higher σ. However, our mean field theory calculation using the parallel resistance model rules out this effect, and the observed thermoelectric property enhancement cannot be described by a simple composite (details can be found in Section 4.7.6). Thus, we hypothesize that electronic transport is occurring predominantly through the organic shell of the hybrid nanowire system.

To validate this hypothesis, we measured the thermoelectric properties of another set of nanowires with a different organic component, namely polyvinylpyrrolidone (PVP) coated Te nanowires. Unlike PEDOT, PVP is an electrical insulator, but has a similar shell thickness ~1.14 ± 0.36 nm while the Te core diameter is varied (**Figure 4.6**). As shown in **Figure 4.2**, the measured σ of Te-PVP core/shell nanowires is only 3.8 S/cm, and it does not exhibit a diameter dependence. If the Te core is responsible for charge transport in the hybrid system, Te-PVP would also show a size dependent σ similar to Te-PEDOT:PSS wires. Note that transport through the organic shell has been previously proposed by Coates *et al.* [53] and Kumar *et al.* [51] based on bulk films, but our work provides the first experimental evidence that conclusively proves that charge transport occurs predominantly through the PEDOT:PSS shell.

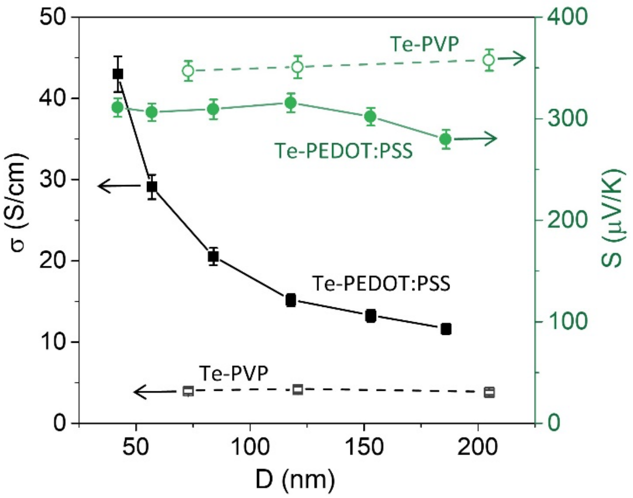

Figure 4.2- Room temperature electrical transport properties. Measured room temperature electrical conductivity and Seebeck coefficient are plotted as a function of wire diameter for different Te-PEDOT:PSS core/shell nanowires. The measured results of Te-PVP core/shell nanowires, represented by the hollow symbols, are also plotted for comparison. Note that PVP is an electrical insulator, and similar to the Te-PEDOT:PSS wires, the PVP layer thickness is kept ~1.14 ± 0.36 nm in Te-PVP nanowires while only the Te core diameter is varied. Here, the measurement uncertainties of *σ* is mainly from the uncertainties in nanowire length and diameter measurements, and uncertainties of *S* is mainly from the uncertainties in linear least square fitting.

With electronic transport occurring predominantly through the organic component, there are two possible mechanisms to explain the diameter dependence in these hybrids: interfacial charge transfer (doping/de-doping) and physical templating (structural reordering) at the interface. Interfacial charge transfer, also known as the de-doping effect, occurs at the organic-inorganic interface and results in an increase in the Seebeck coefficient of hybrid thin films compared to neat PEDOT:PSS films [37,51]. In this case, the discrete molecular orbitals of the organic phase directly interact with continuum band states of the inorganic phase, resulting in interphase hole transfer from the organic PEDOT chain to the inorganic surface [51]. This mechanism in turn would lead to an enhancement in *S* and a decrease in *σ*, which is inconsistent with our experimental results and thus fails to effectively capture the impact of nanowire diameter.

The other mechanism is physical templating of the organic phase on the inorganic surface. Due to the interaction between the organic shell and inorganic nanowire, theoretical work has shown that the packing of the PEDOT molecule is altered, resulting in a reorganization of polymer chains on the inorganic core that leads to larger crystalline PEDOT domains [51]. It is well-established that such changes in crystallinity and structural ordering of polymeric domains are correlated to carrier mobility, thus contributing to a larger electrical conductivity in PEDOT:PSS [23]. As such, we posit that this templating effect at the organic/inorganic interface is responsible for the observed performance enhancement and diameter dependence in Te-PEDOT:PSS single nanowires.

4.3.2 Charge transport in hybrid nanowires

Given that charge transport is dominated by the organic shell, we use the Kang-Snyder charge transport model to validate our hypothesis that templating at the hard-soft interface leads to electrical conductivity enhancements with shrinking nanowire diameter, by separating contributions to transport that arise from mobility improvement and energy alignment [146]. This model was initially developed for conducting polymers, and in contrast to various hopping or mobility edge models that are restricted to certain property regimes, the generalized Kang-Snyder model describes both the temperature and energy dependence of many polymers over eight orders of magnitude in electrical conductivity [146].The electrical conductivity σ can be characterized by the transport function $\sigma_E(E, T)$ as:

$$\sigma = \int \sigma_E(E,T)\left(-\frac{\partial f}{\partial E}\right)dE\,, \tag{4.1}$$

where f is Fermi–Dirac distribution function, and $\sigma_E(E, T)$ is the energy dependent conductivity. The Seebeck coefficient can be described by the transport function $\sigma_E(E, T)$:

$$S = \frac{1}{\sigma}\left(\frac{k_B}{e}\right)\int\left(\frac{E-E_F}{k_BT}\right)\sigma_E(E,T)\left(-\frac{\partial f}{\partial E}\right)dE\,, \tag{4.2}$$

where E_F is Fermi level, and k_B is Boltzmann constant (more details in Methods). This model independently treats energy-dependent scattering (s), doping (reduced chemical potential η), and energy-independent transport ($\sigma_{E0}(T)$, which represents an effective carrier mobility).

A critical aspect in this model is the energy-dependent scattering parameter s, which distinguishes most conducting polymers ($s = 3$) from PEDOT-based polymers ($s = 1$) [51,146]. Different s values are attributed to different charge transport mechanisms, and it has been shown that materials with $s = 1$ (analogous to acoustic phonon scattering in inorganic materials) generally exhibit a higher mobility than those with $s = 3$ (analogous to ionized impurity scattering in inorganic materials) [146,147]. The applicability of this model to hybrid systems was previously demonstrated in hybrid thin films of Te(Cu$_x$)-PEDOT:PSS [51]. In that work, Kumar *et al.* assumed $s = 1$ and showed a good fit to their measured σ-S curve at varying amounts of Cu loading [51]. Rather than assuming $s = 1$ is the appropriate transport parameter for hybrid systems, our single nanowire model system provides direct experimental validation for this - by comparing Te-PEDOT:PSS with Te-PVP wires (**Figure 4.2**), we confirm that the PEDOT:PSS shell dominates charge transport and validate the use of the $s = 1$ parameter to model transport in hybrid Te-PEDOT:PSS nanowires.

For a given scattering parameter s, the reduced chemical potential $\eta(T)$ is obtained from the measured Seebeck coefficient $S(T)$, and then the transport coefficient $\sigma_{E0}(T)$ is extracted from the measured electrical conductivity $\sigma(T)$ (see Methods). The temperature-dependent S and σ of these single nanowires, measured using the same suspended microheater experimental setup described earlier, are shown as in **Figure 4.3a**-**b**, respectively. The extracted $\eta(T)$ and $\sigma_{E0}(T)$ for wires with different diameters are shown in **Figure 4.3c**-**d**, and **Table 4.1** shows the room temperature results. It can be seen that σ_{E0}, which functions as an effective mobility and provides insight on the morphology of the polymer shell, increases monotonically as the wire diameter is reduced, reaching 213.5 S/cm for the 42 nm diameter nanowire. The increasing trend of σ_{E0} suggests enhanced ordering of PEDOT moieties on the inorganic surfaces as the wire diameter reduces. On the other hand, η decreases slightly from -1.09 to -1.56 as the diameter is reduced from 186 to 118 nm, and nearly saturates with further reduction in diameter. The change in $\eta(T)$ is much smaller than that in $\sigma_{E0}(T)$, suggesting that de-doping effects that are captured in the reduced chemical potential are not significant in explaining the diameter dependence of these hybrid nanowires. This is as expected since de-doping at the interface results in trends that are opposite to what we measure experimentally for these hybrid nanowires. To further investigate the role of morphology in the observed performance enhancements, we calculate the hopping energy W_γ, which represents the energy barrier for transport between ordered regions, from $\sigma_{E0}(T)$:

$$\sigma_{E0} \sim \exp\left[-\left(\frac{W_\gamma}{k_B T}\right)^\gamma\right], \tag{4.3}$$

Here, $\gamma = ½$ is chosen as it is widely used for polymers, including PEDOT:PSS [146]. As shown in Table 1, W_γ decreases from 2.13 eV to 0.68 eV as the wire diameter is reduced from 186 nm to 42 nm. A lower W_γ value is expected for polymer films with improved long-range morphological order [146], and this confirms that nanowire diameter reduction results in an enhancement in the templating effect of the organic shell on the inorganic core that increases charge carrier mobility, thus leading to a boost in electrical conductivity.

Although the impact of morphology on σ or W_γ is relatively straightforward to understand, its impact on S or η is less clear. It has been shown that higher degrees of PEDOT crystallinity can increase the number of available states around the Fermi level [148], which would result in an increase in the Seebeck coefficient. However, as shown by Patel *et al.*, the Seebeck coefficient is less sensitive to morphological order as compared to electrical conductivity [149], and this could possibly explain the roughly constant value in the measured S (and is reflected in the small change of $\eta(T)$ in **Table 4.1**). Notably, we posit that the high Seebeck coefficient of the PEDOT shell is due to interphase hole transfer from the organic PEDOT chain to the inorganic Te surface, *i.e.*, de-doping effects occurring at the interface, as predicted by previous theoretical simulations [51]. This interfacial charge transfer or de-doping leads to a lower charge carrier concentration of the PEDOT phase and results in a high Seebeck coefficient. In fact, similar Seebeck coefficients have also been experimentally measured in PEDOT by reducing the charge carrier concentration [150–152]. As has been shown in organic materials, Seebeck coefficient is dominated by carrier concentration (*i.e.,* de-doping effects at the hard-soft interface) and is much less sensitive to charge carrier mobility (*i.e.,* morphological effects such as templating) [149]. Since the increase in electrical conductivity with reduced nanowire diameter is caused by mobility enhancements, it is expected that the Seebeck coefficient remains relatively unchanged for nanowires of varying diameter measured in this work.

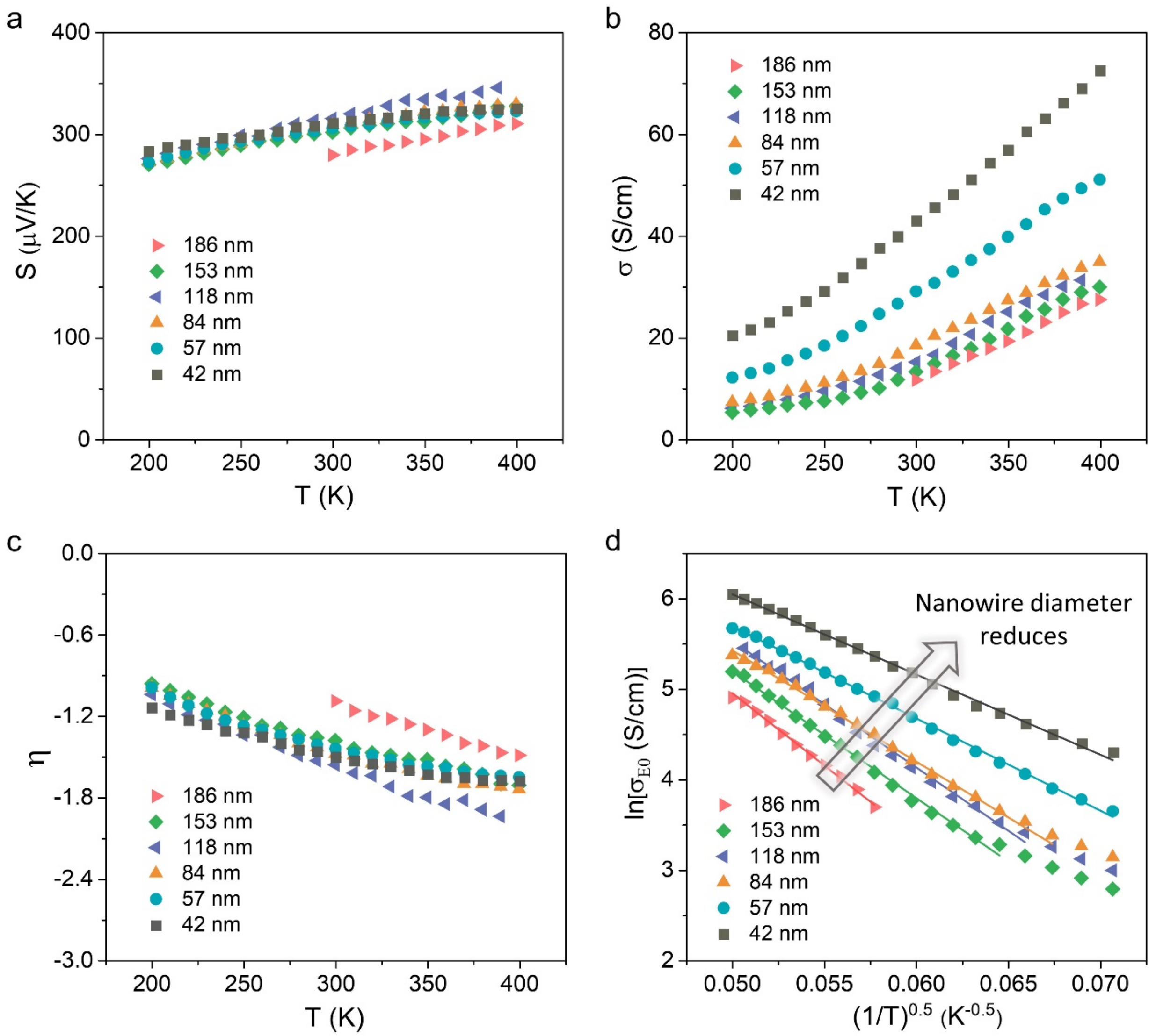

Figure 4.3- Kang-Snyder model on temperature dependent electrical transport properties. (a-b) Measured temperature dependent Seebeck coefficient and electrical conductivity of Te-PEDOT:PSS hybrid nanowires with different diameters. (c) Reduced chemical potential $\eta = (E_F - E_t)/k_B T$ of different diameter Te-PEDOT:PSS nanowires plotted as a function of temperature. (d) $ln(\sigma_{E0})$ is plotted as a function of $T^{-0.5}$, and hopping energy W_γ is extracted by taking the slope of $ln(\sigma_{E0})$ vs $T^{-0.5}$ curve.

Table 4.1 Electrical transport parameters for Te-PEDOT:PSS core/shell nanowires with different diameters.*

Diameter (nm)	**Reduced chemical potential, η**	**Transport coefficient, σ_{E0} (S/cm)**	**Hopping energy, W_{γ} (eV)**
186	-1.09	40.12	2.13
153	-1.38	59.01	1.69
118	-1.56	79.45	1.59
84	-1.48	90.07	1.30
57	-1.44	136.78	0.90
42	-1.50	213.49	0.68

*: All parameters are extracted using Kang-Snyder model based on the measured room temperature results.

4.3.3 Gate-modulated electrical conductivity measurements

To quantify the mobility enhancement due to templating which enhances the electrical conductivity of smaller diameter Te-PEDOT:PSS core/shell nanowires, field effect modulated experiments were conducted (details in Section 4.7.7), as has been previously reported for Sb_2Te_3 nanowires [153], and Ge-Si core/shell nanowires [154]. Three nanowires with different diameters were measured, and the formation of Ohmic contact between the nanowire and the metal electrodes was confirmed by the linear I-V curves at various gate voltages (**Figure 4.15a**). As confirmed earlier, since the electrical current primarily flows through the organic shell in Te-PEDOT:PSS nanowires, the measured source-drain current I_{DS} can be approximated as $I_{DS} = \frac{V_{DS}}{R_{shell}} = \frac{V_{DS}\sigma_{shell}\pi Dt}{L}$, where V_{DS} is the source-drain voltage, σ_{shell} is the polymer shell electrical conductivity, D is the nanowire diameter, t is the shell thickness, and L is the nanowire length. In contrast to conventional single-phase nanowires in which the measured I_{DS} is normalized by the cross-sectional area, as shown in **Figure 4.4a**, the shell cross-sectional area over length normalization ($I_{DS}^{*}=I_{DS}/(\pi Dt/L)$) is used to ensure a meaningful comparison between different diameter hybrid nanowires, where V_{DS} is kept at 0.2 V. As expected, all nanowires show increased I_{DS}^{*} as V_G reduces, as a result of p-type behavior and hole transport. More importantly, I_{DS}^{*} increases for nanowires with smaller diameter at $V_G = 0$, which provides clear evidence that σ_{shell} increases as the core diameter reduces.

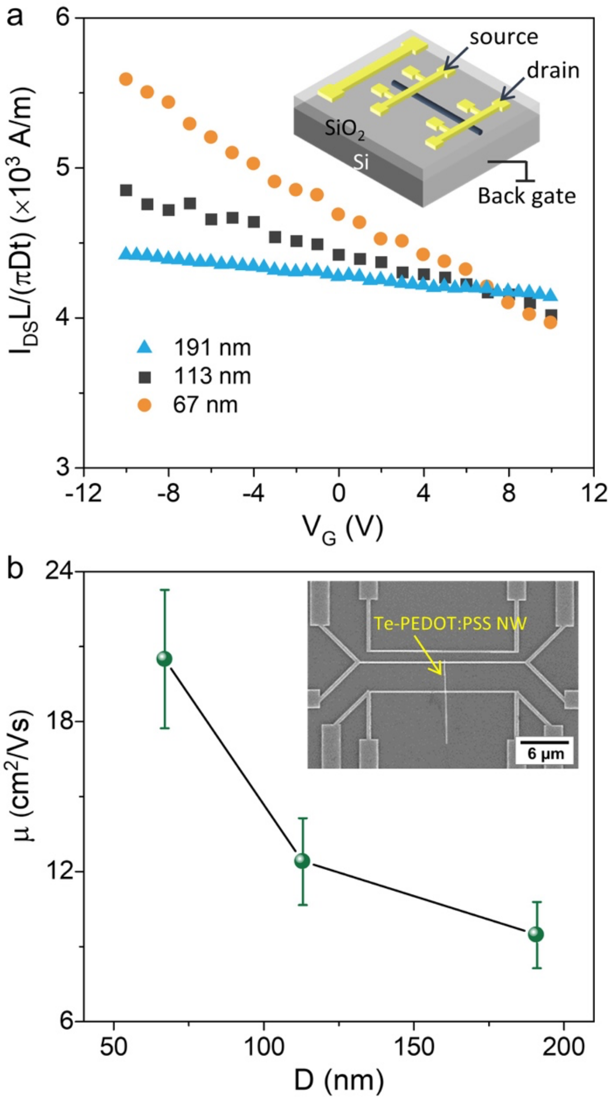

Figure 4.4- Gate modulated electrical conductivity measurements. (a) Measured source drain current normalized with respect to the ratio of nanowire shell cross-sectional area over length ($I_{DS}^{*}=I_{DS}/(\pi Dt/L)$) of three Te-PEDOT:PSS core/shell nanowires as a function of gate voltage, V_G, where the source drain voltage, V_{SD}, is kept at 0.2 V. Inset: schematic drawing of the device. (b) Hole mobility, μ, plotted as a function of nanowire diameter, D. Inset: SEM image of the device used for the gated electrical conductivity measurements. The measurement uncertainties of μ is mainly from the uncertainties in nanowire length and diameter measurements.

The enhancement in the shell electrical conductivity can be related to hole mobility, which is extracted using the calculated transconductance g_m from the measured I_{DS}-V_G data (**Figure 4.15b**) as $\mu = (g_m L^2)/(V_{DS}C)$, where C is the capacitance of the gate oxide (details can be found in **4.11**) [154]. **Figure 4.4b** shows the hole mobility, which increases from 9.46 to 20.5 cm^2/Vs as the wire diameter reduces from 191 to 67 nm; this mobility value is very close to that of PEDOT thin films (26.6 cm^2/Vs) synthesized using oxidative chemical vapor deposition [155], thus confirming the high crystallinity and morphological order of the organic shell in the hybrid. Moreover, the mobility increase follows the same increasing trend as the Kang-Snyder model transport coefficient σ_{E0} with reducing wire diameter. Thus, both approaches (qualitative and quantitative) independently validate the hypothesis that increased carrier mobility due to morphological ordering (templating) is indeed responsible for the enhanced thermoelectric performance in smaller diameter wires.

To understand the driving force and extent of templating in different nanowires, we must consider how PEDOT chains interact with the Te nanowire surface as diameter reduces. The morphology of polymeric materials is typically characterized via a variety of techniques such as grazing incidence wide/small angle x-ray scattering, atomic force microscopy and electron diffraction [156–158]. While the structure of PEDOT:PSS has been effectively resolved through these methods, the polymer blend itself is typically semi-amorphous, resulting in a lack of strong scattering peaks that are common in other conjugated polymers [159,160]. This fact, paired with the ultra-thin nature of the organic shell (1-2 nm thick) seated on top of a highly ordered, inorganic Te core, make it exceedingly difficult to experimentally obtain structural detail of the polymer shell in the hybrid. Nevertheless, we can leverage recent theoretical work to provide some insight on the improved structural order of the polymer chains as the Te core diameter reduces [51,110,161,162]. As demonstrated by Ouyang *et al.* and Ghosh *et al.,* surface energy of Te nanowires is directly proportional to the nanowire diameter [110,161]. Thus, as the diameter decreases, this suppression of surface energy would facilitate polymer self-assembly on the nanowire surface [51,162]. Furthermore, MD simulations performed by Kumar *et al.* reveal that a ~2x reduction in interaction energy at the interface of Te-PEDOT as compared to $Cu_{1.75}Te$-PEDOT facilitates the movement of PEDOT chains, thus enabling improved self-assembly [51]. The question of epitaxial polymer crystallization is a complex one that is dependent on various factors, such as temperature, polymer-inorganic facet interaction energy, and polymer chain mobility [163]. Based on the results of this study, we posit that as the wire diameter shrinks, the polymer shell crystallites become more ordered, greatly enhancing local and long-range connectivity of the organic shell, as shown in **Figure 4.1d**. We expect this effect to plateau as the inorganic core diameter approaches the polymer crystallite size, which acts as the inherent ordering limit (near single crystal). Theoretical calculations have shown that a maximum power factor of ~31200 $\mu W/mK^2$ could be achieved at a carrier concentration of 6.5×10^{19} cm^{-3} for single crystal PEDOT [164], which is the upper limit for the thermoelectric power factor of the ordered polymer shell in this hybrid nanowire. However, future experiments and theoretical modeling are needed to provide further insight on the exact mechanism for the high thermoelectric power factor in this hybrid material system.

4.3.4 Thermal transport in hybrid nanowires

With the organic shell confirmed to be the primary channel for charge transport, the next step is to reveal the role of organic shell and inorganic core in thermal transport. To this end, we performed temperature dependent thermal conductivity measurements on the same set of individual Te-PEDOT:PSS hybrid nanowires of different diameters. Shown in **Figure 4.5a**, the measured κ of the largest nanowire is 2.01 W/m-K at 300 K, and it shows a continually decreasing trend as the diameter reduces, reaching 0.68 W/m-K for the 42 nm diameter nanowire. Combined with the measured power factor, these collectively result in a ~14x enhancement in ZT compared to the 186 nm diameter nanowire, reaching a value of 0.18 at 300 K (**Figure 4.5b**), and an even higher ZT value of 0.54 is achieved at 400 K (**Figure 4.5c**). Traditional efforts to suppress thermal transport in thermoelectric materials typically result in an adverse impact on σ due to increased scattering events or a decrease in carrier concentration [128]. Our results reveal that by reducing the wire diameter, we are able to reduce the κ while simultaneously increasing σ to obtain an enhanced thermoelectric ZT in Te-PEDOT:PSS nanowires (**Figure 4.5d**). It should be noted that the ZT value achieved (0.54 at 400 K) for these undoped individual nanowires is the highest among all Te-PEDOT:PSS materials prepared under various conditions [52,53,112,132,134,135,145], and our measurement technique ensures the highest accuracy as all three parameters (σ, S, and κ) are measured along the same axial direction of the same sample, unlike in previous thin films measurements.

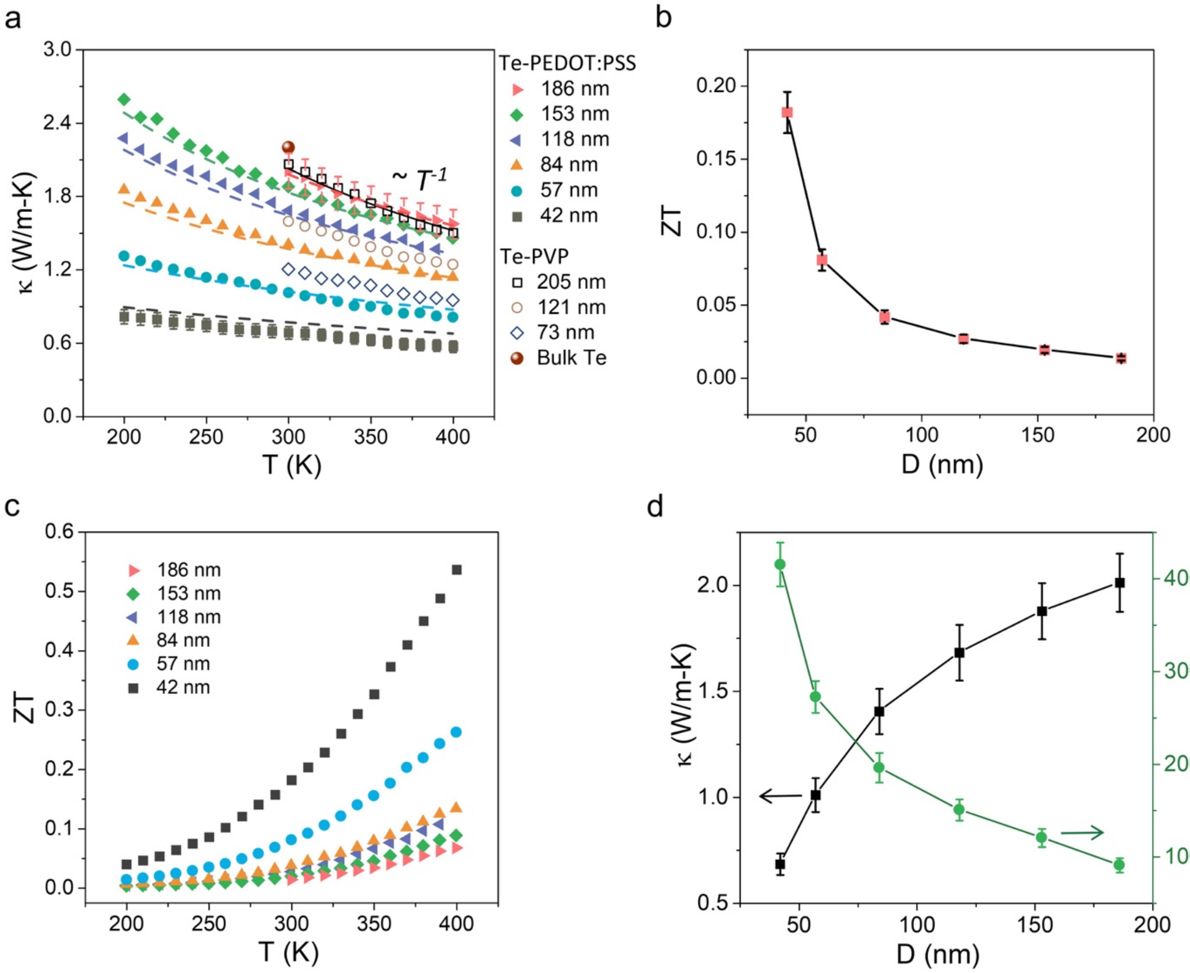

Figure 4.5- Thermoelectric properties of hybrid nanowires. (a) Temperature dependent thermal conductivity of Te-PEDOT:PSS and Te-PVP nanowires with different diameters, where the measured room temperature thermal conductivity for bulk Te is also plotted for comparison [1]. The dashed lines are modeled thermal conductivity of each nanowires considering the effects of phonon-boundary scattering. (b) Size-dependent thermoelectric figure of merit, ZT, of Te-PEDOT:PSS hybrid nanowires at room temperature. (c) Temperature-dependent ZT of Te-PEDOT:PSS hybrid nanowires with various diameters. (d) Size-dependent thermal conductivity and power factor of Te-PEDOT:PSS hybrid nanowires at room temperature, which show inverse relationship with respect to the nanowire diameter. Here, the measurement uncertainties of κ is mainly from the uncertainties in nanowire length and diameter measurements, and the uncertainties of ZT is calculated based on the respective uncertainties in S, σ, and κ.

To quantify the electronic contribution to thermal transport, we estimate the electronic thermal conductivity based on the Wiedemann-Franz law as $\kappa_e = L\sigma T$, where L is the Lorenz number. For the 42 nm diameter wire, the estimated κ_e based on the degenerate limit is 0.03 W/m-K at 300 K, which highlights the negligible role of electrons in thermal transport in this system. This is further confirmed by performing temperature dependent κ measurements that follow approximately a $1/T$ relation above 300 K (**Figure 4.5a**), signifying the dominant role of Umklapp phonon scattering. Additionally, phonons as the dominant heat carriers in these hybrids is confirmed by measurements on Te-PVP nanowires that show thermal conductivity values that are similar to Te-PEDOT:PSS nanowires of comparable diameters (**Figure 4.5a**). If electrons were contributing significantly to thermal transport, a much lower κ should be observed for Te-PVP wires based on the fact that their σ is at least 3x lower than that of Te-PEDOT:PSS (**Figure 4.2**). This clearly establishes phonons as the dominant heat carriers in this system, and it is now possible to understand the size dependence of κ. MD simulations on other hybrids such as Si/a-SiO$_2$ core/shell nanowires have shown that, quasi-stationary modes formed in the amorphous shell carry heat much less efficiently than the propagating phonon modes in the crystalline core [136]. Based on the measured κ of semi-crystalline PEDOT:PSS (0.5 W/m-K) [98] and shell thickness of ~1.45 nm, we calculate that the organic shell contributes less than 13% to the total thermal transport using the simple parallel resistance model (details in S8). In addition, prior theoretical work has shown that 90% of thermal transport along the axial direction in Te can be attributed to phonons with a MFP less than 200 nm [165]. Thus, as the nanowire diameter reduces, phonon-boundary scattering becomes increasingly important and will act to suppress the overall thermal conductivity. This effect can be clearly seen from the flattened $\kappa(T)$ curves for nanowires with shrinking diameter (**Figure 4.5a**). As a result, we posit that the inorganic core is the dominant channel for thermal transport, and the overall reduction in κ for smaller diameter nanowires is due to the increased impact of phonon-boundary scattering.

To confirm this hypothesis, we modeled the lattice thermal conductivity of the hybrid nanowire based on the Callaway-Holland model (details in section Section 4.7.9) [166,167]. In the calculation, we only consider thermal transport in the Te core and neglect the contribution of the thin PEDOT:PSS shell. The calculation is performed along the nanowire axial direction based on the phonon dispersion relation of bulk Te [165]. We consider the mode-dependent phonon relaxation time using Matthiessen's rule, taking into account Umklapp, boundary, and defect scattering mechanisms [166,167]. The dashed lines in **Figure 4.5a** are modeled temperature dependent κ in which only the phonon-boundary scattering term is altered based on nanowire diameter, showing excellent agreement with the experimental results.

4.4 Conclusions

Although Te-PEDOT:PSS is not a new hybrid material system and has been widely studied in previous work [52–54,112,132,134,135], by employing a carefully controlled single nanowire transport study, we have been able to experimentally capture the effects of nanoscale templating at the organic/inorganic interfaces for the first time, which helps to fill in the knowledge gap between atomic-scale simulations [51] and bulk thin film measurements [52–54,112,132,134,135]. Our findings reveal that in nanostructured hybrid materials comprising a thin electrically conductive organic shell coated on a crystalline inorganic core, electrical transport predominantly occurs through the organic shell, while thermal transport is primarily driven by the inorganic core, thereby offering an avenue to decouple these notoriously linked parameters for thermoelectric applications. Due to the fundamental nature of this study, it should be noted that the materials discussed are undoped and have not undergone additional post-processing. Thus, there is great potential to further optimize the thermoelectric properties and achieve even higher *ZT* values. Furthermore, the insight gained from this model system helps establish a framework for next generation organic-inorganic hybrid thermoelectric materials through design principles of interfacial energy minimization (for improved morphology and long-range order) and favorable energetic pairing for optimal de-doping effects (for improved electronic energetics) between the hard and soft components. From these insights it is possible to envisage the rational design of a plethora of high performing, advanced materials composed of new pairings of inorganic nanostructures (perhaps with more environmentally friendly options such as bismuth or sulfur) with conjugated polymers and small molecules to design new p-type materials and more elusive n-type hybrids as well.

In summary, through combining thermoelectric property measurements on single Te-PEDOT:PSS nanowires with the Kang-Snyder model and gate-modulated electrical conductivity experiments, we show that electrical conductivity is enhanced at smaller nanowire diameter due to an increase in the charge carrier mobility of the PEDOT:PSS shell, which in turn is attributed to a physical templating effect at the organic-inorganic interface. Simultaneously, thermal conductivity is reduced at smaller diameter nanowires due to strong phonon boundary scattering in the Te core. Specifically, for the hybrid nanowire with the smallest diameter of 42 nm, a σ of 43.1 S/cm, S of 310.9 μV/K and a low κ of 0.68 W/m-K, is achieved, translating to a *ZT* value of 0.18 at 300 K. For this same nanowire, an even greater *ZT* of 0.54 can be achieved at a temperature of 400 K, which is, to the best of our knowledge, the highest *ZT* achieved to date for this hybrid material. These results demonstrate the ability to decouple electronic and thermal properties in organic-inorganic hybrid materials for thermoelectric applications. Additionally, it realizes the critical nature of the organic component and the need for heightened control over its morphology and electronic nature. As a result, the work detailed in Chapter 5 takes a step back from hybrid materials to instead explore avenues for tuning structure and transport in a conjugated polymer system. By first establishing fundamental understanding and control over a purely organic system, it will then be easier to rationally apply that understanding to a more complex hybrid system in the future.

4.5 Materials and Methods

4.5.1 Material synthesis

Synthesis of Te-PEDOT:PSS core/shell nanowires were performed according to the ligand exchange procedure published by Sahu *et al.*.[50]. PEDOT:PSS (Clevios PH1000) was purchased from Heraeus and was vortexed and filtered but otherwise underwent no further processing. Tellurium dioxide (99.9995%), polyvinylpyrrolidone (PVP, average molecular weight 40 kDa), sodium hydroxide (ACS reagent, ≥97.0%, pellets), ethylene glycol (ReagentPlus®, ≥99%), hydrazine hydrate (78-82%, iodometric), and sodium sulfide were purchased from Sigma Aldrich. The single crystal Te nanowires are initially synthesized with PVP as the surface ligand to act as the structure directing agent. Once synthesized, the wires then undergo a multistep ligand exchange procedure where the final product is coated with a thin conformal layer of PEDOT:PSS. Hybrid nanowires are then drop cast onto glass substrates.

4.5.2 Structural characterization

A FEI Titan 60-300 microscope was operated at an accelerating voltage of 200 kV. Real space images were taken with a spot size of 3 and an exposure of 0.5 seconds for all structures. Selected area electron diffraction (SAED) was taken for 3 nanowires with slightly different conditions. For all structures, a SAED aperture of 40 μm and a camera length of 160 mm were used. For nanowires with diameters of 50 and 80 nm, a spot size of 7, and an exposure of 0.5 seconds was used. For the nanowire with a diameter of 170 nm was imaged, a spot size of 9 and exposure of 0.3 seconds was used. For additional polymer shell thickness characterization a FEI monochromated F20 UT Tecnai was operated at an accelerating voltage of 200 kV. Real space images were taken with a spot size of 3 and an exposure of 0.7 seconds.

4.5.3 Thermoelectric properties measurements on individual nanowires

For thermoelectric measurements, the hybrid nanowire meshes were first immersed in reagent alcohol and sonicated for ~10 seconds, and the nanowires suspension was then drop casted on a piece of polydimethylsiloxane (PDMS). Next, an individual nanowire was picked up by a sharp probe, mounted on an in-house assembled micromanipulator, and laid between two side-by-side suspended membranes integrated with micro- heaters/thermometers. The thermoelectric properties of individual nanowires were measured in a cryostat (Janis VPF-800) operated under a high vacuum ($<1 \times 10^{-6}$ mbar) with a dual radiation shield configuration. EBID of the Pt/C composite was performed at the contacts between the nanowire and Pt electrodes using a dual-beam system (FIB/SEM, FEI Quanta) to establish good electrical contacts and minimize the contact thermal/electrical resistance. The electrical resistance measurement was performed before thermal measurements at each designated temperature point using the four-probe method. During the measurements, we used a DC voltage output from the data acquisition (DAQ) board (National Instruments PCI-6052e), which was connected to a large resistor (1 MΩ) in series with the outer electrodes of the microdevice. By varying the output DC voltage, a sweeping DC current was applied to the Te-PEDOT:PSS nanowire, with the voltage difference between the two inner electrodes measured by a voltage amplifier (Stanford Research Systems, SR560), and the DC current recorded by a high accuracy current amplifier (Keithley 6487). The temperature dependent electrical resistance (*R(T)*) of each measured sample is subsequently obtained by fitting the linear I-V curve.

In order to increase the sensitivity for thermal connectivity measurements, a Wheatstone bridge circuit was adopted through introducing a blank device, which helps to reduce the noise from the temperature fluctuations of the sample holder. During the thermal measurements, we also measured the Seebeck coefficient for each sample by monitoring the temperature difference of the two suspended membranes and the induced voltage difference (SR560) across the two inner electrodes.

4.5.4 Kang-Snyder charge transport model

The transport function $\sigma_E(E, T)$, also regarded as energy dependent conductivity, can be described by:

$$\sigma_E\left(E,T\right)=\sigma_{E0}(T)\left(\frac{E-E_t}{k_B T}\right)^s, \tag{4.4}$$

Through integrating by parts, Eq. (1) and (2) simplify to:

$$\sigma=\sigma_{E0}(T)\times sF_{s-1}\left(\eta\right), \tag{4.5}$$

and

$$S=\frac{k_B}{e}\left[\frac{\left(s+1\right)F_s\left(\eta\right)}{sF_{s-1}\left(\eta\right)}-\eta\right], \tag{4.6}$$

respectively. Here, F is the complete Fermi-Dirac integral: $F_i(\eta)=\int_0^\infty \frac{\varepsilon^i}{1+e^{\varepsilon-\eta}}d\varepsilon,$ and η is reduced chemical potential: $\eta=(E_F\text{-}E_t)/k_BT$, where E_F is Fermi level, E_t is transport energy, below which there is no contribution to the conductivity, k_B is Boltzmann constant, and T is absolute temperature [146].

4.6 Acknowledgments

4.6.1 Funding

This work was partially performed at the Molecular Foundry, Lawrence Berkeley National Laboratory, and was supported by the Department of Energy, Office of Science, Office of Basic Energy Sciences, Scientific User Facilities Division of the U.S. Department of Energy under Contract No. DE-AC02-05CH11231. M.P.G. gratefully acknowledges the National Science Foundation for fellowship support under the National Science Foundation Graduate Research Fellowship Program. A.K.M acknowledges funding support from the ITRI-Rosenfeld Fellowship from the Energy Technologies Area at Lawrence Berkeley National Laboratory. We thank Prof. Junqiao Wu for allowing us access to the probe station for nanowire manipulation.

4.6.2 Author Contributions

L.Y. conducted thermoelectric properties measurements and gate modulated electrical conductivity measurements. L.Y., M.P.G., and A.K.M performed thermoelectric modeling using Kang-Snyder model. M.P.G. and K.H. synthesized Te-PEDOT:PSS and Te-PVP hybrid nanowires. A.B. and M.P.G. performed TEM characterizations. L.Y., M.P.G. and A.K.M. compiled and analyzed results. M.P.G., L.Y., J.J.U. and R.S.P. conceived and directed the project. L.Y., M.P.G., and A.K.M. wrote the manuscript with input from all authors.

4.7 Supporting Information

4.7.1 Transmission Electron Microscopy Examination

In order to confirm that each single wire is truly comparable to one another and insure that all observed electronic and thermal effects could be appropriately attributed to either the organic or inorganic phases, high resolution transmission electron microscopy (HRTEM) and selective area electron diffraction (SAED) were performed on Te-PEDOT:PSS nanowires. The Te core appears to be single crystalline in nature as can be seen in both the HRTEM images and SAED insets through inspection of the lattice fringes and discrete diffraction spots, respectively. **Figure 4.6a-b** shows representative HRTEM and SAED images of Te-PEDOT:PSS nanowires of two different diameters.

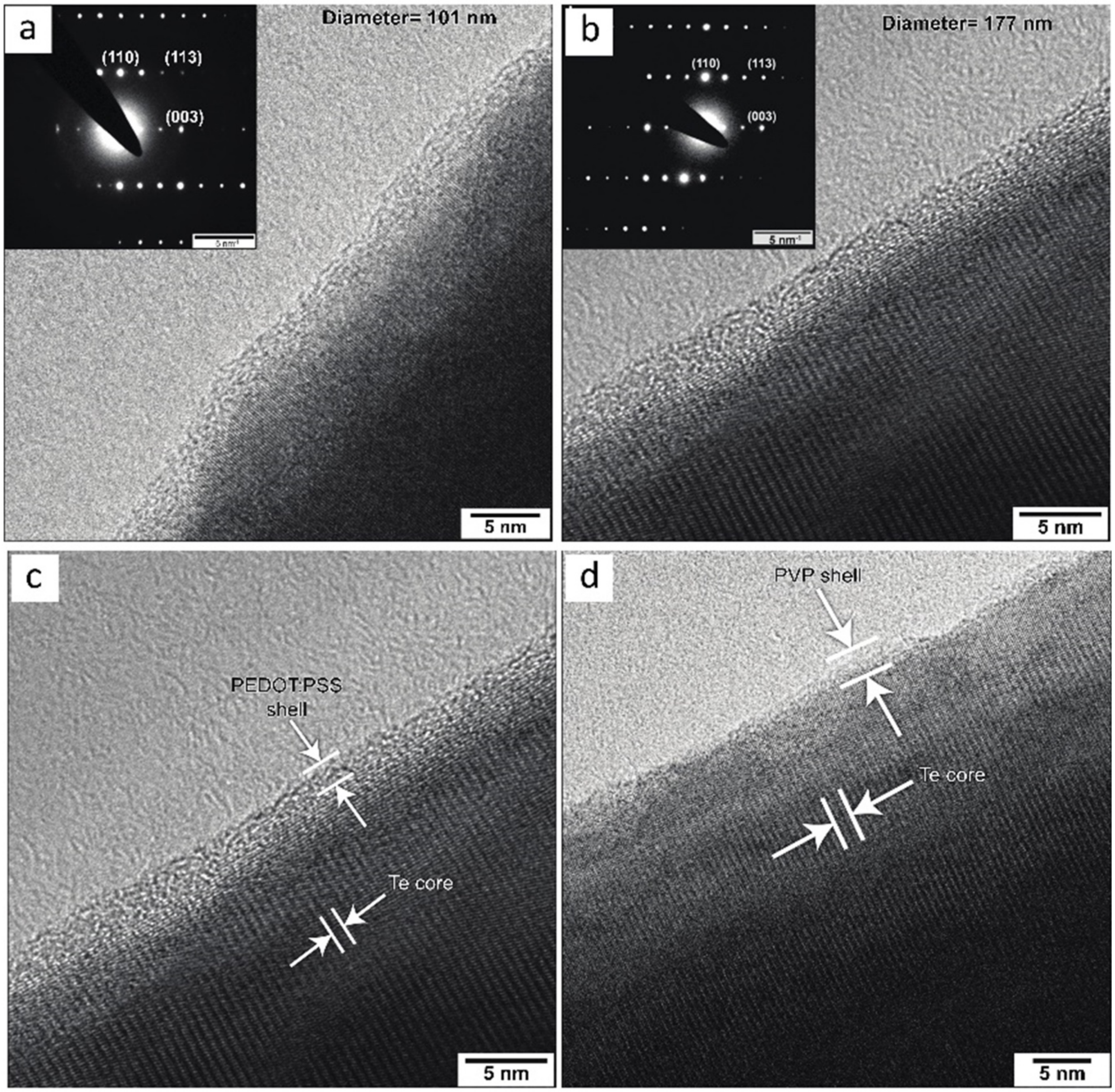

Figure 4.6- Organic shell thickness characterization. HRTEM micrographs and SAED insets for nanowires of diameter (a) 101 nm and (b) 177 nm showing crystalline structure. HRTEM micrographs showing representative images of the shell thickness of (c) Te-PEDOT:PSS and (d) Te-PVP hybrid nanowires.

In addition to efforts to confirm single crystallinity, work was also done to determine the average organic polymer shell thickness for both Te-PEDOT:PSS and Te-PVP hybrid nanowires. To accurately determine the shell thickness, we used high resolution transmission electron microscopy (HRTEM) at three different locations along the axial direction of the Te-PEDOT:PSS hybrid nanowires, and shell thickness value is determined by averaging 9 data points for each nanowire. Representative micrographs are shown in **Figure 4.6**. We plot the average shell thickness for hybrid nanowires with different diameters in **Figure 4.7**. It can be seen that although the average shell thickness measured from five different diameter nanowires is 1.45 ± 0.34 nm (uncertainty of ~23%), this uncertainty is dominated by variations along the length of the same nanowire, but not by differences between different nanowires. In fact, the standard deviation of the averaged shell thickness for five different diameter nanowires is only 0.032 nm, which is only 2.2% of the average shell thickness value. This confirms that there is minimal shell thickness variation across hybrid nanowires with different diameters.

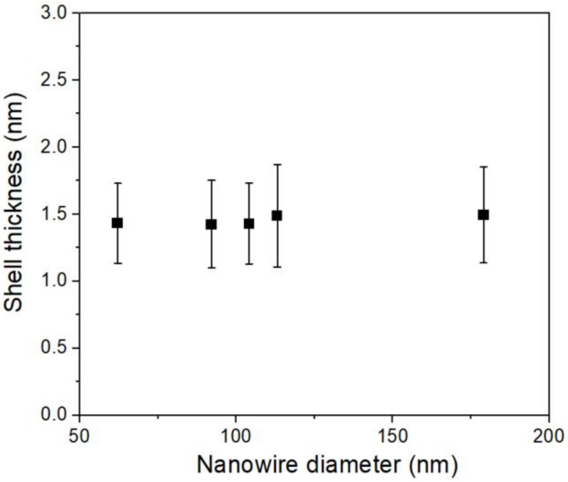

Figure 4.7- Measured average shell thickness and calculated standard deviation for Te-PEDOT:PSS hybrid nanowires with different diameters.

4.7.2 Contact Thermal Resistance and Background Thermal Conductance

For all nanowires measured in this work, the contacts between the nanowire and the underlying Pt electrodes were treated with electron beam induced deposition (EBID) of Pt, as shown in the inset of **Figure 4.8**. To verify that the Pt deposition could reduce the contact thermal resistance to a negligible level, we measured the Seebeck coefficient from different sets of electrodes. This method essentially uses the nanowire as a differential thermocouple to determine the temperature drops at the contacts.[140] We measured the Seebeck voltages between both the two inner electrodes (2&3) and the two outer electrodes (1&4), which would otherwise share different temperatures if there exists large contact thermal resistance. The nearly overlapped Seebeck coefficient from the two sets of the electrodes in **Figure 4.8**, however, suggests negligible contact thermal resistance.

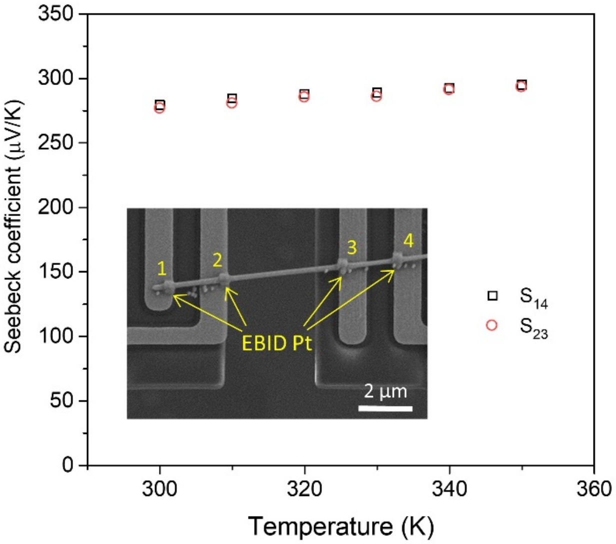

Figure 4.8- Contact thermal resistance characterization. The inset is a SEM image showing a Te-PEDOT nanowire bridging the two suspended side-by-side membranes with all four contacts bonded with EBID Pt deposits. The scale bar of the SEM image is 2 μm.

In fact, when there exists non-negligible contact thermal resistance, as the temperature of the nanowire segments in contact with each membrane varies along the length as a result of heat transfer between the nanowire and the membrane, each nanowire segment in contact with the membrane should be treated as a fin. Mavrokefalos *et al.* have shown that the thermal contact resistance between the nanowire and each membrane is essentially fin thermal resistance, which can be described as[140]

$$R_c = \frac{1}{\kappa A m \tanh(m L_c)} . \tag{4.7}$$

Here, κ and A are the thermal conductivity and cross-section of the nanowire, respectively, L_c is the length of the nanowire segment in conatct with one membrane, and $m = \sqrt{hw/\kappa A}$, where h is the thermal contact conductance per unit area between the nanowire and the membrane, and w is the conctact width between the nanowire and membrane.

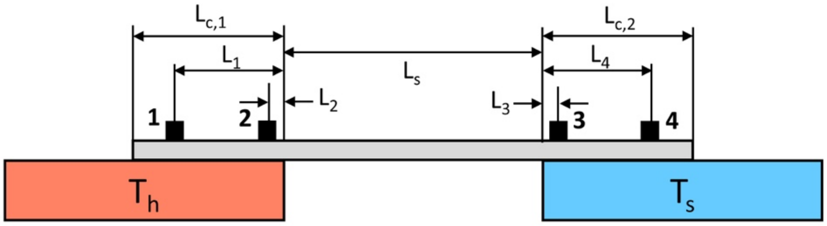

Figure 4.9- Schematic drawing showing a nanowire sample placed to bridge the gap of the two suspended membranes.

Note that the measured total thermal resistance can be described as $R_{tot} = R_c + R_{in}$, where R_c is the contact thermal resistance, and $R_{in} = L_s/\kappa A$ is intrinsic nanowire thermal resistance (L_s is the sample suspended length). As the ratio of the measured Seebeck coefficient at points 1 and 4, S_{14}, over points 2 and 3, S_{23}, can be described as[140]:

$$\gamma = \frac{S_{14}}{S_{23}} = \frac{T_1 - T_4}{T_2 - T_3} = \frac{\gamma_{14}}{\gamma_{23}}, \tag{4.8}$$

where

$$\gamma_{14} = 1 + \frac{1 - \cosh\left[m\left(L_{c,1} - L_1\right)\right]/\cosh\left(mL_{c,1}\right)}{L_s m \tanh(mL_{c,1})} + \frac{1 - \cosh\left[m\left(L_{c,2} - L_4\right)\right]/\cosh\left(mL_{c,2}\right)}{L_s m \tanh(mL_{c,2})}, \tag{4.9}$$

$$\gamma_{23} = 1 + \frac{1 - \cosh\left[m\left(L_{c,1} - L_2\right)\right]/\cosh\left(mL_{c,1}\right)}{L_s m \tanh(mL_{c,1})} + \frac{1 - \cosh\left[m\left(L_{c,2} - L_3\right)\right]/\cosh\left(mL_{c,2}\right)}{L_s m \tanh(mL_{c,2})}. \tag{4.10}$$

As such, the parameter m can be obtained based on Eq. (S3-4) using the measured γ value, and

$$\alpha = \frac{R_{tot}}{R_{in}} = 1 + \frac{1}{L_s m}\left[\frac{1}{\tanh(mL_{c,1})} + \frac{1}{\tanh(mL_{c,2})}\right]. \tag{4.11}$$

Then, the ratio of contact thermal resistance to the measured total thermal resistance (R_c/R_{tot}) can be calculated from Equation (4.11) based on $R_{tot} = R_c + R_{in}$, which is determined to be 1.6% at 300 K for the 186 nm diameter Te-PEDOT:PSS nanowire shown in **Figure 4.8**. This again proves that the contact thermal resistance is negligible compared with the measured total thermal resistance.

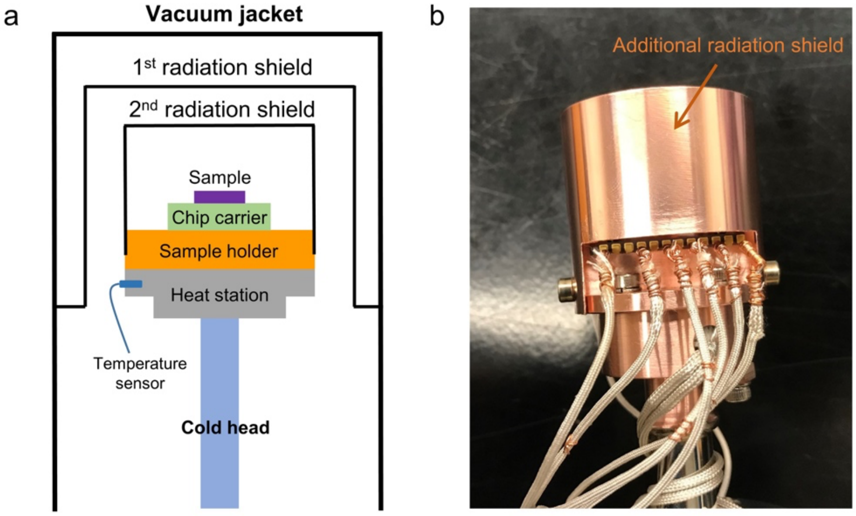

Figure 4.10- Double radiation shield scheme. (a) Schematic drawing showing the inside of the cryostat. (b) A picture showing the approach of mounting the additional radiation shield on the sample holder. Photo Credit: Lin Yang, Lawrence Berkeley National Laboratory.

Radiation heat transfer needs to be carefully considered in the individual nanowire measurement. On the one hand, radiation heat loss from the heating stage to the surrounding environment would cause temperature deviation from the setting temperature. As shown in **Figure 4.10a**, to minimize the radiation heat loss, an additional radiation shield is mounted directly onto the sample stage, which ideally shares the same temperature of the sample holder. By doing this, we can largely avoid radiation heat loss from the device.[139]

On the other hand, radiation heat transfer between the two suspended membranes would contribute to the measured total thermal conductance, which needs to be subtracted in order to obtain the intrinsic sample thermal conductance.[139] To do this, we measured the thermal conductance of an identical empty device with no nanowire bridging the two membranes. As the microheater devices were fabricated from the same batch, sharing nominally identical structures and dimensions, it is reasonable to assume that all devices with the same gap distance have approximately the same background thermal conductance, G_{bg}. The measured G_{bg} data were fitted to a 4th order polynomial function and was subsequently subtracted from measured thermal conductance of the sample. Shown in **Figure 4.11** are the measured total thermal conductance, G_{bg+nw}, background thermal conductance, G_{bg}, and the sample thermal conductance after the background subtraction, G_{nw}, where the measured sample is 57 nm diameter Te-PEDOT:PSS core/shell nanowire. It can be seen starting from 350 K, the background thermal conductance becomes even larger than the sample intrinsic thermal conductance. At 400 K, G_{nw} is 0.58 nW/K, while G_{bg} is 0.81 nW/K. In this case, it is imperative to cancel out the contribution from the background radiation heat transfer to get the intrinsic thermal conductivity of the measured sample.

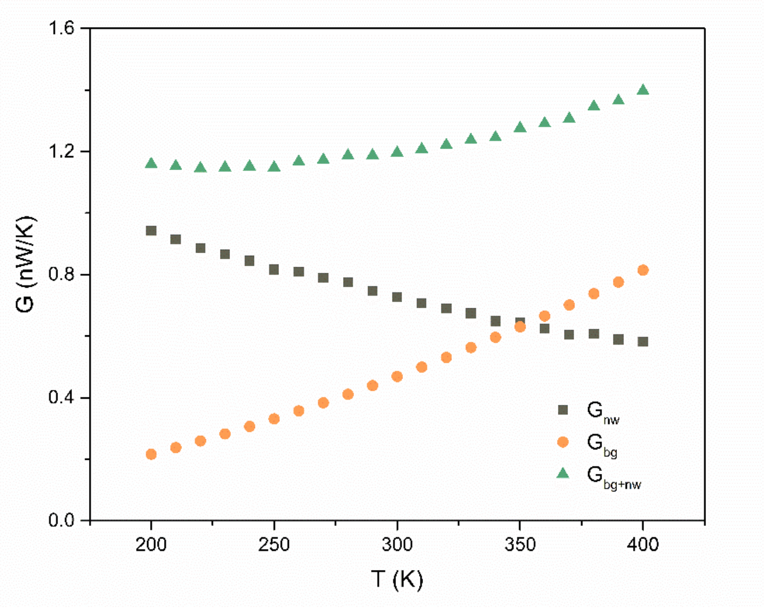

Figure 4.11- Measured total thermal conductance, G_{bg+nw}, background thermal conductance, G_{bg}, and the sample thermal conductance after the background subtraction, G_{nw}, for the 57 nm diameter Te-PEDOT core/shell nanowire.

4.7.4 Temperature Dependent Seebeck Coefficient Measurements

The Seebeck coefficient was also measured for each sample. During the thermal measurements, through monitoring the temperature difference of the two suspended membranes and the induced voltage difference (SR560) across the two inner electrodes, the Seebeck coefficient is derived by $S_{measured} = -V_{total}/\Delta T$. The measured value includes contributions from the nanowire as well as the two platinum electrodes deposited on the SiN_x beams supporting the heating and sensing membranes. Therefore, the measured voltage difference is $V_{total} = V_{Pt,h} + V_{nw} + V_{Pt,c}$, where V_{nw} is the potential produced across the nanowire sample, and $V_{Pt,h}$ as well as $V_{pt,c}$ are generated by the temperature difference between the heating membrane and substrate $V_{Pt,h} = -S_{Pt}(T_0 - T_h)$, and the sensing membrane and substrate $V_{Pt,c} = -S_{Pt}(T_c - T_0)$. As such, we have

$$S_{measured} = -\frac{V_{total}}{\Delta T} = -\frac{-S_{Pt}(T_c - T_h) + V_{nw}}{\Delta T} = -S_{Pt} + S_{nw}, \tag{4.12}$$

where S_{Pt} and S_{nw} are the Seebeck coefficient of the Pt electrode and Te-PEDOT:PSS nanowire sample, respectively. By doing this, we are able to obtain the intrinsic Seebeck coefficient of the measured nanowire based on the previously reported S_{Pt}.[141]

4.7.5 Experimental Uncertainty

The electrical resistance of the Te-PEDOT:PSS hybrid nanowires was obtained by linear least square fitting on measured *I-V* curves with a typical one for the 118 nm diameter wire shown in **Figure 4.12a**, and the fitted slope is the electrical resistance. The uncertainties in the calculated slope is expressed by

$$U_R = \sqrt{\frac{\Sigma\left(V_i - RI_i - b\right)^2}{n-2} \times \frac{n}{\left(n\Sigma I_i^2\right) - \left(\Sigma I_i\right)^2}}, \tag{4.13}$$

where *n* is the number of the measured data points, and *b* is the fitted intercept representing the small zero drift of the current source (data acquisition board, National Instruments PCI-6052e). The fitted electrical resistance for this wire is 206721 Ω at 300 K, and the obtained uncertainty 1752 Ω, which is only 0.85% of the fitted electrical resistance. Then, the electrical conductivity is calculated based on $\sigma = L/RA$, where L is nanowire suspended length, and nanowire cross-sectional area $A = (\pi d^2)/4$ (d is the nanowire diameter). Here, the length L and wire diameter d are measured by SEM, and the standard deviations from 5 different measurements are estimated to be 0.15 µm and 2 nm, respectively. Following the error propagation rule to estimate the overall measurement uncertainty for the extracted electrical conductivity, the relative uncertainty of σ can be written as

$$\frac{\delta\sigma}{\sigma} = \sqrt{\left(\frac{\delta R}{R}\right)^2 + \left(\frac{\delta L}{L}\right)^2 + 4\left(\frac{\delta d}{d}\right)^2}. \tag{4.14}$$

Based on the uncertainties determined from respective sources, the relative uncertainty for the electrical conductivity of this 118 nm hybrid nanowire with suspended length of 3.4 μm is calculated to be 5.5%, and the derived measurement uncertainty is 0.84 S/cm (electrical conductivity is 15.2 S/cm).

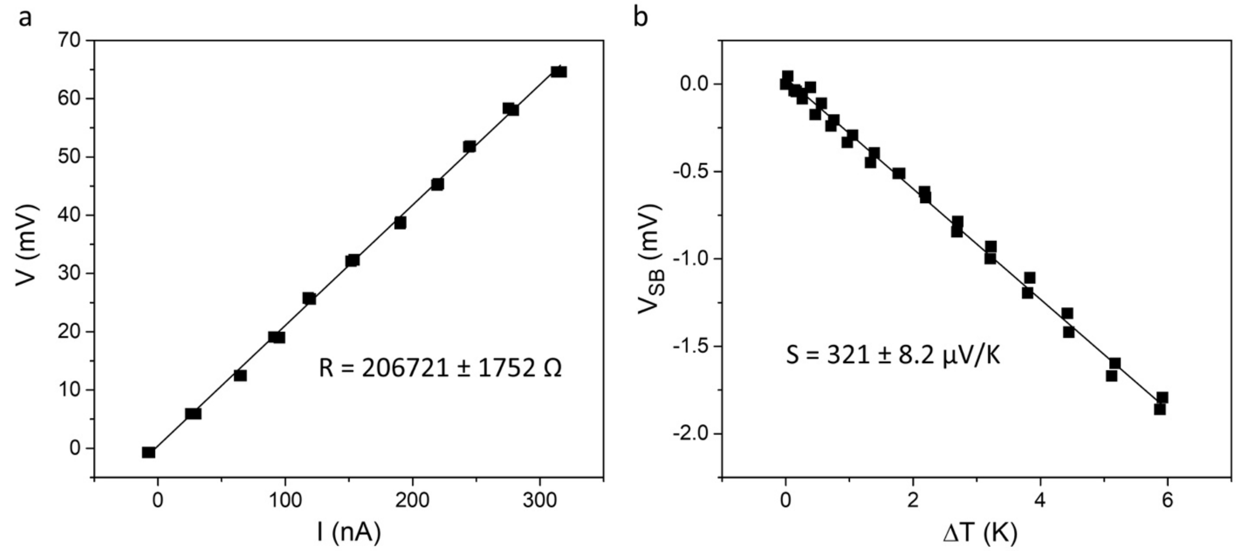

Figure 4.12- Linear fitting to obtain electrical resistance and Seebeck coefficient. (a) Measured *I-V* curve for the 118 nm diameter Te-PEDOT:PSS nanowire at 300 K, where the solid line is the fitted curve using the linear least square fitting approach. (b) Measured temperature difference and induced Seebeck voltage for the same nanowire at 300 K. The Seebeck coefficient is obtained by fitting the slope of the data points using the linear least square fitting method.

The Seebeck coefficient was also obtained by linear least square fit of the measured ΔT-V_{SB} curve (**Figure 4.12b**), where ΔT is the temperature difference between the heating and sensing membranes, and V_{SB} is the measured electrical voltage difference. Based on Section 3, $S_{nw} = S_{measured} + S_{pt}$ (S_{Pt} = -5 μV/K),[141] and the derived uncertainty is 8.2 μV/K at 300 K, or 2.6% of the fitted Seebeck coefficient (316 μV/K).

The thermal conductivity of the nanowire sample is calculated as $\kappa = \frac{GL}{A}$, where G is the measured sample thermal conductance, L is the suspended wire length between the two membranes, and A is the cross-sectional area of the measured sample. The relative uncertainty of κ can be estimated following the error propagation rule considering uncertainties in G, L and A. The uncertainty of the measured thermal conductance $\delta G/G$ mainly comes from the electrical measurements, which is evaluated based on a Monte Carlo method that has been described in our previous work.[141] Using this method, $\delta G/G$ is estimated to be ~3% at 300 K. Based on the uncertainties determined from respective sources, the derived relative uncertainty for the thermal conductivity of this 118 nm hybrid nanowire is 6.4%, which corresponds to measurement uncertainty of 0.11 W/m-K (thermal conductivity for this sample is 1.68 W/m-K).

Thermoelectric figure of merit *ZT* is calculated as $ZT = \frac{S^2 \sigma T}{\kappa}$, where T is temperature. Similarly, relative uncertainty of *ZT* can be calculated following the error propagation rule. Based on the derived measurement uncertainties for σ, S, and κ, we have the relative uncertainty for the derived *ZT* of this 118 nm nanowire as 9.92% at 300 K, which leads to the measurement uncertainty of 0.0027 (*ZT* value for this nanowire sample is 0.027).

For the gate modulated electrical conductivity measurements, the charge carrier mobility is calculated based on $\mu = (g_m L^2)/(V_{DS}C)$, where transconductance g_m is calculated from the measured I_{DS}-V_G data, L is nanowire length between source and drain, and V_{DS} is the constant source-drain voltage. C is the capacitance of the gate oxide, which is described as Equation (4.16). To calculate the overall measurement uncertainty of charge mobility, we need to understand the measurement errors from each source. First, from the measured I_{DS}-V_G data for the 113 nm diameter Te-PEDOT:PSS nanowire shown in **Figure 4.15b**, the transconductance g_m is fitted to be $4.67\times10^{-3} \pm 1.22\times10^{-4}$ μA/V. The measured length for this sample is 3.9 ± 0.2 μm. The relative uncertainty of the gate oxide capacitance can be calculated using the error propagation rule based on Equation (4.16), considering error sources from nanowire length and nanowire radius R (2 nm), which is determined to be 5.14%. Then, using the obtained individual error source, and based on the mobility calculation equation, the relative error of the extracted mobility for the 113 nm sample is 12%, which corresponds to 1.49 cm^2/Vs (measured mobility for this 113 nm diameter sample is 12.4 cm^2/Vs at 300 K).

4.7.6 Parallel Circuit Model to Calculate Hybrid Nanowire Electrical Conductivity and Seebeck Coefficient

To confirm that the observed increased electrical conductivity of the smaller diameter Te-PEDOT:PSS nanowires is not caused by the simple composite effect, here we calculate the effective conductivity of the hybrid nanowire assuming constant properties of each constituent material based on the effective medium theory (EMT). We note that EMT is applicable only to composite systems, and the predicted properties must fall in between that of the individual components; it cannot capture interfacial effects, such as de-doping and physical templating that occur between the organic and inorganic components and has been shown to fail in various hybrid systems.[37,51] Here, our intent it to investigate if the increase in electrical conductivity can be attributed to an increase in the volume fraction of polymer shell as the Te core diameter is reduced. Parallel circuit model can be used to calculate the electrical conductivity and Seebeck coefficient of Te-PEDOT:PSS core/shell nanowires. Shown as the inset in **Figure 4.13a**, for the hybrid nanowire with Te core radius of r and PEDOT:PSS shell thickness of t, the core and shell electrical resistance can be expressed as $R_{core} = \frac{L}{\sigma_{core}\pi r^2}$, and $R_{shell} = \frac{L}{\sigma_{shell}2\pi rt}$, respectively, where L is nanowire length, σ_{core} and σ_{shell} are core and shell electrical conductivity, respectively. Based on the parallel circuit model, the hybrid nanowire electrical resistance can then be described as $R_{hybrid} = \frac{1}{R_{core}^{-1}+R_{shell}^{-1}} = \frac{L}{\sigma_{eff}\pi(r+t)^2}$, from which we are able to calculate the effective electrical conductivity of the hybrid nanowire, σ_{eff}.

In order to calculate σ_{eff}, we need to know the electrical conductivity of Te core and PEDOT:PSS shell. To do this, we approximate σ_{core} to the measured electrical conductivity of Te-PVP nanowires, and extract the PEDOT:PSS shell conductivity based on the measured electrical conductivity of the 186 nm diameter Te-PEDOT:PSS nanowire sample. Then, we use this constant shell electrical conductivity to calculate the hybrid nanowire electrical conductivity as the Te core diameter reduces. **Figure 4.13a** plots the comparison of the calculated σ_{eff} with the measured results, although it also shows an increasing trend as the nanowire diameter reduces, the magnitude of the conductivity increase is much smaller compared with the experimental data. As a result, the calculated σ_{eff} for the 42 nm diameter hybrid nanowire is ~56% lower than our measured value.

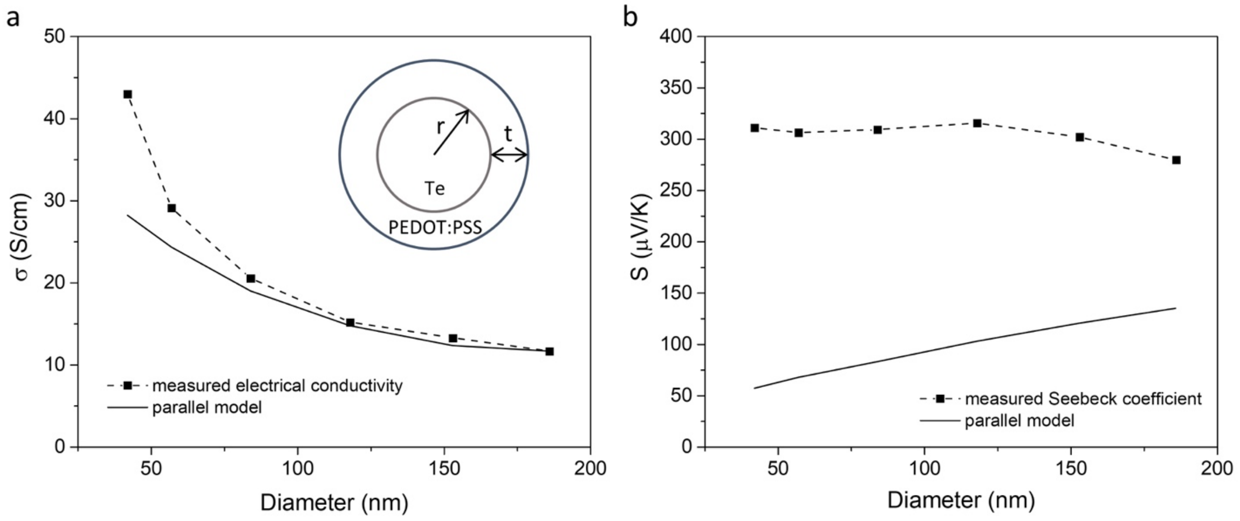

Figure 4.13- Parallel circuit model calculation. (a) Calculated electrical conductivity using the parallel circuit model in comparison with the measured results. Inset: schematic drawing showing the cross-section of the Te-PEDOT:PSS hybrid nanowire. (b) Calculated Seebeck coefficient using the parallel model in comparison with the measured results.

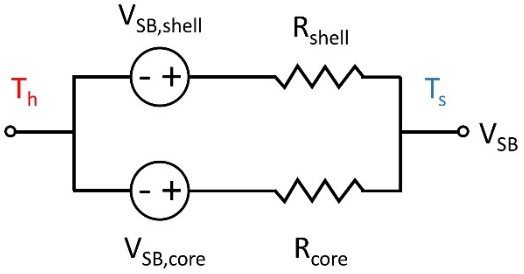

Figure 4.14- Electrical circuit diagram for the hybrid core-shell nanowire under a temperature gradient ($T_h - T_s$), where $V_{SB,shell}$ and $V_{SB,core}$ are shell and core Seebeck voltage, respectively, R_{shell} and R_{core} are shell and core electrical resistance respectively. V_{SB} represents the measured open circuit Seebeck voltage.

Similarly, we can also use the parallel model to calculate the Seebeck coefficient of the hybrid nanowire. For the Te core and PEDOT:PSS shell with Seebeck coefficient of S_{core} and S_{shell}, are subjected to a temperature difference ΔT, and the generated Seebeck voltage for the two components are denoted as $V_{SB,core}$ and $V_{SB,shell}$, respectively (**Figure 4.14**). In this case, the shell will be subjected to current generated by the core and the core will also be subjected to current generated by the shell. As such, the open circuit Seebeck voltage V_{SB} can be described as $V_{SB} = \frac{V_{SB,shell}R_{core}}{R_{core}+R_{shell}} + \frac{V_{SB,core}R_{shell}}{R_{core}+R_{shell}}$. Given that the core and shell have the same temperature difference ΔT, we have $V_{SB,shell} = S_{shell}\Delta T$ and $V_{SB,core} = S_{core}\Delta T$. By plugging these two equations into the V_{SB} equation, and based on $S_{eff} = V_{SB}/\Delta T$, the effective Seebeck coefficient for the core-shell nanowire becomes

$$S_{eff} = \frac{S_{core}R_{shell} + S_{shell}R_{core}}{R_{core} + R_{shell}} \,. \tag{4.15}$$

This equation is identical to that derived in literature comprising two materials connected in parallel.[1] We approximate S_{core} to the measured Seebeck coefficient of Te-PVP nanowire, and S_{shell} is adopted from literature for PEDOT:PSS.[52] The calculated S_{eff} is plotted in **Figure 4.13b** in comparison with the measured results. It can be seen that the calculated results based on the parallel mode is at least 52% lower than the measured data, and also shows a trend opposite to our experimental results. Taken together, we can safely conclude that the observed thermoelectric property enhancement cannot be attributed to effects arising in a simple composite.

4.7.7 Gate Modulated Electrical Conductivity Measurements

For the device fabrication, a target 100 nm SiO_2/Si substrate was first cleaned with "piranha" solution (3:1 sulfuric acid:hydrogen peroxide) in order to remove all organics and contaminating compounds. The Si substrate is degenerately doped to serve as global gate electrode. Patterns are written on the wafer using electron beam (e-beam) lithography (Raith e-beam Lithography System) with polymethyl methacrylate (PMMA) as the resist. Subsequent metal deposition was conducted with a Semicore e-beam evaporator. The metal electrode used in this work is a combination of Ti, Ni, and Au with thicknesses of 5, 55, and 30 nm, respectively, and the electrode width is 200 nm. The metal pattern was transferred to the substrate via a lift-off process. The channel length, *i.e.*, the distance between the two electrodes, is approximately 4 µm.

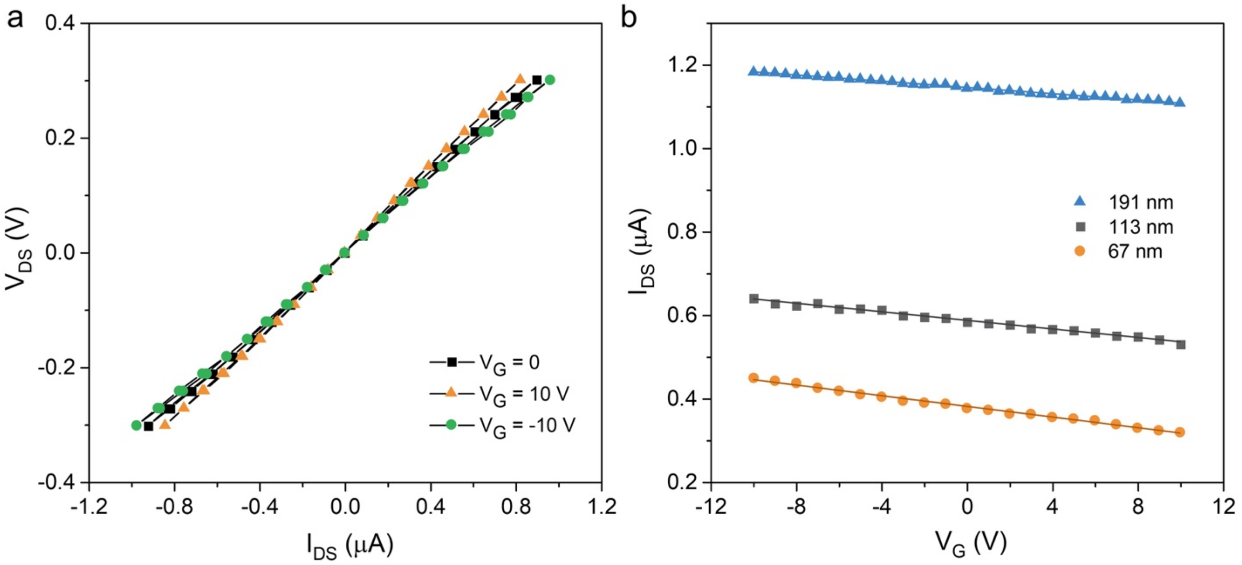

Figure 4.15- Gate modulated electrical conductivity measurements. (a) Drain source current (I_{DS}) versus drain source voltage (V_{DS}) under different gate voltage V_g, the linear I-V curve showing Ohmic behaviors of the contacts. (b) Measured source drain current of three Te-PEDOT:PSS core/shell nanowires as a function of gate voltage, where the drain source voltage is kept at 0.2 V.

As shown in **Figure 4.15a**, the *I-V* curves of the nanowire under various gate voltages are linear, suggesting Ohmic contact between the nanowire and the metal electrodes. It also shows that the conductance of the nanowire decreases as the gate voltage increases, indicating p-type behavior.

Based on the calculated transconductance g_m from the measured I_{DS}-V_G data (**Figure 4.15b**), we are able to extract the hole mobility as $\mu = (g_m L^2)/(V_{DS}C)$, where L is nanowire length, and C is the capacitance of the gate oxide, which is described as[154]:

$$\frac{C}{L} = \frac{2\pi\varepsilon_0\varepsilon_r}{\cosh^{-1}\left(\left(R+h\right)/R\right)}, \tag{4.16}$$

Where h is gate oxide thickness, R is the nanowire radius, ε_0 is the vacuum permittivity, and ε_r is the relative dielectric constant of the gate oxide. Here, an empirical value of $\varepsilon_r = 2.2$ is used, which has been shown to fit very well with the finite element analysis of the gate according to Moon *et al.*.[154] This accounts for the actual model where the bottom of the nanowire is silicon oxide ($\varepsilon_r = 4$) and the surrounding/top of the nanowire is air ($\varepsilon_r = 1$).

4.7.8 Gate Modulated Seebeck Coefficient Measurements

In order to measure the Seebeck coefficient, a controlled temperature gradient must be applied across a material. To do this, we deposited a metal heater on top of the two electrodes, which produces a power output due to Joule heating, and the two metal electrodes also serve as thermometers to measure local temperature variations. As the resistance of a metal is linearly proportional to temperature, by carefully measuring the resistance of the metal electrode the temperature can be attained. **Figure 4.16** shows the schematic drawing of the 10 probe device used to measure local temperature variations. The 2-probe electrode near the top is the heater electrode, while the two 4-probe electrodes are used as thermometers.

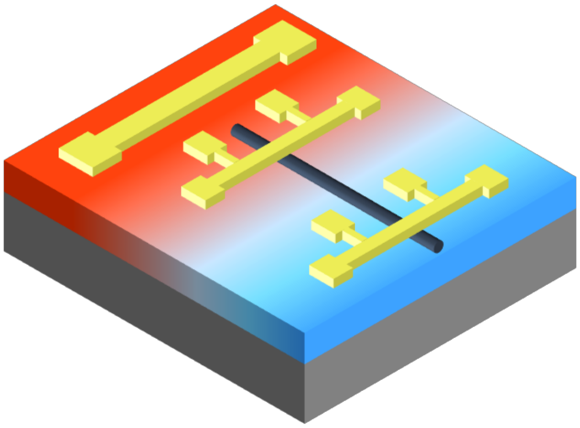

Figure 4.16- Schematic drawing showing the device setup used for gated modulated Seebeck coefficient measurements.

To obtain the temperature coefficient of resistance (TCR) for each resistive thermometer probe, we first measured the electrical resistance of each thermometer without heating voltage at different global temperatures inside the cryostat. Before Seebeck measurements, we need to carefully characterize the thermometers to obtain the local temperature information. To do this, shown as circuit diagram in **Figure 4.17a**, we applied an equivalent of an AC bridge method, following the procedures of Zuev *et al.*.[153] The 4-probe geometry is used in order to eliminate the resistance of the leads and only measure the resistance of the small length of the thermometer line near the heater. Two lock-in amplifiers (Stanford Research Systems, SR830) are used to increase the signal-to-noise ratio, and the resistance measurement is performed simultaneously with two lock-ins in order to improve reproducibility. We use the “Offset” and “Expand” functions on the lock-in amplifier in order to digitally enhance the small changes in resistance produced by the temperature gradient. **Figure 4.17b** shows a typical measured lock-in voltage versus heater voltage curves. The change in resistance is proportional to the change in temperature which in turn is proportional to the power $P = V^2_{heater}/R$ produced in the heater electrode. Since $R_{thermometer} \propto V^2_{heater}$, we fit the curves with second order polynomials, and the temperature of each probe is calculated based on the fitted resistance and calculated TCR.

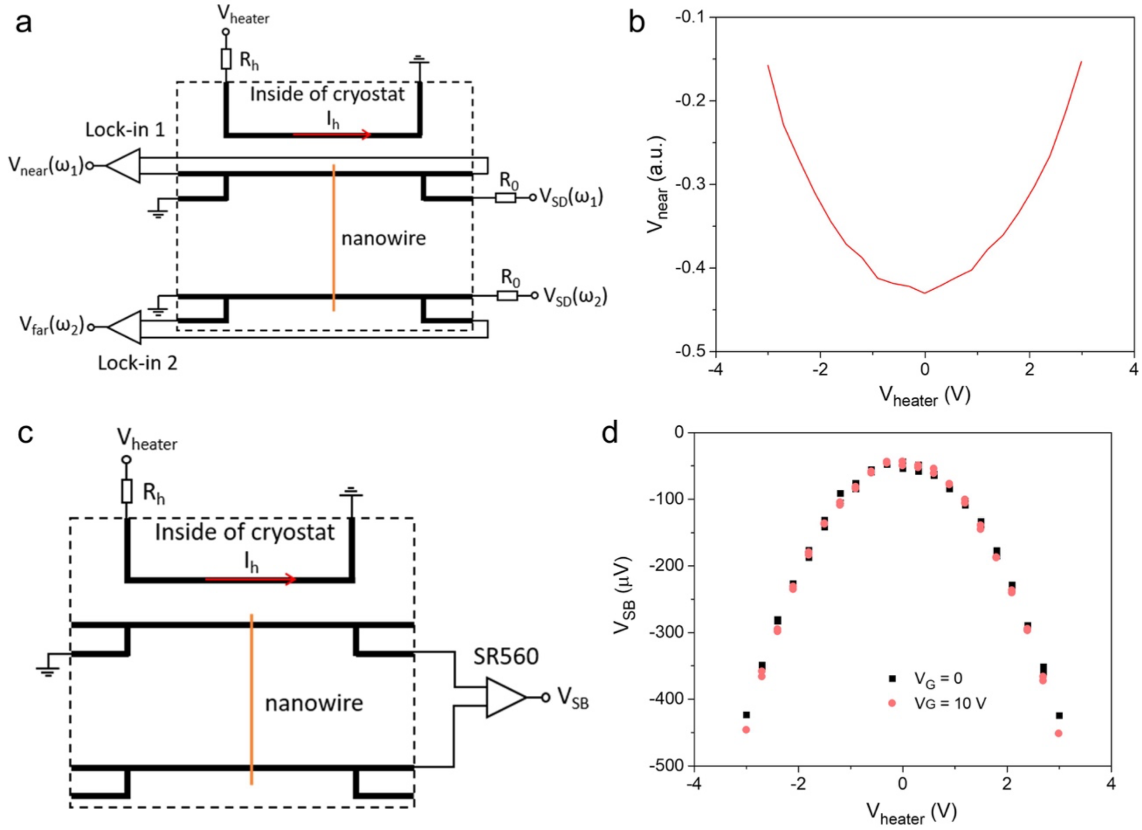

Figure 4.17- Gate modulated Seebeck coefficient measurements. (a) Circuit diagram showing the measurement scheme for the thermometer calibration. (b) Measured voltage with lock-in 1 for the near side thermometer plotted as a function of heating voltage. (c) Circuit diagram showing the measurement scheme for the Seebeck coefficient measurement. (d) Measured Seebeck voltage plotted as a function of heating voltage under different global back gate voltage.

Figure 4.17c shows the approach we used to measure the thermally induced voltage across the nanowire, and the thermometer electrodes are used as voltage probes. During the measurement, the heater voltage is swept the same way as in the calibration measurement. A DC voltage amplifier (SR560) is used to measure the Seebeck voltage, V_{SB}, across the nanowire. **Figure 4.17d** shows a typical V_{SB} curve plotted against V_{heater}, and the down-ward parabolic shape indicates the p-type behavior. We obtained the thermoelectric voltage by taking the difference of the highest and lowest point through second order fit, and Seebeck coefficient is calculated using $S = -\Delta V/\Delta T$. Then, through changing the global back gate voltage, V_G, the carrier density and therefore the Fermi energy in the nanowire can be changed, and we are able to measure S as a function of V_G. Shown as in **Figure 4.18**, the measured Seebeck coefficient increases as the gate voltage increases, which is a result of p-type behavior.[154]

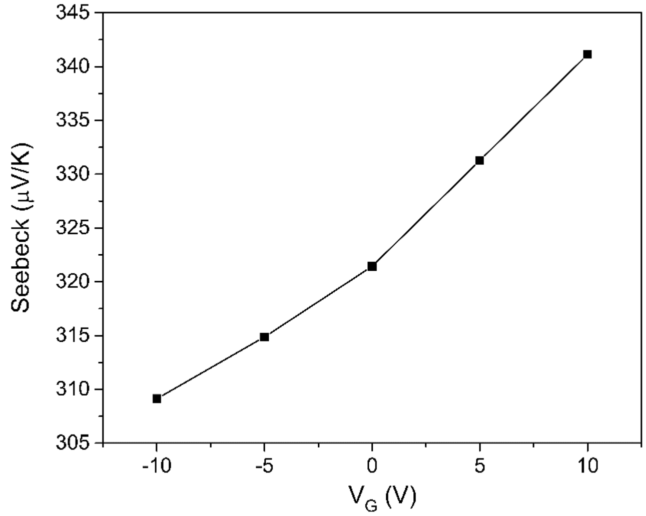

Figure 4.18- Seebeck coefficient of Te-PEDOT:PSS nanowire measured under different gate voltage.

4.7.9 Lattice Thermal Conductivity Modelling Considering Boundary Scattering Effects

In order to confirm that phonon-boundary scattering dominates thermal transport in Te-PEDOT:PSS hybrid nanowires, we calculated lattice thermal conductivity along the axial direction of the nanowire based on the Callaway-Holland model,[98,165] which can be expressed as:

$$\kappa = \frac{1}{6\pi^2}\sum_j \int_q \frac{\hbar^2\omega_j^2(q)}{k_B T^2} \frac{\exp(\frac{\hbar\omega_j(q)}{k_B T})}{(\exp(\frac{\hbar\omega_j(q)}{k_B T})-1)^2} \upsilon_j(q)^2 \tau_j(q,T) q^2 dq, \tag{4.17}$$

where $\hbar$ is the reduced Plank constant, k_B is the Boltzmann constant, T is temperature, and $v_j(q) = \partial\omega_j/\partial q$ is the phonon group velocity. $\omega(q)$ is phonon frequency, and a 4th order polynomial fitting to the full dispersion relation along Γ-A direction of bulk Te was adopted.[98] The summation is over all different acoustic phonon modes j. First-principles calculations have shown that phonon-phonon scattering is the dominant scattering mechanism in Te and electron-phonon scattering is not important.[98] Thus, we assume the phonon scattering lifetime τ is dominated by Umklapp, defects, and boundary scattering, which are determined as $\tau_{j,Umklapp}^{-1} = BT\omega_j(q)^2 \exp(-C/T)$, $\tau_{j,defects}^{-1} = D\omega_j(q)^4$, and $\tau_{j,boundary}^{-1} = v_j(q)/E$, respectively. The total relaxation time is calculated using the Matthiessen's rule as follows: $\tau_{j,bulk}^{-1} = \tau_{j,Umklapp}^{-1} + \tau_{j,defects}^{-1} + \tau_{j,boundary}^{-1}$.

The fitting parameters B, C, and D are obtained through fitting the measured temperature dependent thermal conductivity of the largest nanowire sample tested in this work (186 nm diameter), and E is the nanowire diameter. As shown in Fig. 5a in the main paper, the best fitting is obtained with the following parameters: $B = 4.52 \times 10^{-18}$ s K^{-1}, $C = 120$ K, and $D = 3.5 \times 10^{-43}$ s^3. The fitted defect scattering coefficient is close to that of $NbSe_3$ nanowires,[141] which are also van der Waals materials. The high phonon-phonon scattering coefficient (4.52×10^{-18} s K^{-1}) could be explained due to the high degree of lattice anharmonicity in Te,[98] similar to other van der Waals materials.[141] Shown as in **Figure 4.19a**, the modeled thermal conductivity shows good agreements for the other five nanowires by fixing all of the rest of scattering parameters while varying only the wire diameter, which suggests that phonon-boundary scattering is the dominant scattering mechanism suppressing the thermal conductivity of the hybrid nanowires as the diameter reduces.

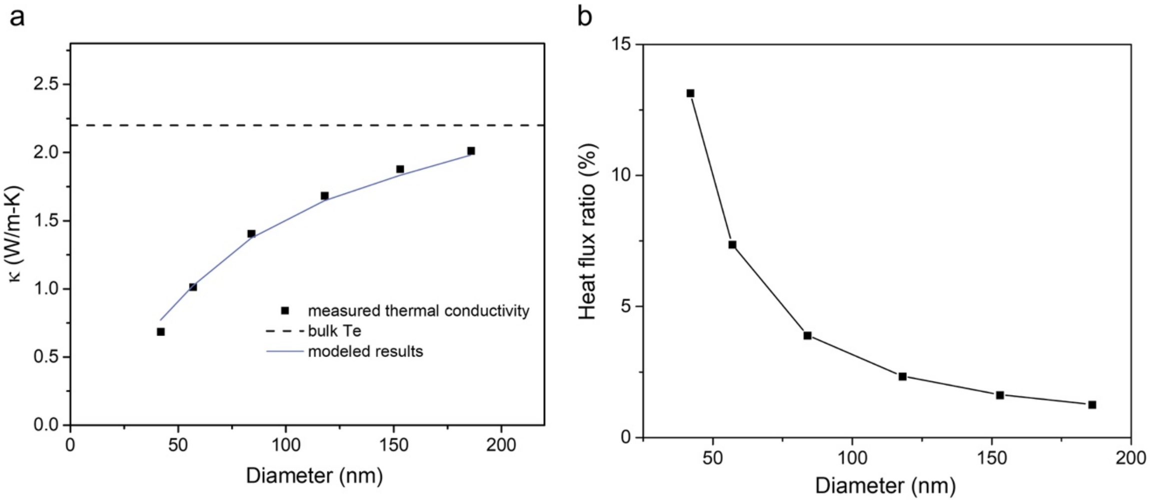

Figure 4.19- Thermal transport in hybrid nanowires. (a) Comparison of the room temperature modeled thermal conductivity with the measured results for Te-PEDOT:PSS hybrid nanowires of different diameters. (b) Calculated heat flux ratio flowing through the shell to that of the total core/shell nanowire as function of wire diameter.

To confirm the negligible role of thin polymer shell on thermal transport, we can calculate the ratio of heat flux flowing through the shell to the total heat flux at a given temperature gradient. Based on the measured κ of semi-crystalline PEDOT:PSS[164] and shell thickness, we can estimate the thermal resistance of the polymer shell R_{shell} with different core diameters. Meanwhile, the thermal resistance of the inorganic core R_{core} can be extracted from the measure hybrid nanowire thermal conductivity and core dimensions using the parallel resistance model. From this, we are able to estimate the ratio of heat flux flowing through the shell and core, which can be calculated as $r = \frac{\Delta T}{R_{shell}} / \frac{\Delta T}{R_{core}} = \frac{R_{core}}{R_{shell}}$, and the heat flux flowing through the shell with respect to the total heat flux is $r/(1+r)$. As shown in **Figure 4.19b**, the thin organic shell is calculated to contribute less than 13% to total thermal transport across all nanowires measured in this work.

Chapter 5. Control over morphology and doping mechanism in Poly(alkyl-chalcogeneophenes) via heteroatom substitution

Reproduced from "Microstructure and heteroatom dictate doping mechanism and thermoelectric properties of poly(alkyl-chalcogenophenes)," Madeleine P. Gordon,† Shawn A. Gregory,† Jamie P. Wooding, Shuyang Ye, Gregory M. Su, Dwight Seferos, Mark D. Losego, Jeffrey J. Urban,* Shannon Yee,* and Akanksha K. Menon*, *Applied Physics Letters,* 2021, 118, 23. (DOI: 10.1063/5.0052604) with permission of the co-authors and AIP Publishing. † Denotes equal contribution.

5.1 Abstract

Heteroatom substitution is one promising way to favorably alter electronic transport in conductive polymers to improve their performance in thermoelectric devices. This study reports the spectroscopic, structural, and thermoelectric properties of poly(3-(3',7'-dimethyloctyl) chalcogenophenes) (P3RX) doped with 2,3,5,6-tetrafluoro-7,7,8,8-tetracyanoquinodimethane (F4TCNQ), where the doping methodology, the heteroatom (X = Thiophene (T), Selenophene (Se), Tellurophene (Te)) and the extent of doping are systematically varied. Spectroscopic measurements reveal that while all P3RX polymers are appreciably doped, the doping mechanism is inherently different between the polymers. Poly(3-hexylthiophene) (P3HT, used in this study as a control) and P3RTe doped primarily via integer charge transfer (ICT), whereas P3RSe and P3RT appear to be doped via charge-transfer complex (CTC) mechanisms. Despite these differences, all polymers saturate with roughly the same number of F4TCNQ counterions (1 dopant per 4 to 6 heterocycles), reinforcing the idea that the extent of charge transfer from polymer to dopant varies significantly on the preferred doping mechanism. Grazing incidence wide-angle X-ray scattering measurements provide insight into the structural driving forces behind these different doping mechanisms - P3RT and P3RSe have similar microstructures in which F4TCNQ intercalates between the π-stacked backbones resulting in CTC doping (localized charge carriers), while P3HT and P3RTe have microstructures in which F4TCNQ intercalates in the alkyl-side chain region, giving rise to ICT doping (delocalized charge carriers). These structural and spectroscopic observations shed light on why P3HT and P3RTe obtain maximum electrical conductivities *ca*. 3 S/cm, while P3RT and P3RSe obtain maximum electrical conductivities $<10^{-3}$ S/cm under the same thin film processing conditions. Ultimately, this work quantifies the effects of heteroatom, microstructural ordering, extent of doping, and doping mechanism on optical and electronic properties and provides rational guidance for designing future polymer and dopant chemistries for high performance thermoelectric materials.

5.2 Introduction

Semiconducting polymers are an attractive class of materials for optical and electronic devices where processability and mechanical flexibility are desired.[168–170] Integration of these polymers into thermoelectric devices, used for energy harvesting and/or localized heating and cooling, has risen in popularity over the last decade.[1,169,171] P3HT (poly(3-hexylthiophene)) is a promising, well-studied p-type organic semiconducting polymer, but its electrical conductivity (σ) and

Seebeck coefficient (S) fall short of conventional inorganic materials, thereby limiting P3HT's practical use in thermoelectric devices. One avenue for improving electronic performance is through polymer main chain heteroatom substitution; the heteroatom identity can fine-tune the molecular packing and the frontier molecular orbital energies, both of which influence charge transport properties.[172–175] In a previous study, we demonstrated that substituting the heteroatom in poly(alkyl-chalcogenophenes) from S to Se to Te results in smaller optical band gaps and increases the susceptibility to $FeCl_3$ oxidation, *i.e.,* a smaller amount of dopant is needed.[80,176] This in turn yields an optimal thermoelectric power factor ($S^2\sigma$) of *ca.* 13 μW/mK^2 for poly(alkyl-tellurophenes) that achieve appreciable σ and low S values (*ca.* 50 S/cm and 30 μV/K, respectively) that are indicative of high doping levels. This previous work demonstrated that heteroatom substitution can alter doping susceptibility and thermoelectric performance, but fundamental insights into the doping-induced charge transfer mechanisms and resulting structure-property relationships for this class of poly(alkyl-chalcogenophenes) remain unexplored.

Chemical doping involves oxidizing or reducing the polymer main chain, thus altering the density and filling of electronic states. Additionally, dopant geometry,[83] dopant intercalation in the polymer microstructure,[177,178] and the alignment of polymer and dopant frontier molecular orbital energies[179,180] must also be considered when engineering a polymer/dopant system.[105] While $FeCl_3$ is commonly used for oxidative doping, its relatively small molecular size (~3-6 Å) can make it challenging to track the dopant position and interactions with the semiconducting polymer.[179] On the other hand, the molecular oxidant F4TCNQ (2,3,5,6-tetrafluoro-tetracyanoquinodimethane) is suitable for quantifying doping mechanisms and establishing structure-doping relationships as its larger molecular size causes a greater disruption to the polymer's microstructure. Additionally, F4TCNQ has been shown to be an effective dopant for enhancing thermoelectric performance in a variety of ways,[181] including charge transfer complexation (CTC),[177] integer charge transfer (ICT),[182–184] and/or double doping[185] depending on the polymer microstructure, energy levels, and processing conditions. CTC involves the formation of new local hybridized molecular orbitals with a partial, non-integer charge transfer from the polymer to the dopant.[177] In contrast, ICT involves the transfer of an integer of charge (*e.g.* $1e$ or $2e$ transfer)[177] and leads to more electrically conductive materials as the polaronic carriers are not localized in a hybridized orbital between the polymer and dopant.[182] By engineering F4TCNQ to dope P3HT primarily through the ICT pathway and intercalate among the hexyl side chains, solution doping studies have reported electrical conductivities of 1-10 S/cm,[186–188] vapor doped conductivity of 1-100 S/cm,[189] and high-temperature rubbing-induced conductivities of >100 S/cm.[181] Unlike P3HT, its branched side chain analog P3EHT (poly(3-(2'-ethyl)hexylthiophene)), is doped by F4TCNQ through a CTC pathway with dopant molecules intercalating between the π-stacks, which leads to a low electrical conductivity of 10^{-3} S/cm.[177] Despite having the same conjugated backbone as P3HT, this P3EHT study demonstrated that microstructural ordering significantly influences the doping mechanism and resulting optical and electronic properties.

Herein, we investigate the effects of heteroatom substitution, doping method, and dopant concentration on the resulting thermoelectric and charge transport properties of a series of poly(3-(3',7'-dimethyloctyl) chalcogenophenes), where the chalcogen is either S, Se, or Te (P3RT, P3RSe, P3RTe, respectively). Through optical, infrared and photoelectron spectroscopies, we find that F4TCNQ dopes P3RT primarily via CTC, P3RSe via both CTC and ICT, and P3RTe primarily via ICT. Experiments with P3HT are also performed and confirm that the doping and processing procedures are comparable to prior literature reports. Grazing incidence wide-angle x-ray scattering (GIWAXS) sheds light on the underlying cause for these different doping mechanisms. P3RT and P3RSe have similar structural ordering where F4TCNQ intercalates between the π-stacks, leading to primarily localized, CTC based doping. In contrast, P3RTe and P3HT have similar microstructural ordering with F4TCNQ primarily intercalating into the lamellar side chain region, resulting in more delocalized, ICT based doping. Thermoelectric measurements reveal the performance impacts of the different doping mechanisms; CTC dominated P3RT and P3RSe have low carrier mobilities and electrical conductivities ($\sigma < 10^{-2}$S/cm), whereas ICT dominated P3RTe and P3HT have considerably higher carrier mobilities and electrical conductivities ($\sigma \approx$ 3 S/cm) upon doping with F4TCNQ via both solution and vapor doping methods.

5.3 Results and Discussion

Thin films (*ca.* 300 nm) of each polymer were spin coated from toluene solutions. These films were either solution-doped with varying F4TCNQ molarities in acetonitrile or vapor-doped by subliming F4TCNQ for 60-minutes. Detailed experimental procedures and polymer characterization can be found in Section 5.5 , and in our prior study.[80]

UV-Visible-Near Infrared (UV-Vis-NIR) spectroscopy is used to provide cursory evidence for the extent of doping and the mechanism as a function of dopant concentration and heteroatom. **Figure 5.1** plots the UV-Vis-NIR spectra for polymer thin films on glass substrates in their pristine, solution doped (50 mM), and vapor doped forms. In each panel of **Figure 5.1**, black lines show the pristine spectra, and the pink and blue lines represent the vapor and 50 mM solution doped films, respectively. An in-depth analysis of the UV-Vis-NIR spectra shown in **Figure 5.1** is provided in the supporting information (Section 5.7.1).

Figure 5.1 provides qualitative insight into the extent of doping; as the intensity of the pristine polymer π-π^* peak between 500-700 nm decreases, the extent of doping increases. For both the solution and vapor doped scenarios, P3RT is least susceptible to F4TCNQ doping (**Figure 5.1a**) and P3RSe demonstrates a stronger degree of doping (*i.e.,* greater π-π^* bleaching, **Figure 5.1b**). P3RTe (**Figure 5.1c**) shows the highest degree of F4TCNQ doping, and the optical features at 410 nm, 760 nm and 875 nm are indicative of ICT being the predominant doping mechanism at play.[182,190–192] While P3RSe also demonstrates these ICT features, peaks at 364 nm and 685 nm suggest the presence of CTC doping as well (**Figure 5.1b**). [182,190–192] In contrast, P3RT demonstrates predominantly CTC doping peaks (**Figure 5.1a**). To facilitate direct comparisons with prior literature, measurements were also made on P3HT films (**Figure 5.1d**), which demonstrate strong ICT features at 410 nm, 760 nm and 875 nm and a fair degree of F4TCNQ doping susceptibility, like P3RTe. Note that in all three P3RX films and P3HT films, there is little variation in the optical spectra of solution doped and vapor doped films, which suggests that the extent of doping is comparable with both methods.

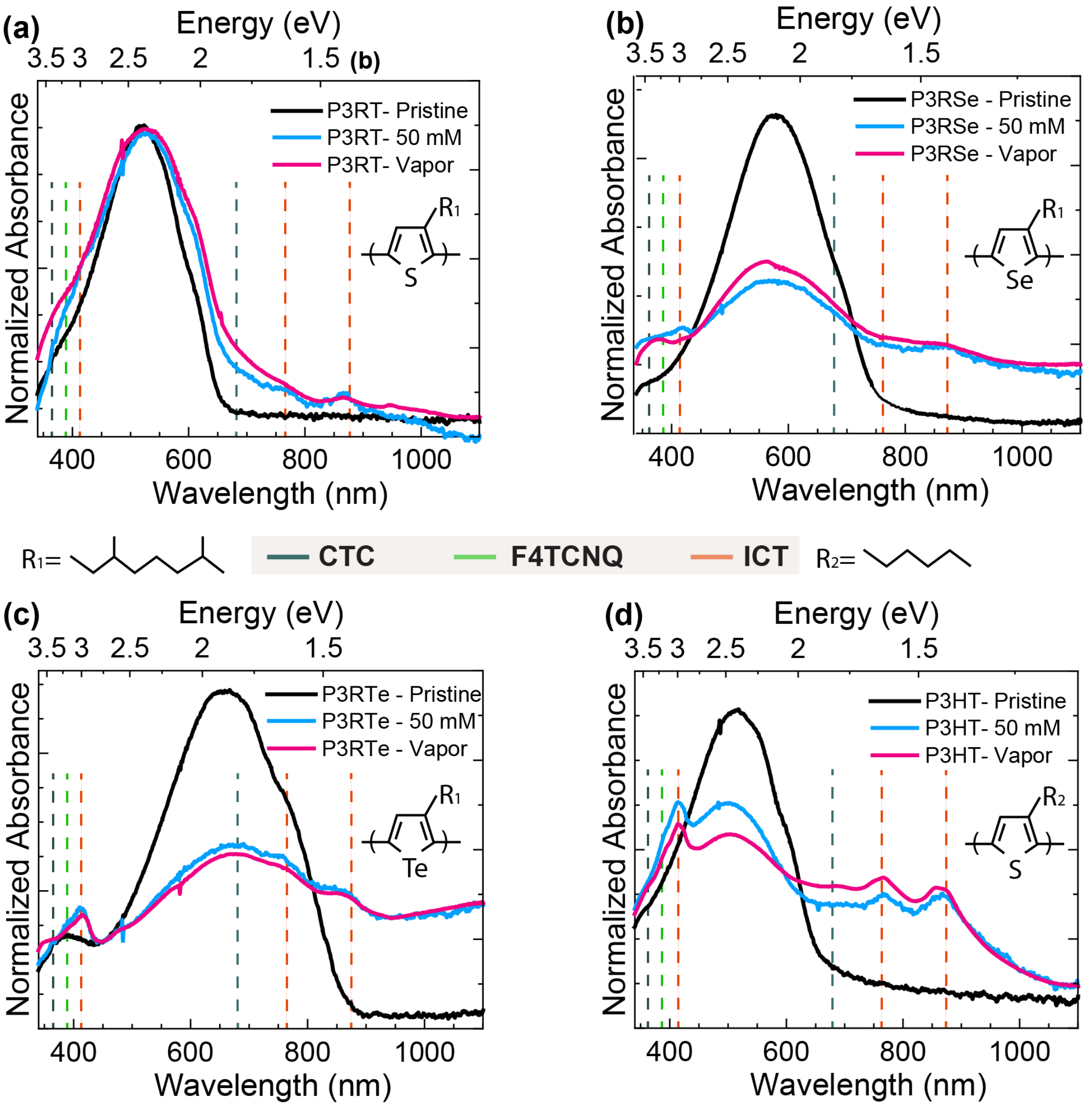

Figure 5.1- Normalized UV-Vis-NIR spectra of the pristine polymers, and the F4TCNQ solution doped (50 mM) and vapor doped films, (a) P3RT, (b) P3RSe, (c) P3RTe, and (d) P3HT. The dashed lines in each panel show the peak locations of CTC (teal lines *ca.* 364, 685 nm), residual F4TCNQ dopant (green lines *ca.* 390 nm) and ICT (orange lines *ca.* 410, 760, 875 nm).

To corroborate these optical trends, attenuated total reflection Fourier-transform infrared spectroscopy (ATR-FTIR) was performed on these films. ATR-FTIR measurements can provide insights into the extent of doping (*via* polaronic absorbance in the mid-IR), degree of charge carrier delocalization (broad optical absorbance ranging from *ca.* 1500 cm^{-1} to over 5000 cm^{-1}) and the doping mechanism (*via* changes in the C≡N stretching mode absorbance near 2200 cm^{-1}). For the sake of brevity, full discussion on this technique is provided in Section 5.7.2. These measurements reveal that P3RTe and P3HT demonstrate strong peak intensities at 2194 cm^{-1} correlated with ICT, while P3RT has peak intensities between 2200-2015 cm^{-1} linked to CTC features, and P3RSe has intensities associated with both ICT and CTC absorption features. Overall, these ATR-FTIR results are consistent with the doping mechanisms elucidated by UV-Vis-NIR.

These optical and infrared spectroscopic measurements provide qualitative insight into the charge transfer mechanism but fail to quantify the extent of doping in the P3RX films and the relative contribution of each doping mechanism at play. To this end, X-ray photoelectron spectroscopy (XPS) surface profiling was used. **Figure 5.2a-d** shows the heteroatom spectra (S-2p, Se-3d, Te-3d) for the pristine polymer films, 50 mM solution doped films, and vapor doped films; additional XPS spectra are in Section 5.7.3. To provide insight into the dopant-polymer interactions, deconvoluted N-1s spectra for 50 mM doped films are shown in **Figure 5.2e**.

Upon doping there is a clear shift to higher binding energies, which is indicative of a loss in electron density with the introduction of dopant in **Figure 5.2a-d**. XPS heteroatom spectra confirm that vapor doping and 50 mM solution doping yield similar results based upon their analogous shifts in binding energy. In-depth discussion of heteroatom peak positions and their deconvolutions can be found in Section 5.7.3. In order to quantify the extent of doping, the atomic abundance for F and N with respect to the heteroatom (S, Se, Te) was used. We examine here the solution doped films due to the better stability of the dopant molecule under vacuum, leading to less background noise. We find that the dopant to heterocycle ratio for 50 mM doped P3RT is 19 ± 3 %, P3RSe is 19 ± 2 %, P3RTe is 23 ± 8 %, and P3HT is 18 ± 4 % (Section 5.7.3). These results suggest that each P3RX polymer has roughly equal amounts of F4TCNQ present at the film's surface (*ca.* 1 dopant per 5 rings), which is consistent with previous P3HT-F4TCNQ reports.[30,31] Inspection of the N-1s spectra shown in **Figure 5.2e** provides additional insight as Watts *et al.* studied ICT and CTC in P3HT doped with F4TCNQ and assigned the N^{-1} peak at 398.2 eV to ITC and the N^0 peak at 400 eV to CTC.[182] The motivation behind these assigned differences in binding energy arises from the electron density differences in F4TCNQ for these two doping mechanisms. ICT involves a full electron transfer to the F4TCNQ molecule, resulting in a higher electron density and thus a shift to lower binding energies, whereas CTC appears at higher binding energies.

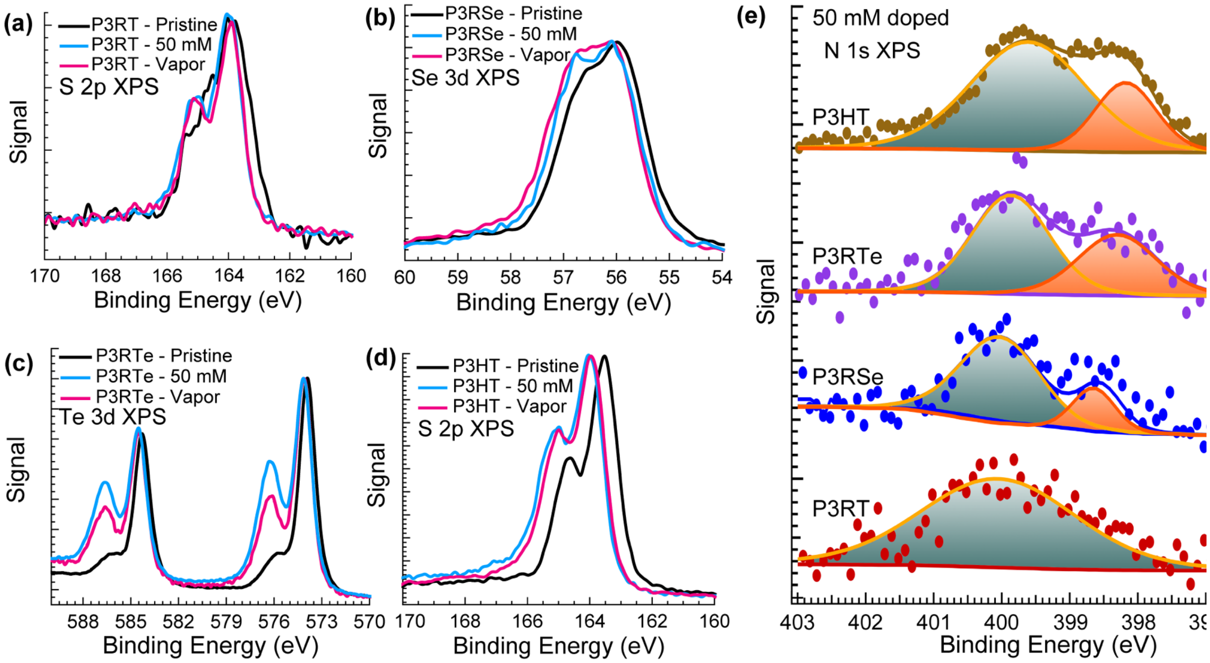

Figure 5.2- XPS analysis for select P3RX films. Heteroatom scans for each polymer (a) S-2p spectra in P3RT, (b) Se-3d spectra in P3RSe, (c) Te-3d spectra in P3RTe, and (d) S-2p spectra in P3HT, all demonstrate a blue shift upon doping. (e) Deconvoluted N-1s spectra of 50 mM doped polymers reveal the relative intensities of N^0 species (teal fitted peak centered at ~399.5 eV) versus the N^{-1} peak (orange fitted peak centered at ~ 398 eV). The strong presence of N^{-1} in both P3RTe and P3HT further corroborates that ICT is the dominant doping mechanism for these two polymers, as opposed to P3RT and P3RSe which show reduced or no intensity.

Deconvolution of the N-1s spectra reveals the presence of both the N^0 and N^{-1} peaks in all systems except P3RT, which demonstrates just a broad N^0 peak at ~ 399.5 eV. From the fitting of these N-1s spectra, peak area ratios were calculated to determine the relative percentage of ICT doping occurring in P3RSe, P3RTe and P3HT, which all show N^{-1} features.[193] P3RSe demonstrates a relatively low N^{-1} percentage of ~18%, further supporting the UV-VIS and FTIR measurements that ICT is not the dominant mode of charge transfer, but it is present to some extent. On the other hand, P3RTe and P3HT both demonstrate strong N^{-1} peak percentages of ~35%, suggesting that ICT is a major charge transfer mechanism at play.

Spectroscopic measurements show that the extent of doping and the mechanism vary significantly within the P3RX family, but these measurements alone do not explain why P3RT and P3RSe have significant CTC populations while P3RTe dopes primarily through ICT. Previous studies have shown that propensity for CTC or ICT doping is dependent on the method of intercalation of F4TCNQ into the polymer crystallite; specifically, CTC doping occurs as F4TCNQ resides between the crystallites' π-stacks and forms localized, hybridized polymer-F4TNCQ molecular orbitals.[177] Therefore, to probe the structural morphology of these polymers and understand the impacts of doping with F4TCNQ, grazing incidence wide angle X-ray scattering (GIWAXS) was performed on the pristine polymers and their F4TCNQ vapor-doped analogs. Vapor doped films were chosen because it has been demonstrated that this maintains higher degrees of structural ordering compared to solution doped films, and we observe comparable spectroscopic properties with both types of doping.[189,194]

A brief discussion of the pristine GIWAXS scattering shown in **Figure 5.3a-c** can be found in Section 5.7.4. Upon doping with F4TCNQ in the vapor phase, a clear change in the scattering pattern occurs for all the polymers (**Figure 5.3d-f**). Both P3RT and P3RSe demonstrate a contraction in lamellar lattice spacing (h00 peaks shift to higher Q), whereas P3HT and P3RTe show an expansion of the lamellar lattice (h00 peaks shift to lower Q). Focus was placed on the (100) peaks due to its strong scattering intensity. Furthermore, several studies have shown that changes in the lamellar lattice spacing can be indicative of the doping mechanism. Stanfield *et al.* demonstrated that a poor doping solvent leads to a contraction of P3HT lamellar lattice spacing, suggesting that F4TCNQ molecules coordinate within the π–π stacking region along the polymer backbone leading to CTC doping.[195] Thomas *et al.* observed a similar effect in P3HT *vs*. P3EHT, where the branched alkyl sidechains in P3EHT create steric hindrance that inhibits F4TCNQ intercalation into the polymer side chains and promotes F4TCNQ intercalation between the π-stacks, and this was accompanied by a slight decrease of the alkyl stacking distance.[177] Therefore, we postulate that P3RT and P3RSe are doped via a CTC mechanism, evidenced by the contraction in alkyl stacking distance (shift in the alkyl stacking peak to higher Q) from 22.6 nm to 19.7 nm for P3RT, and 22.4 nm to 21.5 nm for P3RSe. This suggests the dopant inserts co-facially between polymer backbones. Interestingly, while P3RTe has the same branched side chain as its thio- and seleno- counterparts, it shows a lamellar lattice expansion similar to P3HT, from 18.9 nm to 20.4 nm. This suggests that F4TCNQ intercalates in P3RTe's lamellar side chains and allows for ICT doping. There are many factors, such as crystallite size, differences in electronic interactions, etc., that could be causing these observed differences. However, we hypothesize that P3RTe's unique behavior could, in part, be due to differences in the P3RX polymers' degree of backbone rotational freedom. Ye *et al.* performed an in-depth study on the forces at work to drive crystallization in these polymers and found that as the substituted heteroatom becomes larger, there is less rotational freedom.[196] Thus, as the heteroatom becomes larger and the polymer backbone becomes more conformationally-locked in a planar configuration, the chains can come closer to one another to enable better molecular overlap which ultimately translates to higher mobility. The lower degree of backbone rotational freedom in P3RTe may hinder F4TCNQ intercalation between the π-stacks and as a result, the dopant molecules intercalate into the alkyl side chains and participate in ITC doping. In contrast, higher degrees of backbone rotational freedom in P3RSe and P3RT (while still having a sterically hindered branched alkyl side chain) translates to F4TCNQ molecules intercalating between π-stacks and participating in CTC doping, which is consistent with the spectroscopic results presented herein.

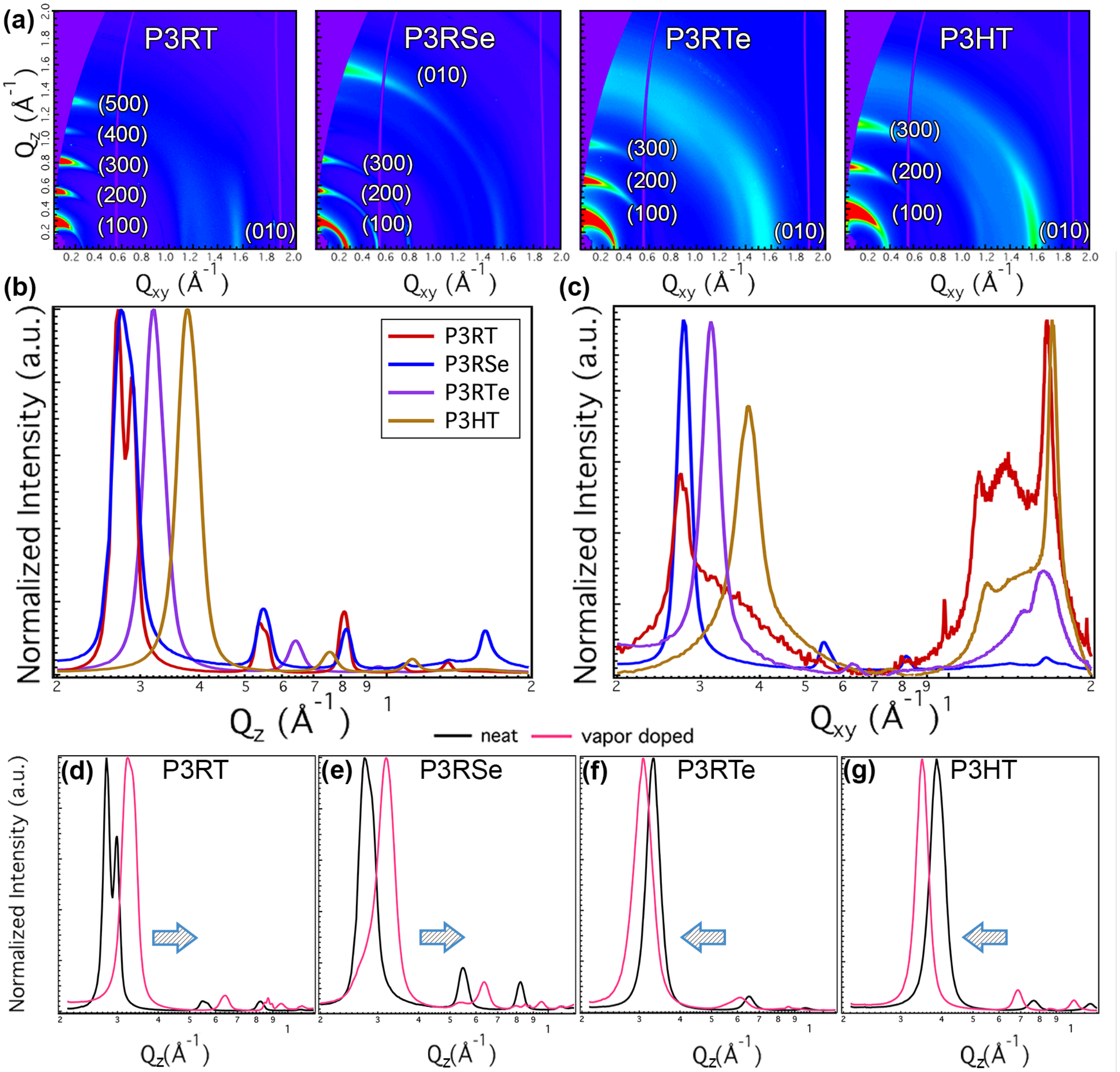

Figure 5.3- (a) GIWAXS of pristine polymers of P3RT, P3RSe, P3RTe and P3HT, (b) nearly out-of-plane line cut, and (c) in-plane line cuts. The strong (h00) peaks visible in (b) along with the pronounced (010) peaks in (c) provide clear support of preference for edge-on orientation for all the polymers except P3RSe which shows both edge-on and face-on alignment. Out-of-plane line cuts are shown for (d) P3RT, (e) P3RSe, (f) P3RTe, and (g) P3HT both before and after vapor doping with F4TCNQ. Both P3RT and P3RSe show (h00) peaks shift to higher Q after doping, indicative of a contraction of the lamellar spacing. P3RTe and P3HT show the lamellar stacking peak shift to lower Q, indicating an expansion in lamellar spacing and suggestive of F4TCNQ dopant intercalating into the alkyl side chains leading to ITC doping.

The electrical conductivity and Seebeck coefficient are a measure of the macroscopic average charge carrier density, charge carrier mobility and how these properties vary as a function of polymer chemistry and extent of doping. The P3RX family has appreciable thermoelectric properties when doped with $FeCl_3$,[80] and spectroscopic data suggests that F4TCNQ dopes all P3RX polymers and P3HT, albeit through various mechanisms. Here, these thermoelectric measurements are used to quantitatively understand to what extent ICT *vs.* CTC doping mechanisms affect the resulting charge transport.

Figure 5.4a plots the electrical conductivity (σ) for both the solution and vapor doped films. Although P3RT has an appreciable number of F4TCNQ dopant counterions (**Figure 5.2**), the number of charge carriers with sufficient mobilities is limited due to its CTC doping mechanism,[177,182] leading to a very low electrical conductivity ($\sigma < 10^{-4}$ S/cm). Similarly, P3RSe shows low electrical conductivities of $< 5\times10^{-3}$ S/cm, likely due to the dopant being incorporated between the π-stacks (**Figure 5.3**) resulting in a significant CTC population (**Figure 5.2**) with heavily localized charge carriers. The latter is supported by temperature dependent conductivity measurements, which show a large activation energy (150-200 meV), in comparison to other highly doped semiconducting polymers (<100 meV), (Section 5.7.5). In contrast to P3RT and P3RSe, P3RTe shows appreciable electrical conductivity at all doping concentrations in this study, with a maximum of 2.6 ± 1.1 S/cm at 25 mM F4TCNQ and with vapor doping. This is three orders of magnitude higher than P3RSe at the same doping molarity and XPS counterion concentration (**Figure 5.2**), owing to P3RTe being doped primarily via ITC. At a higher solution molarities of 50 mM, the electrical conductivity of P3RTe decreases, likely due to over doping, which has been reported in several polymer dopant systems.[80,82,83,197] The maximum P3RTe electrical conductivity is roughly equal to the maximum P3HT electrical conductivity of 3.2 ± 0.4 S/cm. Lastly, we note that the solution doped and vapor doped maximum electrical conductivities for P3HT and P3RTe are comparable to one another and are similar to the electrical conductivity of P3HT doped with F4TCNQ reported in previous literature.[188,194]

Now we turn to analyze the Seebeck coefficient in **Figure 5.4b**. The Seebeck coefficient (S) is directly related to the asymmetry of the carrier distribution about the Fermi energy. Thus, S usually decreases as a result of reduced asymmetry as carrier concentration increases. Doped P3RT and P3RSe films were too insulating for repeatable Seebeck coefficients to be reported, while both P3RTe and P3HT show observable Seebeck coefficients. As expected, the Seebeck coefficient decreases as the doping concentration increases for both P3RTe and P3HT; further discussion can be found in Section 5.7.5. This trend agrees with the measured increasing electrical conductivity and increasing charge carrier concentration, as well as previous literature reports.

Lastly, we examine the S-σ plot for the P3RX polymers doped with $FeCl_3$ and F4TCNQ (**Figure 5.4c**). The curvature, slope, and nominal values on the S-σ plot are indicative of fundamental transport phenomena, so analyzing these curves enables rational polymer and dopant design for optimal thermoelectric performance.[74] Although the values in **Figure 5.4c** do not lead to record-high thermoelectric power factors (maximum of *ca.* 3.8 $\mu W/mK^2$ for the P3RTe-F4TCNQ films), it is notable that all P3RX-$FeCl_3$ and P3RTe-F4TCNQ datasets lie on the same curve. According to the Kang-Snyder model, a generalized transport model developed for polymers, materials that lie on the same curve have a similar set of governing transport physics (*e.g.* mobilities, energy dependence, electronic structures).[74] Based on this framework, we find that the heteroatom, dopant concentration, and chemistry are all parameters that shift transport properties along the same S-σ curve, but do not laterally or vertically shift the S-σ curve (as long as the polymers are doped via ICT mechanisms). Therefore, we hypothesize that in addition to using poly(tellurophenes) for their advantageous ordering and doping susceptibility, employing additional orienting methods such as drawing,[198] or rubbing,[181,199] which have been shown to laterally shift the S-σ curve, will likely lead to enhanced thermoelectric performance beyond what is reported in this work.

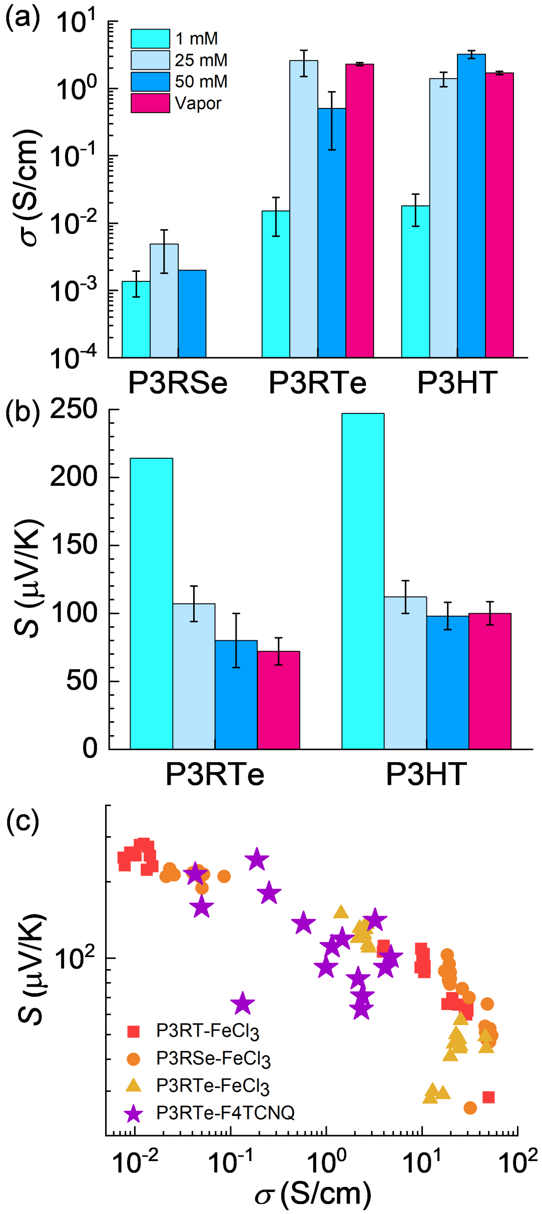

Figure 5.4- Thermoelectric properties as a function of heteroatom and doping. (a) Electrical conductivity, (b) Seebeck coefficient, (c) Jonker curve comparing this study (P3RTe-F4TCNQ) with our previously reported P3RX-$FeCl_3$ dataset. Error bars, when present, represent the sample-to-sample standard deviation.

5.4 Conclusions

In this work, we demonstrated that varying the heteroatom (S, Se, Te) alters the polymer microstructure, doping mechanism, and charge transport properties. Moving from S to Se to Te, the susceptibility to F4TCNQ doping increases. Optical and photoelectron spectroscopies suggest that all P3RX polymers have a comparable number of F4TCNQ counterions, but P3RT is not heavily oxidized and is doped dominantly via CTC mechanisms, P3RSe is more oxidized and is likely doped through both CTC and ICT, and that P3RTe is heavily oxidized and primarily doped through ICT. GIWAXS measurements suggest that P3RT and P3RSe are prone to CTC doping because of their microstructural ordering, resulting in dopant intercalation between π-stacks. In contrast, P3RTe is similar to P3HT (ICT) because of its planar packing that enables dopant intercalation into the lamellar side chains. Lastly, we note that P3RTe/F4TCNQ has similar transport properties to P3RX/$FeCl_3$, suggesting that more sophisticated processing techniques (*e.g.* rubbing, drawing) may be needed to laterally shift the S-σ curve for the P3RX family. The observations herein quantify how polymer and dopant synthetic engineering (heteroatom, side chain, microstructure, dopant chemistry) affect charge transport and provides guidance for future improvement of semiconducting polymers.

5.5 Materials and Methods

5.5.1 Polymer Synthesis

Previous reports on the polymer synthesis and characterization can be found elsewhere.[80] Previously, chlorobenzene and blade coating was used as a casting solvent for the polymers, for this study toluene and spin coating was used.

5.5.2 Film Fabrication

For spectroscopic and thermoelectric measurements, films were deposited on glass substrates.1 cm^2 glass substrates were purchased from TFD Inc. Glass slides were rinsed with toluene and dried with N_2 prior to film deposition. P3RT, P3RSe, and P3RTe polymers were dissolved in toluene at a concentration of 30 mg/mL. Prior to spin coating, P3RT and P3RSe solutions were at room temperature and P3RTe solution was heat to 80°C to improve the film deposition on the glass substrate. Films were spin coated at 1000, 1500, 1250 rpm for 30 seconds with no ramp and from 20µL of solution. Films were then annealed at *ca.* 150°C for 10 minutes. For GIWAXS measurements, 1 cm^2 silicon substrates were used. Silicon substrates had a native thermal oxide layer and were triple rinsed in water, acetone, and isopropanol. Films on silicon substrates were spin coated using a two-step recipe of 1800 rpm, dwell 45, no ramp then 3000 rpm, dwell 10, 2.0 ramp, followed by thermal annealing at 150°C for 10 minutes.

5.5.3 Solution Doping

Sure-seal ACN (Sigma Aldirch, > 99.5% purity) and F4TCNQ (TCI Chemicals, > 98% purity) were used to prepare fresh F4TCNQ/ACN solutions in ambient atmosphere. The 50 mM solution was then serially diluted to the appropriate concentrations (25, 12, 4, 1 mM). To dope the poly(alkyl chalcogenophene) films, 100µL of the dopant solution was dropped onto and spread over the film. The film was then covered with a petri dish (to mitigate ACN evaporation) and permitted to dope for three minutes. After three minutes, excess dopant solution was pipetted off the film. Excess F4TCNQ (that likely did not participate in doping) was removed by submerging the film in excess ACN for approximately 10 seconds. The film was then place on a hot plate at 60°C for one minute to remove excess ACN. Subsequent measurements were then immediately performed to mitigate atmospheric dedoping effects.

5.5.4 Vapor Doping

Thin films on glass substrates were adhered to the underside of a cap of a 20 mL vial. 10-15 mg of F4TCNQ was loaded into a 20 mL glass vial and flushed with N_2. The sealed vial, containing F4TCNQ and film, were then placed on a hot and heated to 210°C for one hour. After one hour, the vial was permitted to cool to room temperature before the film was carefully removed. F4TCNQ deposits on the film surface were carefully removed with cotton swab applicators and compressed nitrogen gas. Spectroscopic and thermoelectric measurements were immediately performed after doping to mitigate atmospheric dedoping effects.

5.5.5 UV-Vis-NIR Measurements

An Avantes spectrometer (Avaspec-ULS2048CL-EVO-RS) was used in transmission mode to collect UV−vis−NIR optical measurements on glass substrates immediately after doping.

5.5.6 ATR:FTIR Measurements

A Nicolet iS Fourier transform infrared spectrometer with a Pike attenuated total reflectance (ATR) attachment (diamond crystal) was used to measure midinfrared spectra of doped films. Pristine and doped films were mounted “facedown” onto the diamond ATR crystal so that the film was in direct contact with the ATR crystal. Pressure was applied to ensure contact between the film and the ATR crystal.

5.5.7 XPS Measurements and Deconvolutions

XPS was conducted with a Thermo Scientific K-Alpha (Waltham, MA) system. A monochromatic Al Kα X-ray source (1486.6 eV) was used with a 60° incident angle and a 90° emission collection geometry. A survey scan with a 1.0 eV step size and high-resolution scans for C, S, Fe, and Cl with 0.1 eV step size were taken for each film. XPS can detect lighter elements at about 1% of the total surface composition and heavier elements down to ~0.1% with an accuracy of 20-50 percent of the given value. Peak fitting was performed using Casa XPS analysis software. Peak positions were corrected by shifting the primary C 1s core level position to 284.8 eV, and deconvolutions were fit with quasi-Voigt lines following a Shirley background subtraction.

5.5.8 GIWAXS Measurements

GIWAXS was performed at the Lawrence Berkeley National Laboratory Advanced Light Source on beamline 7.3.3.[200] A Pilatus 2M area detector was used, and the sample-detector distance was 276.803 mm. The X-ray energy was 10 keV. Samples were exposed for 30-60 seconds at an incidence angle of 0.14°. Measurements were performed in a helium filled chamber to minimize air scattering. An AgB calibrant was used to determine beam center position and sample-detector distance. Data reduction was processed using the Nika software within Igor Pro.[201]

5.5.9 Thermoelectric Measurements

A custom-built thin-film thermoelectric property measurement set-up was used that is well described elsewhere.[80] In short, electrical conductivity and Seebeck coefficient measurements were performed in increments of 2.5 K between *ca.* 283 and 313 K. This temperature range was selected because poly(alkyl thiophenes) doped can thermally dedope in air at elevated temperatures.[80] After doping and thermoelectric measurements, the film thickness was measured using a Profilm optical profilometer. A small scratch was scribed into the film using a plastic stylus and the average step height across the film and scratch was measured.

5.6 Acknowledgements

Funding: MPG and JPW gratefully acknowledge support from the National Science Foundation Graduate Research Fellowship. SAG appreciates the partial support from the Office of Naval Research (award number N00014-19-1-2162), the Department of Education Graduate Assistance in Areas of National Need (GAANN) program at the Georgia Institute of Technology (Award #P200A180075), the Link Energy Foundation, and the Science and Technology of Material Interfaces (STAMI) group at the Georgia Institute of Technology. SY and DSS are grateful for support from the NSERC of Canada and the University of Toronto Connaught Foundation for a McLean Award.

This work was performed in part at the Molecular Foundry and the Advanced Light Source (beamline 7.3.3), Lawrence Berkeley National Laboratory, and was supported by the Department of Energy, Office of Science, Office of Basic Energy Sciences, Scientific User Facilities Division of the U.S. Department of Energy under Contract No. DE-AC02-05CH11231. Part of this work was also performed at the Georgia Tech Institute for Electronics and Nanotechnology, a member of the National Nanotechnology Coordinated Infrastructure, which is supported by the National Science Foundation (Grant ECCS-1542174).

5.7 Supporting Information

5.7.1 UV-Vis-NIR Properties

Figure 5.5 plots the UV-Vis-NIR spectra for polymer thin films on glass substrates as a function of polymer chemistry and extent of F4TCNQ doping. In each panel of **Figure 5.5**, black lines show the pristine polymer spectra, and each colored spectrum represents a dopant concentration. Light blue, red, and green vertical lines illustrate previously reported absorbances associated with charge transfer complex doping (CTC, located at *ca*. 364, 685 nm), integer charge transfer doping (ICT, located at *ca.* 410 nm, 760 nm, 875 nm), and residual F4TCNQ (390 nm), respectively.[177,182,190,194][192]

Figure 5.5a plots the spectra for P3RT. Pristine P3RT shows a π-π* absorbance at *ca.* 520. This peak does not attenuate significantly with F4TCNQ sequential doping, but it broadens. At high doping concentrations (25, 50 mM), P3RT films show a weak F4TCNQ anion absorbance peak at *ca*. 880 nm (ICT absorbance) and a broad shoulder from *ca.* 700 to 800 nm (CTC absorbance). Notably, at high doping concentrations, a broad infrared absorbance (associated with polarons) is not present. The combination of no π-π* bleaching, weak F4TCNQ anion peaks emerging, and no polaron absorbances forming suggests that F4TCNQ does not significantly dope P3RT. F4TCNQ not significantly doping poly(thiophenes) with branched side chains has been observed before. Thomas *et al.* showed that F4TCNQ does ICT dope P3EHT and suggested that F4TCNQ CTC dopes. Thomas and coworkers also suggested that peak (and shoulder) formation between *ca*. 620 nm and 720 nm and also near 360 nm is evidence for CTC formation.[177] Watts *et al*. showed that P3HT with higher ITC characteristics have a sharper and more distinct absorbance at *ca.* 410 nm, but P3HT with higher CTC characteristics have broadening effect near 410 nm.[182] We clearly see the red/NIR shoulder formation, and we speculate that the broadening between 360 and 400 nm agrees with CTC doping in both P3HT and P3EHT.

Figure 5.5b plots the spectra for P3RSe, and P3RSe is doped to a much greater extent than P3RT. P3RSe shows a π-π* absorbance at *ca.* 580 nm, and this absorbance is readily bleached with F4TCNQ doping. With increasing dopant concentration, the π-π* peak is further bleached and the polaronic absorbance intensity in the NIR increases. A broad F4TCNQ anion peak at *ca*. 410 and 870 nm is weak but present, and this indicates ICT doping. Interestingly, the other commonly seen F4TCNQ anion peak *ca.* 770 nm is not readily observed in P3RSe. Additionally, a clear shoulder forms near 360 to 400 nm, and this may suggest CTC doping. Based on these optical observations, P3RSe is appreciably susceptible to F4TCNQ sequential doping and likely is doped through both CTC and ITC pathways.

Figure 5.5c shows the spectra for P3RTe. Pristine P3RTe shows a π-π* absorbance at *ca.* 660 nm, and this absorbance is readily bleached with F4TCNQ doping, similar to P3RSe. Broad and intense polaronic absorbance are present, but F4TCNQ anion peaks are not easily observed. We hypothesize that the F4TCNQ anion peaks are masked by the pristine and polaronic absorbances and are possibly contributing to shoulder formation at *ca.* 770 and 870 nm. This hypothesis is further corroborated by a distinct F4TCNQ anion peak at *ca.* 410 nm and by the lack of CTC peaks or shoulders. Based on these optical observations, P3RTe is highly susceptible to F4TCNQ sequential doping and is primarily doped through ICT pathways.

To facilitate direct comparisons with prior literature, we compare the optical spectra of poly(3,7 dimethyl octyl chalcogenophenes) with P3HT. **Figure 5.5d** plots the spectra for P3HT. Pristine P3HT shows a π-π* absorbance at *ca.* 515 nm, and this absorbance is readily bleached with F4TCNQ doping; this is in stark contrast with P3RT. Upon doping P3HT polaronic absorbance emerge and F4TCNQ anion peaks are clearly defined at *ca.* 870, 770, and 415 nm. These F4TCNQ anion peaks are quite distinct in comparison to the dimethyl-octyl chalcogenophenes and are consistent with prior literature observations.[186,194] This consistency with prior literature suggests that the film preparation and doping procedures herein can dope conjugated polymers, if they contain the proper spatial and energetic attributes for F4TCNQ sequential doping.

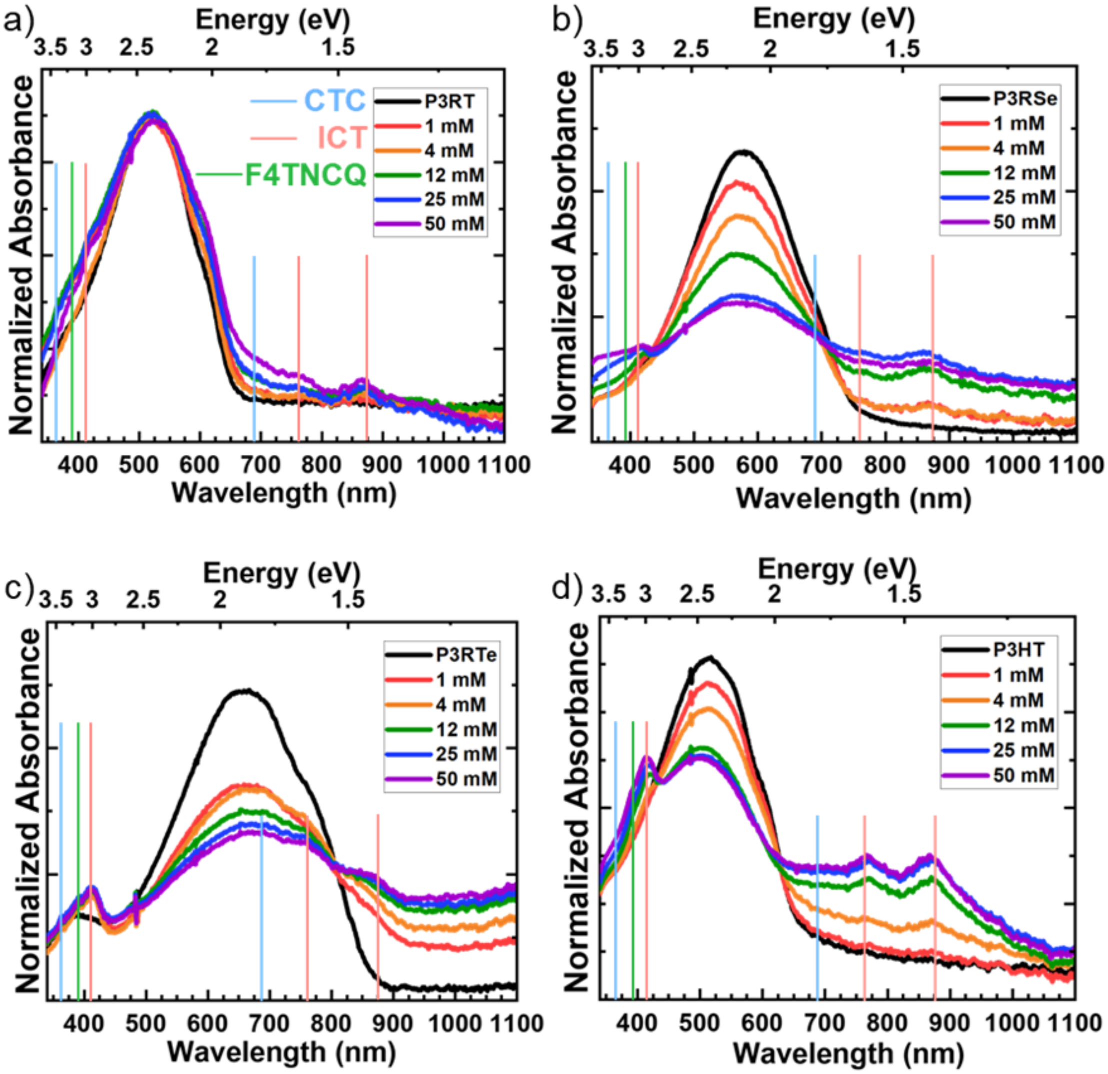

Figure 5.5- UV-Vis-NIR spectra of pristine and F4TCNQ doped films. (a) P3RT, (b) P3RSe, (c) P3RTe, (d) P3HT.

5.7.2 ATR-FTIR Properties

To further corroborate the trends observed in the UV-Vis-NIR spectra, we performed ATR-FTIR measurements. **Figure 5.6** shows the spectra for vapor doped films, and 50 mM solution doped. These measurements provide semi-quantitative insights into the extent of doping, the charge carrier delocalization, and the doping mechanism. [177,182,190,192,202] All vapor doped films (and 50 mM solution doped films) show broad optical absorbances ranging from *ca*. 1500 cm^{-1} to over 5000 cm^{-1}. This absorbance generally increases with increasing solution concentration and increasing polaronic charge carrier concentration, consistent with the UV-vis-NIR plots. Additionally, the ratio of the interchain absorbances (located at wavenumbers *ca.* < 1400 cm^{-1} and also associated with the aromatic/quinoid vibrational modes) with respect to the intrachain peak polaronic absorbance (located at *ca.* > 3000 cm^{-1} and also associated with the first polaronic optical transition) is indicative of the polaronic charge carrier delocalization.[194,202] As this ratio increases, the charge carrier is increasingly delocalized within the aggregate of the polymer. Because the dopant chemistry is fixed, we attribute changes in this ratio to be due to the counterion charge (ICT *vs.* CTC) and polymer microstructure (*vide infra*). Based on the vapor and solution doped spectra, P3RT appears to have the most localized (lowest ratio) polaronic charge carriers. Lastly, to qualify the doping mechanisms, we examine the absorbances near 2200 cm^{-1}, which are associated with the cyano vibrational modes in F4TCNQ. These vibrational modes are magnified and plotted in **Figure 5.6b**. Although there are several interpretations for these cyano vibrational modes, it has been reported that ICT oftentimes yields absorbances near 2194 cm^{-1}, while CTC yields absorbance varying between 2200-2015 cm^{-1}, depending on the extent of partial charge transfer.[177,182,192] **Figure 5.6b** shows that P3RSe, P3RTe, and P3HT have peak absorbances near 2194 cm^{-1} , suggesting a large ICT contribution. In contrast, P3RT shows a shoulder near 2194 cm^{-1} and a peak at 2205 cm^{-1}, associated with CTC and a partial charge transfer of 0.67*e*. Notably, P3RSe also shows a significant shoulder near *ca.* 2210 cm^{-1}, which is associated with a charge transfer of 0.5*e,* suggesting that P3RSe undergoes both ICT and CTC. Ultimately, these FTIR measurements corroborate the trends found in the UV-vis-NIR spectra and provide further evidence that P3RT is likely doped via a CTC mechanism, resulting in comparatively localized charge carriers.

The ratio of interchain (*ca.* <1400 cm-1) to intrachain absorbances (*ca.* >3000 cm-1) is indicative of the polaronic charge carrier delocalization. As this ratio increases, the charge carrier is increasingly delocalized within the aggregate of the polymer. Because the dopant chemistry is fixed, we attribute changes in this ratio to be due to the counterion charge (ICT *vs.* CTC) and polymer microstructure (*vide infra*). Based on the vapor and solution doped spectra, P3RT appears to have the most localized (lowest ratio) polaronic charge carriers.

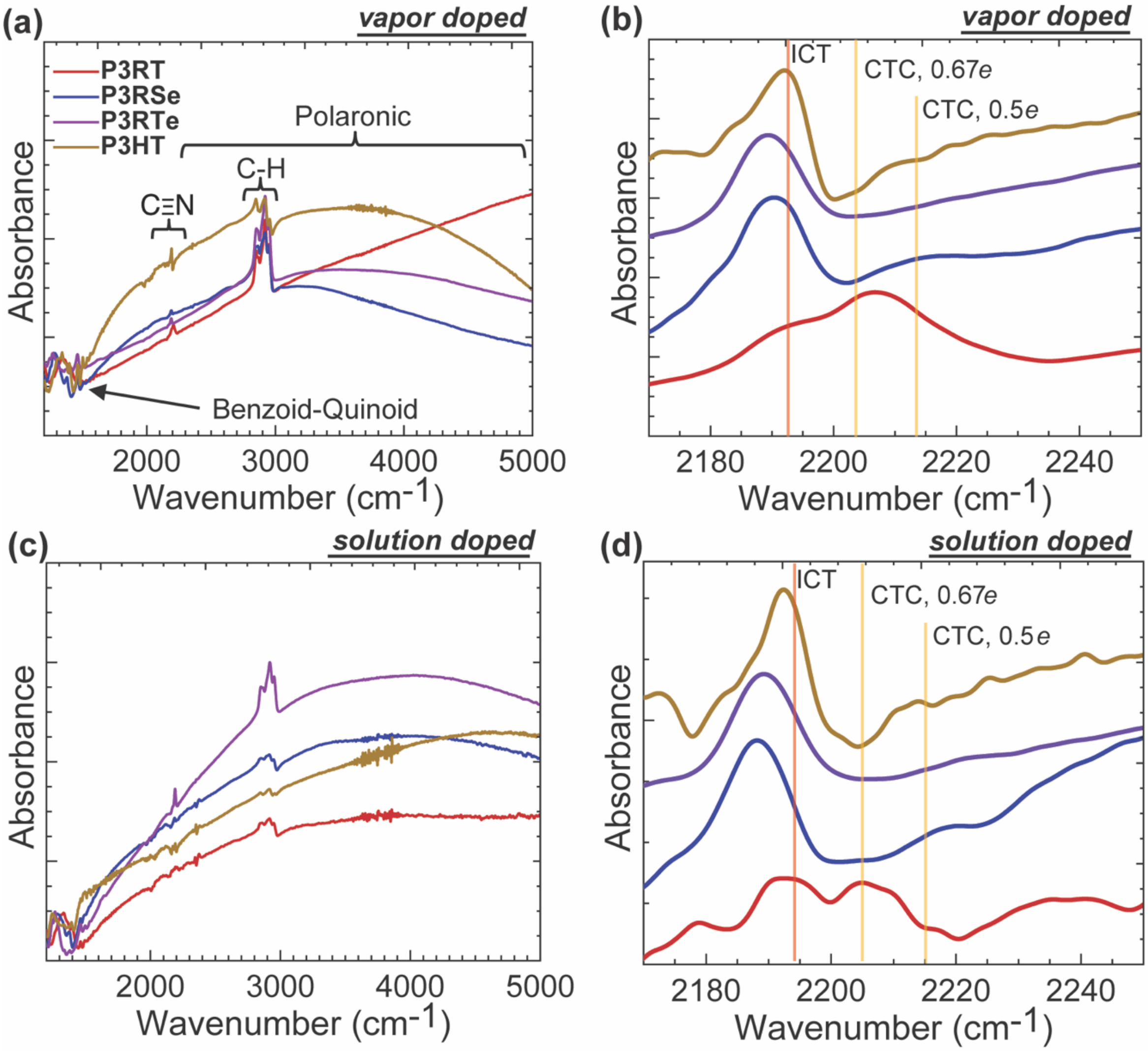

Figure 5.6- ATR-FTIR spectra of F4TCNQ doped films. vapor doped ((a) and (b)) and 50 mM solution doped ((c) and (d)) poly(alkyl chalcogenophenes) thin films. (a) and (c) Annotated MIR spectra. (b) and (d) Zoomed-in MIR spectra, highlighting the cyano absorbances and charge transfer mechanisms.

5.7.3 Electronic Property Analysis with XPS

The P3RT S-2p spectra shows a minimal shift (**Figure 5.7a**) which can easily be deconvoluted and fitted with a single doublet, but in contrast, the P3HT S-2p spectra (**Figure 5.7d)** shows significant shifts to higher binding energies and requires two sets of doublets (one doublet for neutral sulfur, and one doublet for +1 sulfur populations).[191,203] Despite these differences in binding energies, we note that both P3RT and P3HT show a maximum doping level of *ca*. 1 F4TCNQ molecule per 4 to 6 heterocycles (with both solution and vapor doped processes), consistent with previous literature. Therefore, we posit that each F4TCNQ molecule extracts more charge from the P3HT backbone in comparison to P3RT. This is consistent with the idea that P3HT dominantly participates in ICT while P3RT dominantly participates in CTC and is consistent with the UV-Vis-NIR spectra and the cyano stretching analysis (**Figure 5.6b**). Turning to P3RSe, we note that two sets of doublets are needed for the Se-3d deconvolution (**Figure 5.7b)**. This need for two doublets in P3RSe is not as readily obvious as P3HT, likely because P3RSe has a notable CTC population, consistent with the UV-vis-NIR and MIR spectra. In contrast, P3RTe shows clear signs of ICT, with increasing Te^{4+} populations at *ca.* 577 and 587 eV relative to the Te^{2+} populations at *ca.* 574 and 584 eV (**Figure 5.7c)**. Like P3RT and P3HT, most P3RSe and P3RTe doping procedures saturate with a maximum doping level of *ca*. 1 F4TCNQ molecule per 4 to 6 heterocycles. Overall, these shifts in the heteroatom binding energies further confirm that P3HT and P3RTe are primarily doped via ICT mechanisms, P3RSe shows both ICT and CTC signatures, and that P3RT is primarily doped via a CTC mechanism.

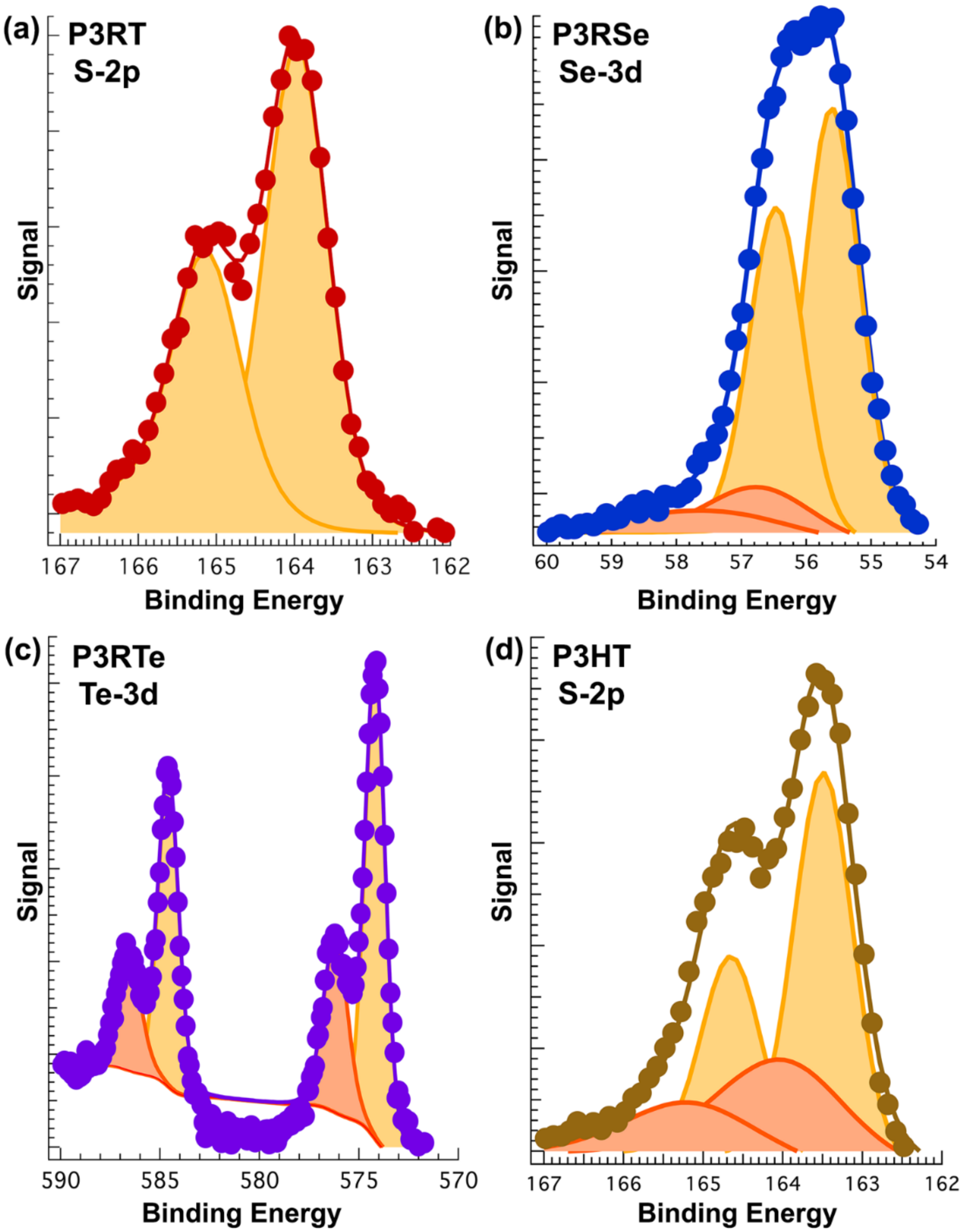

Figure 5.7- 50 mM (a) P3RT, (b) P3RSe, (c) P3RTe and (d) P3HT heteroatom deconvolutions. Orange peaks indicate blue shifted populations that interact with the F4TCNQ dopant whereas the yellow peaks are indicative of the neat populations.

Lastly, we quantify the mol fraction of F4TCNQ in P3RSe and P3RTe films using the atomic abundance of N and F (**Figure 5.8**).[180] Both P3RSe and P3RTe have an increasing F4TCNQ mol fraction with increasing dopant concentration up to *ca.* 12 mM. Beyond 12 mM, the F4TCNQ mol fraction saturates at *ca.* 0.18, which is approximately 1 F4TCNQ dopant for every 5 chalcogenophene rings. This saturated doping level is consistent with prior F4TCNQ/thiophene doping literature and is consistent with the UV-Vis-NIR spectra which show increased polaronic absorbance from 0 to 12 mM, but then show a plateauing polaronic absorbance from 12 to 50 mM (**Figure 5.5**). In general, these polymer/F4TCNQ systems exhibit a maximum doping ratio of 1 F4TCNQ dopant for every 4 to 6 heteroatom rings; however, a full integer (1*e*) charge transfer is not always associated with each F4TCNQ molecule. Therefore, the ratio of F4TCNQ to heteroatom does not need to be commensurate with the oxidized to total heteroatom ratio from the heteroatom deconvolution.

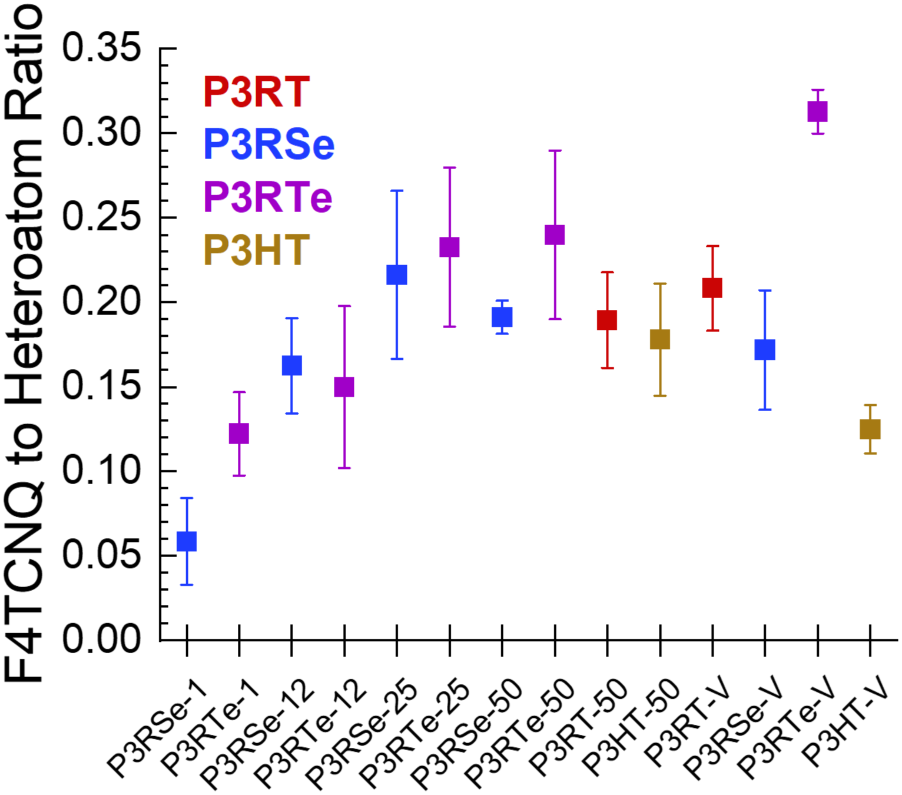

Figure 5.8- F4TCNQ:Heteroatom doping ratio. X-labels represent the doping conditions, where number (*e.g.* 1, 12, 50) represent the solution concentration in mM, and “V” represents vapor. Error bars represent the standard deviation as calculated from the F-1s and N-1s spectra.

5.7.4 Structural Properties with GIWAXS

The in-plane and nearly out-of-plane plots shown in **Figure 5.3** of the main text were created by integrating angled sector cuts as depicted below in **Figure 5.9**.

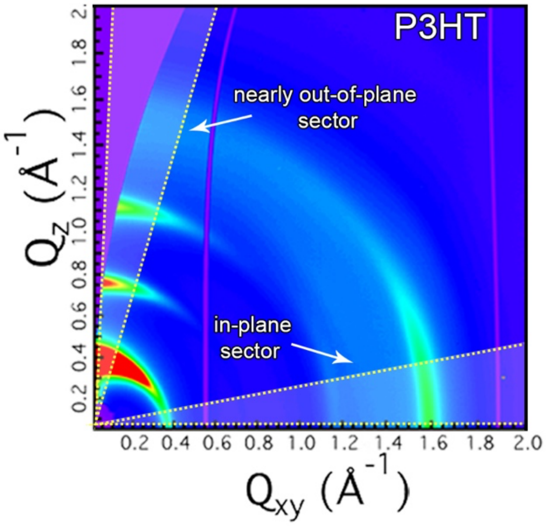

Figure 5.9- Depiction of in-plane and nearly out of plane sector integrations.

Initial analysis of the neat polymers reveals interesting differences in structural ordering. **Figure 5.3** shows that both P3RT and P3RSe demonstrate higher degrees of crystalline ordering in comparison to standard P3HT and P3RTe, with out-of-plane line cuts (*Q_z)* showing higher order reflections up to the 5th order. In addition to demonstrating high degrees of crystallinity, doublets can also be observed for lamellar stacking peaks, before and after doping as shown in **Figure 5.10 a** and **b**. This is likely indicative of two differently ordered crystalline populations demonstrating different degrees of branched alkyl sidechain interdigitation, as has been discussed by Kynaston *et al.* for a similar block copolymer system.[204]

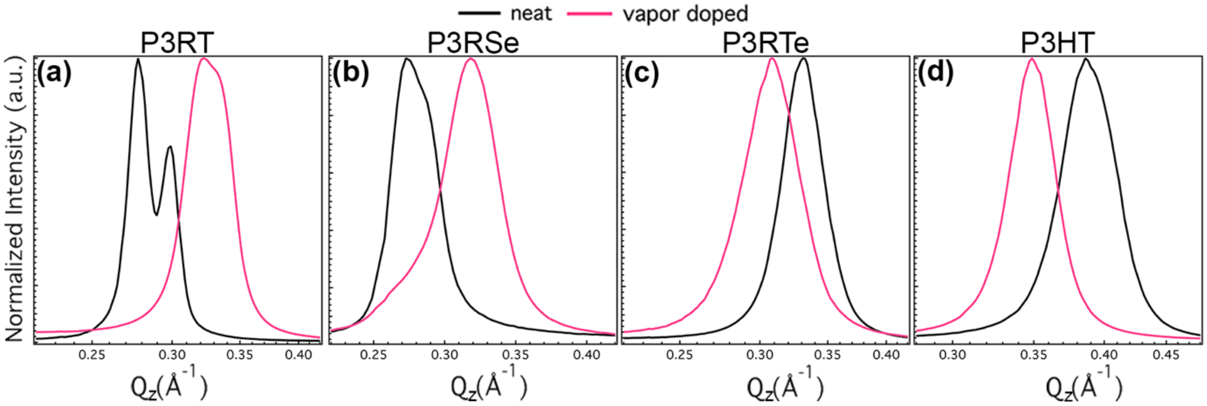

Figure 5.10- Nearly out-of-plane GIWAXS (100) peak line cuts for (a) P3RT, (b) P3RSe, (c) P3RTe, and (d) P3HT before and after vapor doping. Both (a) and (b) demonstrate that the doublets observed before doping are also present after doping as well.

All the polymers probed here demonstrate a strong edge-on orientation except for P3RSe which demonstrates a high degree of both edge-on and face-on crystallites, as shown in Figure 3a. Appearance of sharp multiplet peaks is attributed to neutral F4TCNQ molecules on the surface of the sample after doping, **Figure 5.11**.[205]

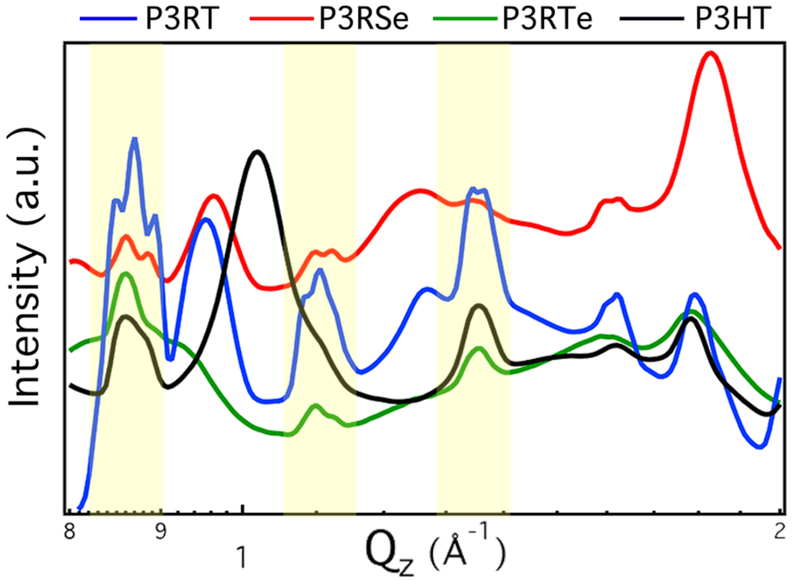

Figure 5.11- Analyzing neutral F4TCNQ in GIWAXS line cuts. Zoomed in GIWAXS nearly out-of-plane line cuts of F4TCNQ doped P3RT, P3RSe, P3RTe and P3HT demonstrate the consistent nature with which sharp peaks appear that are indicative of neutral F4TCNQ molecules in the polymer thin film at the time of the measurement.

To further probe the impact of doping upon the samples, coherence length calculations were performed, **Table 5.1**. Coherence length calculations were carried out according to the Scherrer equation, $L_C = 2\pi k/\Delta q$ where L_c is the coherence length or grain size, k is the shape factor and Δq is the full width at half maximum (FWHM) of the peak. Due to the higher order reflections present in our system, we employ the method detailed by Rivnay *et al.* where coherence length is tabulated according to a best fit line of all the (h00) peak FWHMs plotted as a function of reflection order as is shown in **Figure 5.12**.[206,207] This technique was utilized in an effort to decouple competing effects unrelated to grain size that might cause peak broadening to occur. **Table 5.1** displays the coherence length values for the chalcogenophene polymers before and after vapor doping, for both the lamellar and pi-pi stacking directions. It should be noted that the pi-pi grain sizes are likely an over-estimation due to a lack of higher order reflections to aid in deconvolution, however, the general trends still hold.

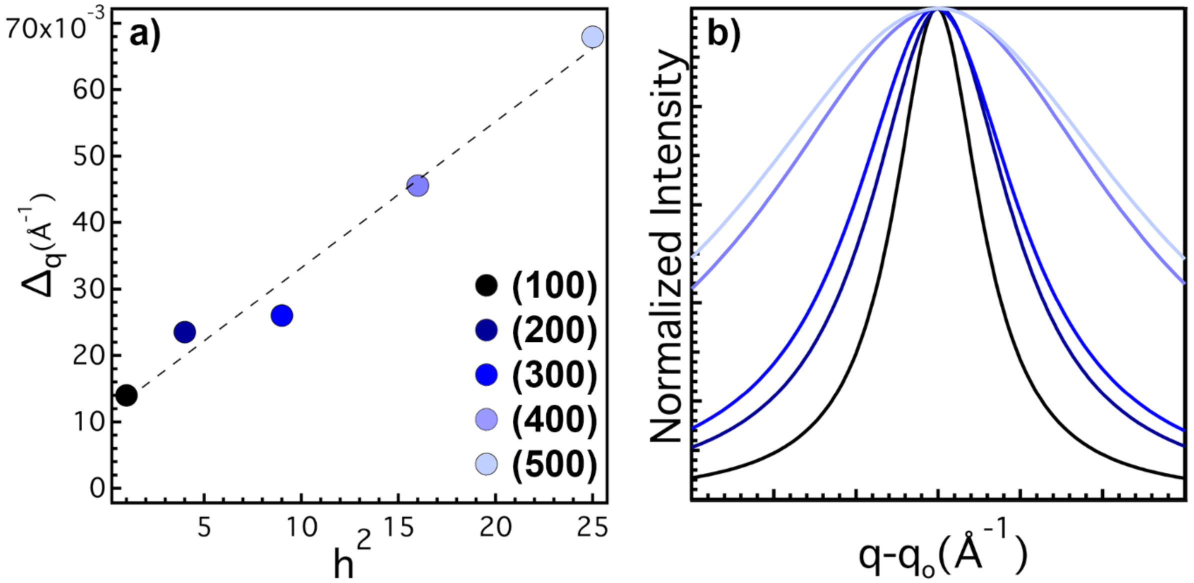

Figure 5.12- Calculating coherence lengths. Full width half max (Δq) determination in order to calculate coherence length. Panel a) shows Δq of the different (h00) reflections plotted as a function of h^2 and a line of best fit finding the intersection point with the y-axis. The intercept is then used as the Δq in the Scherrer formula to determine coherence length. This method is appropriate to use based upon inspection of panel b) peak breadth (q-q_o), which shows a distinct broadening of higher order reflections. Higher order broadening indicates that peak width is impacted not only by grain size but also by other effects such as thermal fluctuations, thus utilizing the y intercept rather than (100) value for Δq is more accurate and helps to negate over estimation of coherence length that might occur.

Table 5.1- Coherence lengths corresponding to lamellar stacking (h00) and pi-pi stacking (010)

	Type	Lc (nm)
P3RT	(h00)	50.5
	(010)	3.8
vapor doped	(h00)	24.8
	(010)	4.8
P3RSe	(h00)	25.4
	(010)	5.6
vapor doped	(h00)	9.50
	(010)	4.5
P3RTe	(h00)	21.7
	(010)	2.2
vapor doped	(h00)	31.8
	(010)	4.5
P3HT	(h00)	13.4
	(010)	6.3
vapor doped	(h00)	18.5
	(010)	4.6

Unsurprisingly, pristine P3RT, the polymer showing highest order reflections, displays the largest coherence length of all the undoped polymers. For the lamellar (h00) peaks, P3RT and P3RSe demonstrate coherence lengths that decrease significantly after F4TCNQ vapor doping, this is consistent with findings for CTC dominated systems discussed by Thomas *et al.*.[177] P3RTe and P3HT also show expected trends, upon vapor doping the coherence length in the out-of-plane direction increases; this is consistent with findings for many ITC based polymer-dopant blends.[177,187,190,194,208]

5.7.5 Additional Notes on Thermoelectric Properties

Temperature dependent electrical conductivity measurements were performed on solution doped films to better understand and quantify to what extent the charge carriers are localized. Previous experimental and theoretical studies have shown that as the extent of doping increases, the activation energy for electrical conductivity decreases.[73,80,82,83,189] This decreasing activation barrier can be rationalized as the increasing overlap of localized potential energy wells.[73] Using the Mott polaron model, which has an Arrhenius-like temperature dependency, the activation energy for thermally activated electrical transport can be quantified. Specifically, the Mott polaron model is expressed as,

$$\sigma = \sigma_0 \exp\left(-\frac{E_a}{k_B T}\right) \tag{5.1}$$

where σ is the observable electrical conductivity, σ_0 is the hypothetical maximum electrical conductivity if localization was not present, E_a is the activation energy and represents the extent of charge carrier localization, k_B is Boltzmann's constant, and T is the absolute temperature. From a slope of $\ln(\sigma)$ *vs.* $\frac{1}{T}$ plot, E_a can be calculated.

Figure 5.13 shows the calculated E_a values for P3RSe, P3RTe, and P3HT as a function of F4TCNQ solution concentration. P3RSe films do not show a large change in E_a with increasing F4TCNQ doping concentration. Interestingly, spectroscopic measurements show that the extent of oxidation and number of F4TCNQ molecules is increasing over this doping range, but E_a does not significantly change. If the carrier density is increasing but the localization energy barriers do not decrease, then it indicates that the localized charge carrier potential energy wells are not overlapping (*i.e.* spatially narrow and energetically deep wells). This is qualitatively consistent with CTC doping mechanisms, where the charge carriers are localized in a hybridized orbital between the dopant and polymer.

In contrast, P3RTe and P3HT show a large decrease in E_a with increasing doping level. Both P3RTe and P3HT initially have large E_a values, comparable to P3RSe at 1mM (> 150 meV), but then E_a decreases with increasing doping level. E_a in P3RTe and P3HT plateau from 12 to 50 mM at *ca*. 100 meV. These trends in E_a are generally concomitant with the UV-vis-NIR absorbances and Seebeck coefficients, suggesting a direct link between E_a and carrier density. We suspect that P3HT and P3RTe show E_a values that decrease with increasing carrier density because their charge carriers are primarily formed via ICT and not localized to a hybridized molecular orbital. Lastly, there E_a values are substantially larger than those of P3RX and P3HT doped with $FeCl_3$, which demonstrate E_a values near *ca.* 25 meV and lower.[80] This is likely because $FeCl_3$ is a stronger oxidant than F4TCNQ and generates more charge carriers (closer to 1 carrier per 3 rings), thereby affording more potential well overlap. Ultimately, this analysis suggests that temperature dependent electrical conductivity measurements may be useful for elucidating CTC and ICT mechanisms.

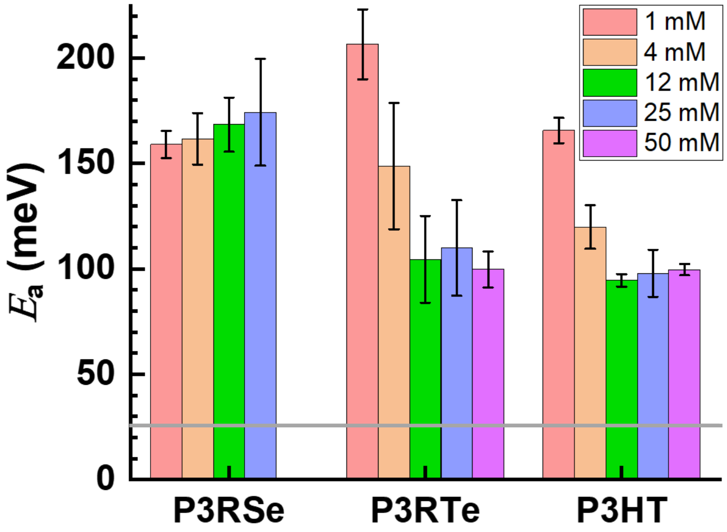

Figure 5.13- Thermal activation energies for electrical conductivity. Error bars represent sample to sample standard deviations. All doped films demonstrated statistically significant activation energies, with a 95% confidence interval. Grey line represents k_BT at 300 K.

In **Figure 5.14** the thermoelectric properties of the full doping ladder are shown. In **Figure 5.14(b)** it is worth noting that for Seebeck coefficient, P3RTe plateaus at *ca.* 75 μV/K while P3HT plateaus at *ca.* 95 μV/K. This plateau indicates that marginally fewer charge carriers are being generated with increasing F4TCNQ solution concentration. This plateauing is in good agreement with the XPS-calculated carrier concentrations for P3RTe (**Figure 5.8**), and a plateau at *ca.* 75-100 μV/K also indicates that these polymers could be further oxidized with a stronger oxidant; P3HT doped with $FeCl_3$ (a stronger oxidant) oftentimes achieves $S = 30$ μV/K with one charge carrier per three rings. Lastly, a plateau for P3HT doped with F4TCNQ near *ca.* 95 μV/K with these doping procedures is in reasonable agreement with previous literature.[177,189,194]

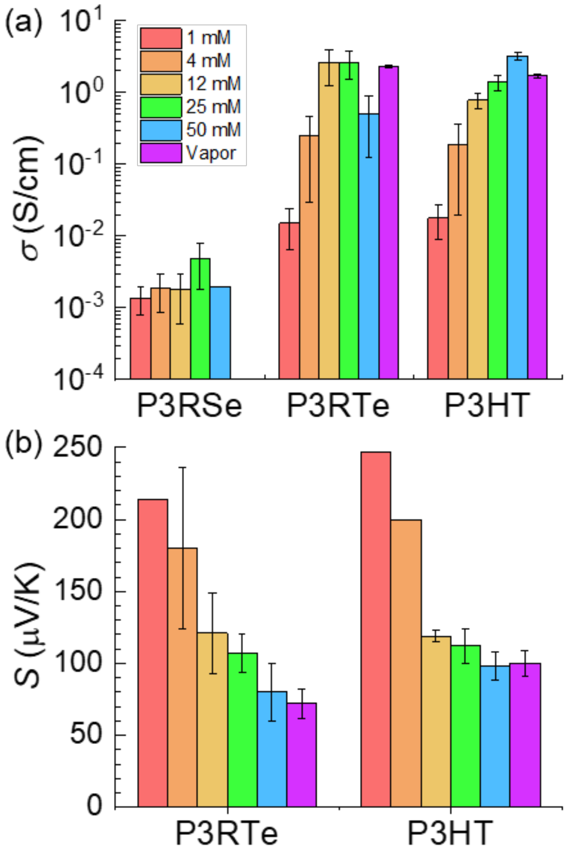

Figure 5.14- Electrical conductivity (a) and Seebeck coefficient (b) of full doping ladder. Error bars, when present, represent sample to sample standard deviations**.**

Chapter 6. Conclusions and Future Outlooks

With the ability to transform waste heat into electricity, thermoelectrics hold great potential but have thus far fallen short of widespread deployment. The future commercialization of thermoelectric devices is dependent on the improvement of a number of different factors simultaneously including material property enhancement, device design and decreasing manufacturing costs. As the need for power supplies for the ever-multiplying number of small and personal electronic devices grows, greater emphasis is placed on the development of conformal and flexible thermoelectrics. Soft hybrid thermoelectric material development is a field that holds great potential for filling this need but is inherently plagued with a host of challenges including effective modeling and understanding the transport physics at play. For even the most well studied hybrid systems there still remain gaps and disagreements in the literature surrounding the physical underpinnings., These knowledge gaps make it especially challenging to develop new hybrid materials that demonstrate synergistic performance enhancements, a classic calling card of a true hybrid material, due to the lack of well-established rational design rules to act as a guide. This dissertation focuses upon establishing an understanding of the structure-function relationships in soft thermoelectric materials through rational design.

In Chapter 3 we demonstrated that by changing the molecular weight of the surface ligand it is possible to modulate the diameter and length of synthesized Te nanowires. Ultimately these changes in dimension impact the electronic transport to result in a ~183% performance enhancement for the narrowest diameter set of hybrid thin films. This diameter dependent trend challenges the established literature understanding of aspect ratio being the most critical dimension for tuning electron transport. In Chapter 4, we dive more deeply into the cause for this diameter dependent trend by investigating charge and heat transport in a single hybrid nanowire. This measurement captures the effects of nanoscale templating at the hybrid interface for the first time and helps to bridge the knowledge gap between atomic scale simulations and bulk thin film measurements. We find that electrical transport predominantly occurs through the organic shell, whereas thermal transport primarily occurs within the inorganic core. This understanding reveals an avenue for decoupling these notoriously linked thermoelectric parameters and results in a remarkable ZT of 0.54 achieved at 400 K.

Given the critical nature of the organic shell for electron transport, in Chapter 5, we investigate additional methods for controlling organic polymer morphology, doping mechanism and charge transport properties through heteroatom substitution. We demonstrate that by substituting the heteroatom with Sulfur, Selenium and Tellurium it is possible to tune the degree of rotational freedom of the polymer backbone, driving the degree of morphological order. Through our x-ray scattering studies we found that the extent of ordering ultimately drives the type of polymer:dopant interaction which has a direct impact on charge transport performance.

Looking forwards, one important area that merits additional investigation is characterizing the structure of the thin organic shell. This task is challenging due to the 1-2 nm thick semi-amorphous organic shell sitting on top of a crystalline inorganic core. There are many techniques developed for probing the structure of thin polymer films. One such technique is GIWAXS (a technique applied in Chapter 5). GIWAXS is a very handy technique for thin films because rather than having the incident x-ray approach at an angle perpendicular to the film surface, here the x-ray approaches at a very shallow angle. This shallow incident angle limits the penetration depth of the beam (which is optimal for ensuring that only the polymer is sampled and not the substrate underneath it) and spreads out the beam footprint, increasing the number of atoms the incident beam interacts with to ultimately increase scattering signal intensity.[200] However, even a technique such as GIWAXS inevitably picks up a fair degree of high intensity scattering contribution from the inorganic core, masking any organic morphology signals. Some recent advancements in transmission electron microscopy (TEM) and resonant x-ray scattering holds promise for overcoming these challenges. A study published by Kuei *et al.* demonstrates success in using TEM to image the 3.6 Å lattice spacing of poly[(5,6-difluoro-2,1,3-benzothiadiazol-4,7-diyl)-alt-(3,3‴-di(2-octyldodecyl)-2,2′;5′,2″;5″,2‴-quaterthiophene-5,5‴-diyl)] with the help of added antioxidants. This work is significant progress seeing as using TEM for characterizing polymer morphology on an atomic scale has been a challenge due to the damage inflicted by the electron beam on such a soft material. Applying such a technique to a hybrid material may enable the effective tracking of currently elusive morphology changes in the organic shell. Additionally, a recent study by Freychet *et al.* employed resonant diffraction (a phenomenon that occurs when the incident x-ray energy corresponds to the x-ray absorption edge of a certain element present in the sample) to exclusively probe the sulfur edge of the conjugated polymer poly([*N,N'*-bis(2-octyldodecyl)-naphthalene-1,4,5,8-bis(dicarboximide)-2,6-diyl]-*alt*-5,5'-(2,2'-bithiophene)).[209] This study found that resonant diffraction is able to differentiate between discrete crystalline packing motifs. Such a capability would enable the possibility for probing the structure of the organic shell without interference from the inorganic core by simply tuning the energy of the incident x-ray beam. By employing these types of cutting-edge techniques, I believe it is possible to fully reveal the remaining mysteries surrounding transport phenomenon in these hybrid systems.

Ultimately, from the fundamental understandings detailed in this dissertation, it is possible to envisage the rational design of myriad high performing hybrid materials. These advanced materials will pair new inorganic nanostructures (*e.g.* more environmentally friendly options such as bismuth or sulfur) with tunable conjugated polymers or small molecules to result in new p-type materials and more elusive n-type hybrids as well. With the realization of such materials, it will be possible to help thermoelectric technologies find more widespread deployment for a whole host of new cutting-edge applications.

Chapter 7. References

[1] S. Lin, W. Li, Z. Chen, J. Shen, B. Ge, Y. Pei, *Nat Commun* **2016**, *7*, 1.

[2] P. D. Mitcheson, E. M. Yeatman, G. K. Rao, A. S. Holmes, T. C. Green, *Proceedings of the IEEE* **2008**, *96*, 1457.

[3] A. Raj, D. Steingart, *J. Electrochem. Soc.* **2018**, *165*, B3130.

[4] J.-H. Bahk, H. Fang, K. Yazawa, A. Shakouri, *J. Mater. Chem. C* **2015**, *3*, 10362.

[5] Y. Chen, Y. Zhao, Z. Liang, *Energy Environ. Sci.* **2015**, *8*, 401.

[6] X. Dong, S. Xiong, B. Luo, R. Ge, Z. Li, J. Li, Y. Zhou, *ACS Appl. Mater. Interfaces* **2018**, *10*, 26687.

[7] L. GALVANI, *De Bonoiensi Scientiarum et Artium Intituo atque Academie Commentarii* **1791**, *7*, 363.

[8] T. J. Seebeck, *Annalen der Physik* **1826**, *82*, 253.

[9] William Thomson, *Proc.Roy.Soc.Edinburgh* **1851**, 91.

[10] L. R. F.R.S, *The London, Edinburgh, and Dublin Philosophical Magazine and Journal of Science* **1885**, *20*, 361.

[11] E. Altenkirch, *Phys. Z.* **1911**, *12*, 920.

[12] J. B. J. Fourier, H. D. Oersted, *Ann. Chim. Phys.* **1823**, *22*, 375.

[13] L. Onsager, *Phys. Rev.* **1931**, *37*, 405.

[14] L. Onsager, *Phys. Rev.* **1931**, *38*, 2265.

[15] D. Beretta, N. Neophytou, J. M. Hodges, M. G. Kanatzidis, D. Narducci, M. Martin-Gonzalez, M. Beekman, B. Balke, G. Cerretti, W. Tremel, A. Zevalkink, A. I. Hofmann, C. Müller, B. Dörling, M. Campoy-Quiles, M. Caironi, *Materials Science and Engineering: R: Reports* **2019**, *138*, 100501.

[16] L. D. Hicks, M. S. Dresselhaus, *Physical Review B* **1993**, *47*, 16631.

[17] M. S. Dresselhaus, G. Dresselhaus, X. Sun, Z. Zhang, S. B. Cronin, T. Koga, *Phys. Solid State* **1999**, *41*, 679.

[18] M. S. Dresselhaus, G. Chen, M. Y. Tang, R. G. Yang, H. Lee, D. Z. Wang, Z. F. Ren, J.-P. Fleurial, P. Gogna, *Adv. Mater.* **2007**, *19*, 1043.

[19] M. S. Dresselhaus, X. Sun, S. B. Cronin, T. Koga, G. Dresselhaus, K. L. Wang, *MRS Online Proceedings Library* **1997**, *478*, 55.

[20] G. J. Snyder, E. S. Toberer, *Nature Mater* **2008**, *7*, 105.

[21] C. Goupil, W. Seifert, K. Zabrocki, E. Müller, G. J. Snyder, *Entropy* **2011**, *13*, 1481.

[22] D. M. Rowe, *Thermoelectrics Handbook: Macro to Nano*, CRC Press, **2018**.

[23] B. Russ, A. Glaudell, J. J. Urban, M. L. Chabinyc, R. A. Segalman, *Nature Reviews Materials* **2016**, *1*, 16050.

[24] A. Bonfiglio, D. D. Rossi, Eds. , *Wearable Monitoring Systems*, Springer US, **2011**.

[25] A. Bals, N. Barnes, R. Bravo, N. Garcia, J. O'Bryan, D. Santana, **n.d.**, 126.

[26] H. Mamur, M. R. A. Bhuiyan, F. Korkmaz, M. Nil, *Renewable and Sustainable Energy Reviews* **2018**, *82*, 4159.

[27] X. Hu, P. Jood, M. Ohta, M. Kunii, K. Nagase, H. Nishiate, M. G. Kanatzidis, A. Yamamoto, *Energy Environ. Sci.* **2016**, *9*, 517.

[28] M. G. Kanatzidis, *Chem. Mater.* **2010**, *22*, 648.

[29] J. R. Sootsman, R. J. Pcionek, H. Kong, C. Uher, M. G. Kanatzidis, *Chem. Mater.* **2006**, *18*, 4993.

[30] A. J. Minnich, M. S. Dresselhaus, Z. F. Ren, G. Chen, *Energy Environ. Sci.* **2009**, *2*, 466.

[31] C. J. Vineis, A. Shakouri, A. Majumdar, M. G. Kanatzidis, *Advanced Materials* **2010**, *22*, 3970.

[32] D. A. Wright, *Nature* **1958**, *181*, 834.

[33] J. Yang, H.-L. Yip, A. K.-Y. Jen, *Advanced Energy Materials* **2013**, *3*, 549.

[34] A. Shakouri, *Annual Review of Materials Research* **2011**, *41*, 399.

[35] H. M. Elmoughni, A. K. Menon, R. M. W. Wolfe, S. K. Yee, *Advanced Materials Technologies* **2019**, *4*, 1800708.

[36] A. K. Menon, S. K. Yee, *Journal of Applied Physics* **2016**, *119*, 055501.

[37] E. W. Zaia, M. P. Gordon, P. Yuan, J. J. Urban, *Advanced Electronic Materials* **2019**, *5*, 1800823.

[38] Q. Zhang, Y. Sun, W. Xu, D. Zhu, *Advanced Materials* **2014**, *26*, 6829.

[39] M. P. Gordon, S. A. Gregory, J. P. Wooding, S. Ye, G. M. Su, D. S. Seferos, M. D. Losego, J. J. Urban, S. K. Yee, A. K. Menon, *Appl. Phys. Lett.* **2021**, *118*, 233301.

[40] B. J. Worfolk, S. C. Andrews, S. Park, J. Reinspach, N. Liu, M. F. Toney, S. C. B. Mannsfeld, Z. Bao, *PNAS* **2015**, *112*, 14138.

[41] T. D. Anthopoulos, G. C. Anyfantis, G. C. Papavassiliou, D. M. de Leeuw, *Applied Physics Letters* **2007**, *90*, 122105.

[42] D. M. de Leeuw, M. M. J. Simenon, A. R. Brown, R. E. F. Einerhand, *Synthetic Metals* **1997**, *87*, 53.

[43] J. E. Anthony, A. Facchetti, M. Heeney, S. R. Marder, X. Zhan, *Advanced Materials* **2010**, *22*, 3876.

[44] B. Russ, M. J. Robb, F. G. Brunetti, P. L. Miller, E. E. Perry, S. N. Patel, V. Ho, W. B. Chang, J. J. Urban, M. L. Chabinyc, C. J. Hawker, R. A. Segalman, *Adv. Mater. Weinheim* **2014**, *26*, 3473.

[45] R. A. Schlitz, F. G. Brunetti, A. M. Glaudell, P. L. Miller, M. A. Brady, C. J. Takacs, C. J. Hawker, M. L. Chabinyc, *Adv. Mater. Weinheim* **2014**, *26*, 2825.

[46] B. J. Jung, N. J. Tremblay, M.-L. Yeh, H. E. Katz, *Chem. Mater.* **2011**, *23*, 568.

[47] Y. Sun, P. Sheng, C. Di, F. Jiao, W. Xu, D. Qiu, D. Zhu, *Advanced Materials* **2012**, *24*, 932.

[48] W. Shi, G. Wu, X. Yong, T. Deng, J.-S. Wang, J.-C. Zheng, J. Xu, M. B. Sullivan, S.-W. Yang, *ACS Appl. Mater. Interfaces* **2018**, *10*, 35306.

[49] D. Patidar, N. S. Saxena, *Advances in Nanoparticles* **2013**, *2*, 11.

[50] A. Sahu, B. Russ, N. C. Su, J. D. Forster, P. Zhou, E. S. Cho, P. Ercius, N. E. Coates, R. A. Segalman, J. J. Urban, *Journal of Materials Chemistry A* **2017**, *5*, 3346.

[51] P. Kumar, E. W. Zaia, E. Yildirim, D. V. M. Repaka, S.-W. Yang, J. J. Urban, K. Hippalgaonkar, *Nature Communications* **2018**, *9*, 5347.

[52] K. C. See, J. P. Feser, C. E. Chen, A. Majumdar, J. J. Urban, R. A. Segalman, *Nano Lett.* **2010**, *10*, 4664.

[53] N. E. Coates, S. K. Yee, B. McCulloch, K. C. See, A. Majumdar, R. A. Segalman, J. J. Urban, *Advanced Materials* **2013**, *25*, 1629.

[54] E. W. Zaia, A. Sahu, P. Zhou, M. P. Gordon, J. D. Forster, S. Aloni, Y.-S. Liu, J. Guo, J. J. Urban, *Nano Letters* **2016**, *16*, 3352.

[55] M. P. Gordon, K. Haas, E. Zaia, A. K. Menon, L. Yang, A. Bruefach, M. D. Galluzzo, M. C. Scott, R. S. Prasher, A. Sahu, J. J. Urban, *Advanced Electronic Materials* **2021**, *7*, 2000904.

[56] E. W. Zaia, M. P. Gordon, V. Niemann, J. Choi, R. Chatterjee, C.-H. Hsu, J. Yano, B. Russ, A. Sahu, J. J. Urban, *Advanced Energy Materials* **2019**, *9*, 1803469.

[57] A. Sahu, B. Russ, M. Liu, F. Yang, E. W. Zaia, M. P. Gordon, J. D. Forster, Y.-Q. Zhang, M. C. Scott, K. A. Persson, N. E. Coates, R. A. Segalman, J. J. Urban, *Nat Commun* **2020**, *11*, 1.

[58] R. Tian, C. Wan, Y. Wang, Q. Wei, T. Ishida, A. Yamamoto, A. Tsuruta, W. Shin, S. Li, K. Koumoto, *J. Mater. Chem. A* **2017**, *5*, 564.

[59] F. Erden, H. Li, X. Wang, F. Wang, C. He, *Phys. Chem. Chem. Phys.* **2018**, *20*, 9411.

[60] Y. Lu, Y. Qiu, Q. Jiang, K. Cai, Y. Du, H. Song, M. Gao, C. Huang, J. He, D. Hu, *ACS Appl. Mater. Interfaces* **2018**, *10*, 42310.

[61] Q. Meng, K. Cai, Y. Du, L. Chen, *Journal of Alloys and Compounds* **2019**, *778*, 163.

[62] K. Choi, S. L. Kim, S.-I. Yi, J.-H. Hsu, C. Yu, *ACS Appl Mater Interfaces* **2018**, *10*, 23891.

[63] L. Wang, Z. Zhang, Y. Liu, B. Wang, L. Fang, J. Qiu, K. Zhang, S. Wang, *Nat Commun* **2018**, *9*, 1.

[64] C. Kim, J. Y. Baek, D. H. Lopez, D. H. Kim, H. Kim, *Appl. Phys. Lett.* **2018**, *113*, 153901.

[65] K. Kato, K. Kuriyama, T. Yabuki, K. Miyazaki, *J. Phys.: Conf. Ser.* **2018**, *1052*, 012008.

[66] Q. Jin, S. Jiang, Y. Zhao, D. Wang, J. Qiu, D.-M. Tang, J. Tan, D.-M. Sun, P.-X. Hou, X.-Q. Chen, K. Tai, N. Gao, C. Liu, H.-M. Cheng, X. Jiang, *Nature Mater* **2019**, *18*, 62.

[67] S. Hu, S. Zeng, X. Li, J. Jiang, W. Yang, Y. Chen, M. Li, J. Zheng, *Materials & Design* **2020**, *188*, 108496.

[68] C. Ou, A. L. Sangle, T. Chalklen, Q. Jing, V. Narayan, S. Kar-Narayan, *APL Materials* **2018**, *6*, 096101.

[69] N. Lu, L. Li, M. Liu, *Physical Chemistry Chemical Physics* **2016**, *18*, 19503.

[70] R. Dhanker, C. L. Gray, S. Mukhopadhyay, S. Nunez, C.-Y. Cheng, A. N. Sokolov, N. C. Giebink, *Nature Communications* **2017**, *8*, DOI 10.1038/s41467-017-02459-3.

[71] S. D. Baranovskii, I. P. Zvyagin, H. Cordes, S. Yamasaki, P. Thomas, *physica status solidi (b)* **2002**, *230*, 281.

[72] R. M. Hill, *physica status solidi (a)* **1976**, *34*, 601.

[73] N. F. Mott, E. A. Davis, *Electronic Processes in Non-Crystalline Materials*, OUP Oxford, **2012**.

[74] S. D. Kang, G. J. Snyder, *Nature Materials* **2017**, *16*, 252.

[75] M. Statz, D. Venkateshvaran, X. Jiao, S. Schott, C. R. McNeill, D. Emin, H. Sirringhaus, R. Di Pietro, *Commun Phys* **2018**, *1*, 1.

[76] J. L. Blackburn, S. D. Kang, M. J. Roos, B. Norton-Baker, E. M. Miller, A. J. Ferguson, *Advanced Electronic Materials* **2019**, *5*, 1800910.

[77] E. M. Thomas, B. C. Popere, H. Fang, M. L. Chabinyc, R. A. Segalman, *Chem. Mater.* **2018**, *30*, 2965.

[78] C. J. Boyle, M. Upadhyaya, P. Wang, L. A. Renna, M. Lu-Díaz, S. P. Jeong, N. Hight-Huf, L. Korugic-Karasz, M. D. Barnes, Z. Aksamija, D. Venkataraman, *Nat Commun* **2019**, *10*, 1.

[79] S. A. Gregory, R. Hanus, A. Atassi, J. M. Rinehart, J. P. Wooding, A. K. Menon, M. D. Losego, G. J. Snyder, S. K. Yee, *Nat. Mater.* **2021**, 1.

[80] S. A. Gregory, A. K. Menon, S. Ye, D. S. Seferos, J. R. Reynolds, S. K. Yee, *Advanced Energy Materials* **2018**, *8*, 1802419.

[81] A. M. Glaudell, J. E. Cochran, S. N. Patel, M. L. Chabinyc, *Adv. Energy Mater.* **2015**, *5*, n/a.

[82] K. A. Kurdi, S. A. Gregory, S. Jhulki, M. Conte, S. Barlow, S. K. Yee, S. R. Marder, *Mater. Adv.* **2020**, *1*, 1829.

[83] H.-I. Un, S. A. Gregory, S. K. Mohapatra, M. Xiong, E. Longhi, Y. Lu, S. Rigin, S. Jhulki, C.-Y. Yang, T. V. Timofeeva, J.-Y. Wang, S. K. Yee, S. Barlow, S. R. Marder, J. Pei, *Advanced Energy Materials* **2019**, *9*, 1900817.

[84] Y. Xuan, X. Liu, S. Desbief, P. Leclère, M. Fahlman, R. Lazzaroni, M. Berggren, J. Cornil, D. Emin, X. Crispin, *Phys. Rev. B* **2010**, *82*, 115454.

[85] J. A. Malen, S. K. Yee, A. Majumdar, R. A. Segalman, *Chemical Physics Letters* **2010**, *491*, 109.

[86] E. J. Bae, Y. H. Kang, K.-S. Jang, S. Y. Cho, *Scientific Reports* **2016**, *6*, 18805.

[87] M. He, J. Ge, Z. Lin, X. Feng, X. Wang, H. Lu, Y. Yang, F. Qiu, *Energy Environ. Sci.* **2012**, *5*, 8351.

[88] Q. Li, *Functional Organic and Hybrid Nanostructured Materials: Fabrication, Properties, and Applications*, John Wiley & Sons, **2018**.

[89] K. Wei, T. Stedman, Z.-H. Ge, L. M. Woods, G. S. Nolas, *Applied Physics Letters* **2015**, *107*, 153301.

[90] L. Yang, M. P. Gordon, A. K. Menon, A. Bruefach, K. Haas, M. C. Scott, R. S. Prasher, J. J. Urban, *Science Advances* **2021**, *7*, eabe6000.

[91] Z. Liang, M. J. Boland, K. Butrouna, D. R. Strachan, K. R. Graham, *J. Mater. Chem. A* **2017**, *5*, 15891.

[92] S. Ouk Kim, H. H. Solak, M. P. Stoykovich, N. J. Ferrier, J. J. de Pablo, P. F. Nealey, *Nature* **2003**, *424*, 411.

[93] W. A. Memon, J. Li, Q. Fang, Z. Ren, S. Yan, X. Sun, *J. Phys. Chem. B* **2019**, *123*, 7233.

[94] J. M. MacLeod, F. Rosei, *Small* **2014**, *10*, 1038.

[95] D. J. Bergman, L. G. Fel, **n.d.**, 13.

[96] G. Chen (PhD.), D. of M. E. G. Chen, *Nanoscale Energy Transport and Conversion: A Parallel Treatment of Electrons, Molecules, Phonons, and Photons*, Oxford University Press, **2005**.

[97] C. Kittel, *Introduction to Solid State Physics*, Wiley, **2004**.

[98] A. Weathers, Z. U. Khan, R. Brooke, D. Evans, M. T. Pettes, J. W. Andreasen, X. Crispin, L. Shi, *Advanced Materials* **2015**, *27*, 2101.

[99] J. Liu, X. Wang, D. Li, N. E. Coates, R. A. Segalman, D. G. Cahill, *Macromolecules* **2015**, *48*, 585.

[100] Y. Wang, J. Zhou, R. Yang, *J. Phys. Chem. C* **2011**, *115*, 24418.

[101] D. Moses, A. Denenstein, *Phys. Rev. B* **1984**, *30*, 2090.

[102] J. Jin, M. P. Manoharan, Q. Wang, M. A. Haque, *Appl. Phys. Lett.* **2009**, *95*, 033113.

[103] H. Wang, C. Yu, *Joule* **2019**, *3*, 53.

[104] G. Yang, J. Pan, X. Fu, Z. Hu, Y. Wang, Z. Wu, E. Mu, X.-J. Yan, M.-H. Lu, *Nano Convergence* **2018**, *5*, 22.

[105] J. J. Urban, A. K. Menon, Z. Tian, A. Jain, K. Hippalgaonkar, *Journal of Applied Physics* **2019**, *125*, 180902.

[106] K. Gordiz, A. K. Menon, S. K. Yee, *Journal of Applied Physics* **2017**, *122*, 124507.

[107] E. S. Cho, N. E. Coates, J. D. Forster, A. M. Ruminski, B. Russ, A. Sahu, N. C. Su, F. Yang, J. J. Urban, *Advanced Materials* **2015**, *27*, 5744.

[108] Q. Xue, W. Yao, J. Liu, Q. Tian, L. Liu, M. Li, Q. Lu, R. Peng, W. Wu, *Nanoscale Res Lett* **2017**, *12*, 480.

[109] L. Sonntag, F. Eichler, N. Weiß, L. Bormann, D. S. Ghosh, J. M. Sonntag, R. Jordan, N. Gaponik, K. Leo, A. Eychmüller, *Phys. Chem. Chem. Phys.* **2019**, *21*, 9036.
[110] G. Ouyang, X. L. Li, X. Tan, G. W. Yang, *Nanotechnology* **2008**, *19*, 045709.
[111] P. Ghosh, M. U. Kahaly, U. V. Waghmare, *Phys. Rev. B* **2007**, *75*, 245437.
[112] S. K. Yee, N. E. Coates, A. Majumdar, J. J. Urban, R. A. Segalman, *Physical Chemistry Chemical Physics* **2013**, *15*, 4024.
[113] X. Chen, Z. Wang, X. Wang, J. Wan, Y. Qian, *Appl. Phys. A* **2005**, *80*, 1443.
[114] B. Kim, B.-K. Park, *Electron. Mater. Lett.* **2012**, *8*, 33.
[115] H. Dong, Y.-C. Chen, C. Feldmann, *Green Chemistry* **2015**, *17*, 4107.
[116] Y.-J. Zhu, X.-L. Hu, W.-W. Wang, *Nanotechnology* **2006**, *17*, 645.
[117] Z. Liu, Z. Hu, Q. Xie, B. Yang, J. Wu, Y. Qian, *Journal of Materials Chemistry* **2003**, *13*, 159.
[118] F. Liang, H. Qian, *Materials Chemistry and Physics* **2009**, *113*, 523.
[119] L. Xu, G. Wang, X. Zheng, H. Pan, J. Zhu, Z. Li, S.-H. Yu, *Chem* **2018**, *4*, 2451.
[120] X. Zeng, B. Zhou, Y. Gao, C. Wang, S. Li, C. Y. Yeung, W. Wen, *Nanotechnology* **2014**, *25*, 495601.
[121] F.-Y. Yang, K.-J. Chang, M.-Y. Hsu, C.-C. Liu, *Journal of Materials Chemistry* **2008**, *18*, 5927.
[122] S. K. S. Basha, G. S. Sundari, K. V. Kumar, M. C. Rao, *Journal of Inorganic and Organometallic Polymers and Materials* **2017**, *27*, 455.
[123] K. A. Fichthorn, T. Balankura, X. Qi, *CrystEngComm* **2016**, *18*, 5410.
[124] Lin Yang*, Madeleine P. Gordon*, Akanksha K. Menon, Alexandra Bruefach, Kyle Haas, Mary C. Scott, Ravi S. Prasher, Jeffrey J. Urban, *Under Review* **2020**.
[125] Z. Li, S. Zheng, Y. Zhang, R. Teng, T. Huang, C. Chen, G. Lu, *Journal of Materials Chemistry A* **2013**, *1*, 15046.
[126] M. A. Hannan, S. Mutashar, S. A. Samad, A. Hussain, *BioMedical Engineering Online* **2014**, *13*, 79.
[127] M. Rein, V. D. Favrod, C. Hou, T. Khudiyev, A. Stolyarov, J. Cox, C. C. Chung, C. Chhav, M. Ellis, J. Joannopoulos, Y. Fink, *Nature* **2018**, *560*, 214.
[128] R. Chen, J. Lee, W. Lee, D. Li, *Chemical Reviews* **2019**, *119*, 9260.
[129] L. D. Hicks, M. S. Dresselhaus, *Phys. Rev. B* **1993**, *47*, 12727.
[130] A. I. Hochbaum, R. Chen, R. D. Delgado, W. Liang, E. C. Garnett, M. Najarian, A. Majumdar, P. Yang, *Nature* **2008**, *451*, 163.
[131] K. Biswas, J. He, I. D. Blum, C.-I. Wu, T. P. Hogan, D. N. Seidman, V. P. Dravid, M. G. Kanatzidis, *Nature* **2012**, *489*, 414.
[132] E. Jin Bae, Y. Hun Kang, K. S. Jang, S. Yun Cho, *Scientific Reports* **2016**, *6*, 1.
[133] J. N. Heyman, B. A. Alebachew, Z. S. Kaminski, M. D. Nguyen, N. E. Coates, J. J. Urban, *Applied Physics Letters* **2014**, *104*, 141912.
[134] H. Song, K. Cai, *Energy* **2017**, *125*, 519.
[135] M. Culebras, A. M. Igual-Muñoz, C. Rodríguez-Fernández, M. I. Gómez-Gómez, C. Gómez, A. Cantarero, *ACS Applied Materials and Interfaces* **2017**, *9*, 20826.
[136] Y. He, G. Galli, *Physical Review Letters* **2012**, *108*, 215901.
[137] A. Henry, *Annu. Rev. Heat Transfer* **2013**, *17*, 485.
[138] L. Shi, D. Li, C. Yu, W. Jang, D. Kim, Z. Yao, P. Kim, A. Majumdar, *Journal of Heat Transfer* **2003**, *125*, 881.

[139] L. Yang, Y. Yang, Q. Zhang, Y. Zhang, Y. Jiang, Z. Guan, M. Gerboth, J. Yang, Y. Chen, D. Greg Walker, T. T. Xu, D. Li, *Nanoscale* **2016**, *8*, 17895.
[140] A. Mavrokefalos, M. T. Pettes, F. Zhou, L. Shi, *Review of Scientific Instruments* **2007**, *78*, 034901.
[141] L. Yang, Y. Tao, J. Liu, C. Liu, Q. Zhang, M. Akter, Y. Zhao, T. T. Xu, Y. Xu, Z. Mao, Y. Chen, D. Li, *Nano Letters* **2019**, *19*, 415.
[142] L. Yang, Q. Zhang, Z. Cui, M. Gerboth, Y. Zhao, T. T. Xu, D. G. Walker, D. Li, *Nano Letters* **2017**, *17*, 7218.
[143] Z. Luo, J. Tian, M. Srinivasan, Y. P. Chen, X. Xu, *ACS Nano* **2018**, *12*, 1120.
[144] L. A. Agapito, N. Kioussis, W. A. Goddard, N. P. Ong, *Physical Review Letters* **2013**, *110*, 176401.
[145] E. W. Zaia, A. Sahu, P. Zhou, M. P. Gordon, J. D. Forster, S. Aloni, Y. S. Liu, J. Guo, J. J. Urban, *Nano Letters* **2016**, *16*, 3352.
[146] S. Dongmin Kang, G. Jeffrey Snyder, *Nature Materials* **2017**, *16*, 252.
[147] V. I. Fistul', *Heavily Doped Semiconductors*, Springer New York, **1995**.
[148] C. Liu, J. Xu, B. Lu, R. Yue, F. Kong, *Journal of Electronic Materials* **2012**, *41*, 639.
[149] S. N. Patel, A. M. Glaudell, K. A. Peterson, E. M. Thomas, K. A. O'Hara, E. Lim, M. L. Chabinyc, *Science Advances* **2017**, *3*, e1700434.
[150] O. Bubnova, Z. U. Khan, A. Malti, S. Braun, M. Fahlman, M. Berggren, X. Crispin, *Nature Materials* **2011**, *10*, 429.
[151] O. Bubnova, M. Berggren, X. Crispin, *Journal of the American Chemical Society* **2012**, *134*, 16456.
[152] T. Park, C. Park, B. Kim, H. Shin, E. Kim, *Energy and Environmental Science* **2013**, *6*, 788.
[153] Y. M. Zuev, J. S. Lee, C. Galloy, H. Park, P. Kim, *Nano Letters* **2010**, *10*, 3037.
[154] J. Moon, J.-H. Kim, Z. C. Y. Chen, J. Xiang, R. Chen, *Nano Letters* **2013**, *13*, 1196.
[155] X. Wang, X. Zhang, L. Sun, D. Lee, S. Lee, M. Wang, J. Zhao, Y. Shao-Horn, M. Dincă, T. Palacios, K. K. Gleason, *Science Advances* **2018**, *4*, eaat5780.
[156] A. Hexemer, P. Müller-Buschbaum, *IUCrJ* **2015**, *2*, 106.
[157] J. K. Hobbs, O. E. Farrance, L. Kailas, *Polymer* **2009**, *50*, 4281.
[158] M. Brinkmann, *Materials Chemistry Frontiers* **2020**, *4*, 1916.
[159] U. Lang, E. Müller, N. Naujoks, J. Dual, *Advanced Functional Materials* **2009**, *19*, 1215.
[160] Q. Wei, M. Mukaida, Y. Naitoh, T. Ishida, *Advanced Materials* **2013**, *25*, 2831.
[161] P. Ghosh, M. U. Kahaly, U. V Waghmare, *Physical Review B - Condensed Matter and Materials Physics* **2007**, *75*, 245437.
[162] F. Zhang, E. Mohammadi, X. Luo, J. Strzalka, J. Mei, Y. Diao, *Langmuir* **2018**, *34*, 1109.
[163] H. Li, S. Yan, *Macromolecules* **2011**, *44*, 417.
[164] W. Shi, T. Zhao, J. Xi, D. Wang, Z. Shuai, *Journal of the American Chemical Society* **2015**, *137*, 12929.
[165] H. Peng, N. Kioussis, D. A. Stewart, *Applied Physics Letters* **2015**, *107*, 251904.
[166] J. Callaway, *Physical Review* **1959**, *113*, 1046.
[167] M. Holland, *Physical Review* **1963**, *132*, 2461.
[168] R. Kroon, D. Alemu Mengistie, D. Kiefer, J. Hynynen, J. D. Ryan, L. Yu, C. Müller, *Chemical Society Reviews* **2016**, *45*, 6147.
[169] O. Bubnova, X. Crispin, *Energy Environ. Sci.* **2012**, *5*, 9345.

[170] J. F. Ponder, A. K. Menon, R. R. Dasari, S. L. Pittelli, K. J. Thorley, S. K. Yee, S. R. Marder, J. R. Reynolds, *Advanced Energy Materials* **2019**, *9*, 1900395.
[171] A. K. Menon, O. Meek, A. J. Eng, S. K. Yee, *Journal of Applied Polymer Science* **2017**, *134*, DOI 10.1002/app.44060.
[172] J. Hollinger, D. Gao, D. S. Seferos, *Israel Journal of Chemistry* **2014**, *54*, 440.
[173] E. I. Carrera, D. S. Seferos, *Macromolecules* **2015**, *48*, 297.
[174] A. A. Jahnke, B. Djukic, T. M. McCormick, E. Buchaca Domingo, C. Hellmann, Y. Lee, D. S. Seferos, *Journal of the American Chemical Society* **2013**, *135*, 951.
[175] L. Li, J. Hollinger, A. A. Jahnke, S. Petrov, D. S. Seferos, *Chemical Science* **2011**, *2*, 2306.
[176] J. G. Manion, S. Ye, A. H. Proppe, A. W. Laramée, G. R. McKeown, E. L. Kynaston, S. O. Kelley, E. H. Sargent, D. S. Seferos, *ACS Appl. Energy Mater.* **2018**, *1*, 5033.
[177] E. M. Thomas, E. C. Davidson, R. Katsumata, R. A. Segalman, M. L. Chabinyc, *ACS Macro Lett.* **2018**, *7*, 1492.
[178] P. Y. Yee, D. T. Scholes, B. J. Schwartz, S. H. Tolbert, *J. Phys. Chem. Lett.* **2019**, *10*, 4929.
[179] Z. Liang, Y. Zhang, M. Souri, X. Luo, A. M. Boehm, R. Li, Y. Zhang, T. Wang, D.-Y. Kim, J. Mei, S. R. Marder, K. R. Graham, *Journal of Materials Chemistry A* **2018**, *6*, 16495.
[180] S. L. Pittelli, S. A. Gregory, J. F. Ponder, S. K. Yee, J. R. Reynolds, *J. Mater. Chem. C* **2020**, *8*, 7463.
[181] V. Untilova, T. Biskup, L. Biniek, V. Vijayakumar, M. Brinkmann, *Macromolecules* **2020**, *53*, 2441.
[182] K. E. Watts, B. Neelamraju, E. L. Ratcliff, J. E. Pemberton, *Chem. Mater.* **2019**, *31*, 6986.
[183] H. Méndez, G. Heimel, S. Winkler, J. Frisch, A. Opitz, K. Sauer, B. Wegner, M. Oehzelt, C. Röthel, S. Duhm, D. Többens, N. Koch, I. Salzmann, *Nat Commun* **2015**, *6*, 8560.
[184] O. Zapata-Arteaga, A. Perevedentsev, S. Marina, J. Martin, J. S. Reparaz, M. Campoy-Quiles, *ACS Energy Lett.* **2020**, *5*, 2972.
[185] D. Kiefer, R. Kroon, A. I. Hofmann, H. Sun, X. Liu, A. Giovannitti, D. Stegerer, A. Cano, J. Hynynen, L. Yu, Y. Zhang, D. Nai, T. F. Harrelson, M. Sommer, A. J. Moulé, M. Kemerink, S. R. Marder, I. McCulloch, M. Fahlman, S. Fabiano, C. Müller, *Nature Mater* **2019**, *18*, 149.
[186] D. T. Scholes, P. Y. Yee, J. R. Lindemuth, H. Kang, J. Onorato, R. Ghosh, C. K. Luscombe, F. C. Spano, S. H. Tolbert, B. J. Schwartz, *Advanced Functional Materials* **2017**, *27*, 1702654.
[187] J. Hynynen, D. Kiefer, L. Yu, R. Kroon, R. Munir, A. Amassian, M. Kemerink, C. Müller, *Macromolecules* **2017**, *50*, 8140.
[188] I. E. Jacobs, E. W. Aasen, J. L. Oliveira, T. N. Fonseca, J. D. Roehling, J. Li, G. Zhang, M. P. Augustine, M. Mascal, A. J. Moulé, *J. Mater. Chem. C* **2016**, *4*, 3454.
[189] E. Lim, K. A. Peterson, G. M. Su, M. L. Chabinyc, *Chem. Mater.* **2018**, *30*, 998.
[190] B. Neelamraju, K. E. Watts, J. E. Pemberton, E. L. Ratcliff, *J. Phys. Chem. Lett.* **2018**, *9*, 6871.
[191] J. K. Harris, B. Neelamraju, E. L. Ratcliff, *Chem. Mater.* **2019**, *31*, 6870.
[192] K. E. Watts, B. Neelamraju, M. Moser, I. McCulloch, E. L. Ratcliff, J. E. Pemberton, *J. Phys. Chem. Lett.* **2020**, *11*, 6586.

[193] H. Wang, S. V. Levchenko, T. Schultz, N. Koch, M. Scheffler, M. Rossi, *Advanced Electronic Materials* **2019**, *5*, 1800891.

[194] M. T. Fontana, D. A. Stanfield, D. T. Scholes, K. J. Winchell, S. H. Tolbert, B. J. Schwartz, *J. Phys. Chem. C* **2019**, *123*, 22711.

[195] D. A. Stanfield, Y. Wu, S. H. Tolbert, B. J. Schwartz, *Chem. Mater.* **2021**, *33*, 2343.

[196] S. Ye, L. Janasz, W. Zajaczkowski, J. G. Manion, A. Mondal, T. Marszalek, D. Andrienko, K. Müllen, W. Pisula, D. S. Seferos, *Macromolecular Rapid Communications* **2019**, *40*, 1800596.

[197] S. A. Gregory, Y. Li, T. D. Monroe, J. Li, S. K. Yee, M. D. Losego, *ACS Appl. Polym. Mater.* **2021**, *3*, 720.

[198] J. Hynynen, E. Järsvall, R. Kroon, Y. Zhang, S. Barlow, S. R. Marder, M. Kemerink, A. Lund, C. Müller, *ACS Macro Lett* **2019**, *8*, 70.

[199] V. Vijayakumar, E. Zaborova, L. Biniek, H. Zeng, L. Herrmann, A. Carvalho, O. Boyron, N. Leclerc, M. Brinkmann, *ACS Applied Materials & Interfaces* **2019**, *11*, 4942.

[200] A. Hexemer, W. Bras, J. Glossinger, E. Schaible, E. Gann, R. Kirian, A. MacDowell, M. Church, B. Rude, H. Padmore, *J. Phys. Conf. Ser.* **2010**, *247*.

[201] J. Ilavsky, *J Appl Cryst* **2012**, *45*, 324.

[202] E. M. Thomas, K. A. Peterson, A. H. Balzer, D. Rawlings, N. Stingelin, R. A. Segalman, M. L. Chabinyc, *Advanced Electronic Materials* **2020**, *6*, 2000595.

[203] R. C. Shallcross, T. Stubhan, E. L. Ratcliff, A. Kahn, C. J. Brabec, N. R. Armstrong, *J. Phys. Chem. Lett.* **2015**, *6*, 1303.

[204] E. L. Kynaston, K. J. Winchell, P. Y. Yee, J. G. Manion, A. D. Hendsbee, Y. Li, S. Huettner, S. H. Tolbert, D. S. Seferos, *ACS Applied Materials & Interfaces* **2019**, *11*, 7174.

[205] D. T. Duong, C. Wang, E. Antono, M. F. Toney, A. Salleo, *Organic Electronics* **2013**, *14*, 1330.

[206] J. Rivnay, R. Noriega, R. J. Kline, A. Salleo, M. F. Toney, *Phys. Rev. B* **2011**, *84*, 045203.

[207] J. Rivnay, S. C. B. Mannsfeld, C. E. Miller, A. Salleo, M. F. Toney, *Chem. Rev.* **2012**, *112*, 5488.

[208] S. N. Patel, A. M. Glaudell, D. Kiefer, M. L. Chabinyc, *ACS Macro Letters* **2016**, *5*, 268.

[209] G. Freychet, E. Gann, L. Thomsen, X. Jiao, C. R. McNeill, *J. Am. Chem. Soc.* **2021**, *143*, 1409.